Commissioning of the Recoil Silicon Detector for the HERMES Experiment

Der Naturwissenschaftlichen Fakultät
der Friedrich-Alexander-Universität Erlangen Nürnberg
zur
Erlangung des Doktorgrades

vorgelegt von
Nils Christian Pickert
aus Erlangen

Als Dissertation genehmigt von den Naturwissenschaftlichen Fakultäten der Universität Erlangen-Nürnberg

Tag der mündlichen Prüfung: 24. Januar 2008

Vorsitzender der Promotionskommission:		Prof. Dr. E. Bänsch
Erstberichterstatter	:	Prof. Dr. K. Rith
Zweitberichterstatter	:	Prof. Dr. W. Eyrich

Zusammenfassung

Generalisierte Parton Verteilungen (GPD) bieten eine einzigartige Möglichkeit, Informationen über die innere Struktur der Nukleonen zu erhalten. Messungen des Hermes Experimentes sowie anderer Experimente lieferten bisher die seperate Beschreibung der longitudinalen Impulsverteilung der Konstituenten des Nukleons (über die Parton-Verteilungs-Funktionen) und der transversen räumlichen Ladungsverteilung (über Formfaktoren). Generalisierte Parton Verteilungen vereinigen nun diese beiden Aspekte in einer einzigen Beschreibung und beinhalten weitere, bisher nicht zugängliche Informationen über die Quark-Gluon-Struktur der Nukleonen. Das bekannteste Beispiel solcher zusätzlicher Informationen ist die Summenregel von Ji, ein Integral über die Summe zweier GPDs, die die Bestimmung des Gesamtdrehimpulses der Quarks erlaubt.

Der zugänglichste Weg, um GPDs experimentell zu bestimmen, ist das Studium der tief-virtuellen Compton Streuung (DVCS), der harten exklusiven Produktion eines reelen Photons in Lepton-Hadron Streuung. Insbesondere erlaubt die Interferenz dieses Prozesses mit dem Bethe-Heitler Prozess die Messung von Asymmetrien in Bezug auf die Spin-Ausrichtung und die Ladung des Leptons sowie auf die Spin-Ausrichtung des Target-Nukleons. Aus diesen Asymmetrien lassen sich Compton Form-Faktoren berechnen, aus diesen wiederum die Generalisierten Parton Verteilungen. Einige dieser Asymmetrien wurden bereits mit dem Hermes Experiment vermessen, da jedoch das zurück gestreute Nukleon nicht detektiert werden konnte, musste die fehlende Masse (*missing mass*) aus der Spur des Leptons und der Energie des erzeugten Photons rekonstruiert werden. Die Vielseitigkeit des Hermes Gas-Targets ermöglichte es, diese Streuprozesse an spin-polarisiertem Wasserstoff und Deuterium sowie an verschiedenen unpolarisierten schwereren Gasen zu vermessen.

Die Rekonstruktion der fehlenden Masse ist limitiert durch die Orts- und Impulsauflösung des Hermes Spektrometers, daher ist es mit den bisherigen Messungen nur möglich, die führenden Momente der Asymmetrien zu bestimmen. Um höhere Genauigkeit in den Messungen zu erreichen, muss das zurück gestreute Nukleon

ebenfalls detektiert werden. Ein dazu geeigneter Detektor muss die Möglichkeit bieten, den Impuls der Teilchen über einen sehr großen Bereich zu bestimmen: von minimal ionisierenden Teilchen bis zu Protonen, die im Detektor gestoppt werden. Der Detektor muss ebenfalls Hadronen und Mesonen unterscheiden können sowie möglichst den kompletten Raumbereich um das Target umschließen.

Im Winter 2005–2006 wurde ein solcher Rückstoß-Detektor (*Recoil Detector*) im HERMES Experiment installiert und nahm Daten in der Zeit zwischen Mai 2006 und dem Ende des HERA Betriebes Ende Juni 2007. Der Detektor besteht aus drei Teil-Detektoren: einem Silizium-Zähler innerhalb der Streukammer, einem Detektor aus szintillierenden Fasern und einem Photon-Detektor. Er befindet sich im 1 T starken Magnetfeld eines supraleitenden Magneten.

Der Szintillierende-Faser-Detektor besteht aus vier Lagen mit mehr als 7000 Fasern, die in zwei Zylindern angeordnet sind. Ein Zylinder befindet sich direkt außerhalb der Streukammer, der zweite schließt bündig an den Photon-Detektor an. Er liefert sowohl Raum-Punkte für die Spurverfolgung als auch Energie-Messungen. Der Photon-Detektor befindet sich in der Bohrung des Magneten und besteht aus drei Lagen Szintillatoren, eine davon parallel zur Strahl-Achse, die beiden anderen unter $\pm 45^\circ$. Vor jeder Szintillatorlage befindet sich eine Konverterschicht aus Wolfram. Die Hauptaufgabe des Photon-Detektors ist der Nachweis von Photonen aus Zerfällen von π^0-Mesonen, die aus dem Zerfall von Δ-Resonanzen zu einem Meson und einem Proton stammen. Das Proton kann dadurch von Rückstoß-Protonen unterschieden werden, die direkt aus einem DVCS-Prozess stammen.

Der Silizium-Detektor ist innerhalb der Streukammer montiert, er befindet sich im HERA Vakuum. Er besteht aus 16 Sensoren mit einer Fläche von 10×10 cm^2, die in 8 Modulen zu je zwei Sensoren in zwei Lagen um die Target-Zelle angeordnet sind. Jeder Sensor besitzt 128 Streifen auf jeder Seite, die Streifen auf der p-Seite sind rechtwinkelig zu denen auf der n-Seite angeordnet. Um die Energie-Deposition von Teilchen über einen großen Impuls-Bereich messen zu können, wurde eine spezielle Ladungs-Aufteilungs-Auslese entwickelt. Jeder Sensor ist sowohl mit einem HELIX Auslese-Chip direkt verbunden, als auch über einen 10 pF Kondensator mit einem zweiten HELIX Chip, das Signal wird so in einen Pfad mit hoher Verstärkung (*high gain*) und in einen mit niedriger Verstärkung (*low gain*) aufgeteilt. Diese Auslese erlaubt es, die Energie-Depositionen von minimal ionisierenden Teilchen bis zu dem Siebzigfachen dieser Energiedeposition zu messen.

Vor der Installation des Detektors wurden die Silizium-Module in einem Bench-Test und, zusammen mit den anderen Teildetektoren, in einem Test-Experiment

geprüft. Ein Großteil dieser Dissertation widmete sich der Planung und Durchführung dieser Tests sowie deren Auswertung. Es konnte gezeigt werden, dass die Module gemäß ihrer Spezifikation funktionierten, jedoch durch unerwartet hohes Rauschen eine Signal-Korrektur notwendig wurde. Verschiedene Modelle zur Korrektur wurden im Rahmen dieser Arbeit entwickelt und getestet. Nach Fertigstellung des Test-Experimentes konnte jedoch durch eine kleine Modifikation der Module das Rauschen drastisch reduziert werden. Trotz des hohen Rauschens konnten im Test-Experiment kosmische Müonen nachgewiesen und ihre Energie-Deposition mit einem Signal-Rausch-Verhältnis von 2:1 gemessen werden.

In der Winterpause 2005–2006 wurde der *Recoil Detector* in das HERMES Experiment installiert. Erste Diagnose- und Analyse-Software wurde während dieser Arbeit entwickelt. Kurz nach Inbetriebnahme wurde jedoch ein falsch montiertes Zwischenstück in der HERA Strahlröhre entdeckt, dass für extrem hohes Rauschen im Silizium-Detektor sowie für ein Überhitzen der Targetzelle verantwortlich war. Nach Austausch dieses Zwischenstückes und Einbau einer elektromagnetischen Abschirmung um den Silizium-Detektor sank das Rauschen auf ein normales Niveau und die Targetzellen-Temperatur blieb konstant. Ein Strahlstrom-abhängiges Wandern der Null-Linie (*pedestal*) der Silizium-Detektoren wurde weiterhin beobachtet, kann jedoch off-line korrigiert werden.

Das beobachtete *Common Mode* Rauschen (ein korreliertes Rauschen auf allen Streifen) zeigte eine von Streifen zu Streifen variierende Stärke. Um dieses Rauschen zu korrigieren, wurde jeder achte Streifen eines Sensors immer ausgelesen, ein Spline durch diese Datenpunkte gelegt und dieser Spline zur Interpolation des korrelierten Rauschens benutzt. Nach Korrektur betrug das durchschnittliche Rauschen 3 ADC Kanäle, die Null-Breite der zur Interpolation verwendeten Streifen wird durch diese Methode künstlich auf Null gezwungen.

Der Silizium-Detektor maß erfolgreich Energie-Depositionen von Minimal Ionisierenden Teilchen bis zu im Sensor gestoppten Protonen. Minimal Ionisierende Teilchen konnten mit einem Signal-Rausch-Verhältnis von 5:1 nachgewiesen werden. Mit Hilfe von Spurinformationen des Szintillierende-Fasern-Detektors können Protonen von Pionen und anderen Mesonen durch den Silizium-Detektor unterschieden werden. Der HERMES Silizium-Recoil-Detektor wurde erfolgreich installiert und betrieben. Er nahm Daten zwischen Mai 2006 und dem Ende des HERA Betriebes am 30. Juni 2007. Die speziell entwickelte Ladungs-Aufteilung ermöglichte die Bestimmung der Energiedeposition über einen sehr großen Impulsbereich. Trotz der harschen Bedingungen innerhalb der Streukammer war ein erfolgreicher Betrieb

des Silizium-Detektors möglich.

Während der Datennahme mit einem Wasserstoff-Target wurden 28 Millionen DIS Ereignisse beobachtet, weitere 7 Millionen DIS Ereignisse wurden an einem Deuterium Target beobachtet. Dies ist etwa das vierfache der bis 2005 gesehenen Daten vor der Installation des Recoil Detektors. Erste Daten-Analysen ohne die Informationen des Recoil Detektors zeigen alleine durch die höhere Statistik bereits deutlich geringere Fehler, eine deutliche Verbesserung der Ergebnisse wird durch die Verwendung der Daten des Recoil-Detektors erwartet. Der HERMES Recoil Detektor ist ein hervorragendes Werkzeug zur Unterdrückung des Untergrundes bei der Messung tief-virtueller Compton Streu-Prozesse.

Contents

Nomenclature

A short overview of the nomenclature in this thesis.

Physics

Symbol	Meaning
$\mathbf{p}, \mathbf{k}, \ldots$	Bold face denotes four-vectors
F_1^q,F_2^q	Elastic Pauli and Dirac Form factors for quark flavour q
G_A^q,G_P^q	Axial- and Pseudocalar Form factors for quark flavour q
H,$\widetilde{H}$,E,$\widetilde{E}$	Generalised Parton Distributions
$\mathcal{H}$,$\widetilde{\mathcal{H}}$,$\mathcal{E}$,$\widetilde{\mathcal{E}}$	Compton Form Factors
A_{xy}	Azimuthal Asymmetry for beam state x and target state y

Signal Model

Symbol	Meaning
$E^k_{\text{dep},i}$	Energy deposited in strip k for event i
Q_i^k	Charge in strip k for event i including all noise sources
S_i^k	Charge produced by the passing particle in strip k for event i
P^k	Pedestal of strip k
C_i	Common Mode Noise for event i
N_i^k	Noise for strip k and event i
$w_k(C^i)$	Common Mode dependant weighting factor
$\mathfrak{S}_i^k \ldots$	Signal digitised by HADC for event i and strip k
$U^k_{\text{ACC},i}$	output voltage of the silicon module for strip k and event i on it's signal lines
g_{ACC}	Gain of the ACC module
c_{HADC}	Conversion factor of an HADC
$g^k_{\text{Si},x}$	Calibration factor of strip k for gain x (Hi or Lo) specific for each module
h^k	Ratio of Low gain to high gain

1 Introduction

> “Se ao menos isto tudo se passasse
> numa Terra de mulheres bonitas!”
> *José Almada Negreiros – Cena do ódio*

Starting with Rutherford's discovery of the atomic nucleus at the beginning of the 20th century, scattering experiments unravelled the internal structure of the atom and its components. Using the large angle scattering of α-particles off atoms, Rutherford concluded that the atom bears a central core, the nucleus. Subsequent experiments led to the discovery of the neutron and the proton as the building blocks of this nucleus, commonly referred to as nucleons. Stern [ESS37] and Hofstadter [MH56] showed experimentally that also the nucleons had to consist of smaller particles. Stern showed that the magnetic moment of protons was not consistent with a single particle interpretation. Hofstadter determined in scattering experiments the electromagnetic Form Factors of the proton. These Form Factors describe the spatial distribution of charge and the magnetic moment inside the proton and show that the nucleon is a composite object. Experiments using deep-inelastic lepton-nucleon scattering at the Stanford linear collider detected events where a large momentum transfer from the electron to the proton was observed. The only possible explanation was that the nucleon contained point-like partons [BFK+69].

The theoretical description of deep-inelastic scattering processes led to Bjorken's scaling hypothesis, stating that the structure functions describing deep-inelastic processes must not depend on parameters containing physical dimensions [Bjo69]. A theoretical image of the nucleon at high energy was provided by Feynman's parton model [Fey69]: at high energy the nucleon can be viewed as a composite object of small independent constituents, where the interactions of a probe only happens with one of these constituents. The charged constituents should be of spin one-half and were identified with Murray Gell-Mann's [GM64] quarks and Zweig's [Zwe64] aces[1].

[1] The name *quarks* stuck, Zweig's term *ace* disappeared soon.

The charge-less constituents were to be called gluons. Subsequently a field theory of strong interactions was developed to describe the quarks, the gluons and their interactions—Quantum Chromo-Dynamics (QCD).

Together with the theory of electroweak interaction, QCD forms the foundation of the *standard model* of particle physics. According to the standard model, the constituents of matter are quarks and leptons, interacting with electromagnetic, weak and strong forces transmitted by photons, W- and Z-bosons and gluons.[2] Above an energy of 10^2 GeV electromagnetic and weak force can be described by the same formalism, at a scale $\sim 10^{14}$ GeV this can also be done for the electroweak and the strong force. The standard model has been tested extensively in experiments at particle colliders like LEP at CERN, SLC at SLAC, the Tevatron at Fermi-National-Lab and HERA at DESY. It has become the most predictive and best tested theory in science.

However, some problems still remain. QCD describes aptly well strong interaction dynamics on a short scale, but the long distance behaviour is still not calculable analytically. Free quarks have not been observed; instead, when emitted, they form a colour neutral object and fragment into observable hadrons. In the case of a large (hard) momentum transfer in a scattering process, the emitted quarks do not show up as single quarks but form jets of hadrons. This process cannot be described analytically so far, although a rough physical picture exists: The quarks are imagined to be connected by a string of glue. Separating the quarks increases the energy stored in the string up to the point where the string breaks down and forms a quark-antiquark pair from the vacuum at it's ends. This *infrared slavery* is yet prohibiting an analytical description of the nucleon's interior.

Hard scattering processes, like Deep-Inelastic Scattering (DIS), can be described by a hard scattering amplitude calculable in perturbative QCD and a non-perturbative soft part, thus separating the calculable part from a parametrisation which needs to be determined empirically [Rad96, CF99]. In case of inclusive and semi-inclusive DIS on a nucleon, the nucleon's internal structure involved in the scattering process is described by Parton Distribution Functions (PDFs). These PDFs are the longitudinal momentum distributions of the nucleon's constituents. The transverse spatial location of the partons is accessible by elastic processes, it is described by Form Factors (FFs). The FFs yield no direct information on the momentum distribution, the PDFs contain no information on the spatial location. However, both aspects are needed for a complete description of the nucleon.

Recently the formalism of Generalised Parton Distributions (GPDs) has been introduced [Rad97, JMS97, e.g.]. In these GPDs a wealth of information on the quark-gluon structure of the nucleon is encoded. They are generalised in the sense that the Parton Distribution Functions and the Form Factors appear as limiting cases and x-moments, respectively. GPDs contain information on the 2+1 dimensional distribution of partons inside the nucleon [Bur07]: the transverse spatial distribution (two dimensions) and the longitudinal distribution of momenta (one dimension). The angular momentum of the quarks is also accessible via Ji's sum rule, an integral over the sum of two GPDs [Ji97b]. Generalised Parton Distributions can describe hard exclusive processes like Deeply Virtual Compton Scattering (DVCS) or hard meson production. GPDs have been extended to nuclear targets with spins different to 1/2 in order to learn more about nuclear structure.

Observables from Deeply Virtual Compton Scattering (DVCS) and it's interference with the competing Bethe-Heitler process (BH) provide the simplest experimental access to the GPD framework. The cross section of the interference between DVCS and BH shows various single spin asymmetries, like the Beam Charge Asymmetry (BCA) for different beam charges or the Transverse Target Spin Asymmetry (TTSA) for different transverse target spin states, which provide access to a combination of the GPDs necessary to describe the nucleon's structure. In order to improve the accuracy of the measurements of some of these asymmetries, a recoil detector has been installed at the HERMES experiment located at the HERA accelerator. This thesis covers the testing, the installation and the commissioning of the silicon sub-detector of this recoil detector. A short introduction on the physical processes to be measured will be given (chapter 2), followed by a description of the HERMES-experiment (chapter 3) and it's recent results on DVCS (chapter 4). A portraiture of the recoil detector is given (chapter 5), followed by an overview of silicon detectors and detector noise considerations (chapter 6). Chapter 7 deals with the simulation of the silicon detector in the HERMES-Monte-Carlo simulation, chapter 8 gives an overview on the performance tests done before installation. In chapter 9 first data measured by the recoil silicon detector are presented.

[2] Gravity is not included in the standard model.

2 Towards a new picture of the Nucleon

> "In order to get any picture at all of a thing, it is sometimes necessary to begin with a false picture and then correct it."
> *C.S. Lewis – Miracles*

In the year 1923 Arthur Holly Compton researched the scattering of photons off electrons in the atoms electron cloud, proving the particle like nature of the photon [Com23a, Com23b]. A similar process can be used in particle physics to disentangle the inner structure of the nucleon: Deeply Virtual Compton Scattering (DVCS). A virtual photon generated by inelastic lepton scattering, interacts with a quark of momentum $(x + \xi)\mathbf{P}$, where $\mathbf{P}$ is the momentum of the proton. A real photon is then emitted by this quark, and the quark returns into the nucleon with a momentum of $(x - \xi)\mathbf{P}$. The Feynman graph of this process is shown in Figure 2.1(a). It was first shown by Ji that this process allows to access GPDs [Ji97b].

The following section will give an overview of the kinematical variables used. Then a short introduction to the GPD framework will be given and it will be shown how GPDs can be determined experimentally.

2.1 Kinematics

The exclusive lepto-production of a photon off a nucleon with mass M

$$e(\mathbf{k}) + N(\mathbf{P}) \to e(\mathbf{k}') + N(\mathbf{P}') + \gamma(\mathbf{v}) \tag{2.1}$$

is usually described in terms of the four-momenta $\mathbf{k}$ ($\mathbf{k}'$) and $\mathbf{P}$ ($\mathbf{P}'$) of the incoming (outgoing) lepton and nucleon. The following Lorentz-invariant quantities are

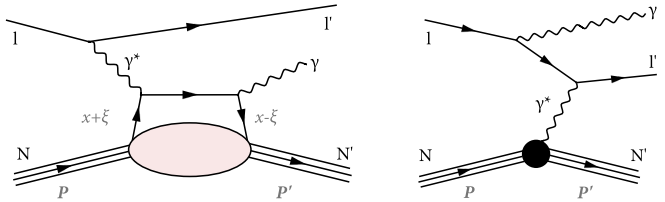

(a) The Deeply Virtual Compton Scattering process.

(b) One possible Bethe-Heitler process.

Figure 2.1: The two processes for the electro-production of a photon off a nucleon.

defined:

$$s \equiv (\mathbf{k} + \mathbf{P})^2, \tag{2.2}$$

$$q^2 = -Q^2 \equiv (\mathbf{k} - \mathbf{k}')^2 < 0, \tag{2.3}$$

$$W^2 \equiv (\mathbf{P} + \mathbf{q})^2, \tag{2.4}$$

$$\nu \equiv \frac{\mathbf{P} \cdot \mathbf{q}}{M}; \tag{2.5}$$

where s is the centre of mass energy squared, q the four-momentum transfer by the virtual photon and W^2 the squared energy in the photon-nucleon centre of mass system. The quantity ν has no easy physical interpretation in this frame. In the reference frame of a fixed target experiment and under the assumption of a negligible electron mass, these quantities can be expressed as

$$s = 2ME + M^2, \tag{2.6}$$

$$Q^2 = 4EE' \sin^2 \frac{\theta_e}{2}, \tag{2.7}$$

$$W^2 = M^2 + 2M\nu - Q^2, \tag{2.8}$$

$$\nu = E - E'; \tag{2.9}$$

where E and E' denote the energies of the incoming and the scattered lepton respectively; θ_e is the angle between the initial and final lepton trajectory. In this rest-frame,

ν is the energy of the virtual photon. Additionally two dimensionless variables are introduced:

$$x_B \equiv \frac{Q^2}{2\mathbf{P} \cdot \mathbf{q}} = \frac{Q^2}{2M\nu} \tag{2.10}$$

which, in the case of DIS can be interpreted as the fraction of the four-momentum of the nucleon that is carried by the struck quark; and

$$y \equiv \frac{\mathbf{P} \cdot \mathbf{q}}{\mathbf{P} \cdot \mathbf{k}} = \frac{\nu}{E} \tag{2.11}$$

which is the fractional energy of the virtual photon with respect to the beam energy. For both variables the allowed region is $0 < x_B, y \leq 1$. All the variables Q^2, W^2, ν, x_B and y are fully defined by the properties of the initial particles and the outgoing lepton only.

In the case of exclusive meson production or DVCS additional variables are needed to describe the final state of three particles. The four momentum transfer to the nucleon Δ and its square, the Mandelstam invariant t are given by

$$\Delta \equiv \mathbf{P}' - \mathbf{P}, \tag{2.12}$$

$$t \equiv \Delta^2 < 0. \tag{2.13}$$

A generalised Bjorken-variable ξ, the *skewness*, is introduced as

$$\xi \equiv \frac{-q^2}{\mathbf{q} \cdot \mathbf{P}} \approx \frac{x_B}{2 - x_B}. \tag{2.14}$$

This variable can be interpreted as follows for the process shown in Figure 2.1(a): a quark with the momentum fraction $x + \xi$ is taken out of the nucleon, interacts with the virtual photon, emits a real photon and then returns back into the nucleon with a momentum fraction of $x - \xi$. The quantity x can be interpreted as the longitudinal momentum fraction of the struck quark. It is an internal loop variable and therefore experimentally inaccessible.

2.2 Generalised Parton Distributions

Figure 2.1(a) represents the so called *handbag-diagram*. In contrast to the usual Deep-Inelastic Scattering Feynman graph, the quark taken out of the nucleon and

the quark going back into it have a different momentum fraction x. To describe this process a transition matrix with off-diagonal elements is needed. Therefore a new type of parton distributions, which parametrise the transition matrix elements were introduced: the off-forward PDFs [Ji97b, Ji97a] or non-forward PDFs [Rad97, Rad98]. Recently a common nomenclature for both has been developed and the term Generalised Parton Distribution (GPD) is commonly used for the distribution functions.

At leading twist the structure of the nucleon is described by eight GPDs for each quark flavour q and eight GPDs for the gluons. Four of the parton GPDs conserve the parton's helicity, four involve an helicity-flip. The parton helicity conserving ones are the unpolarised GPDs $H(x,\xi,t)$ and $E(x,\xi,t)$ and the polarised GPDs $\widetilde{H}(x,\xi,t)$ and $\widetilde{E}(x,\xi,t)$. Of these $H(x,\xi,t)$ and $\widetilde{H}(x,\xi,t)$ conserve the nucleon's helicity, while the other two do not. The four parton helicity-flip GPDs are denoted by $H_T(x,\xi,t)$, $E_T(x,\xi,t)$, $\widetilde{H}_T(x,\xi,t)$ and $\widetilde{E}_T(x,\xi,t)$.

In the forward limit $t \to 0$ (where also $\xi \to 0$) the GPDs H and $\widetilde{H}$ reduce to the quark density distributions $q(x)$ and quark helicity distributions $\Delta q(x)$, obtainable also from DIS:

$$H^q(x,0,0) = \begin{cases} q(x) & x > 0 \\ -\overline{q}(-x) & x < 0, \end{cases} \tag{2.15}$$

$$\widetilde{H}^q(x,0,0) = \begin{cases} \Delta q(x) & x > 0 \\ -\Delta\overline{q}(-x) & x < 0. \end{cases} \tag{2.16}$$

The GPDs E and $\widetilde{E}$ are inaccessible in the forward limit. In the region $-\xi < x < \xi$ one parton involved in the scattering process in figure 2.2 represents a quark, the other one an antiquark. In this region the GPDs can be interpreted as a meson distribution amplitude [Rad96, GPV01]. They therefore contain new information on the nucleon, not accessible through DIS (which corresponds to the limit $\xi \to 0$).

The first moments of the GPDs are related to the elastic form factors of the nucleon

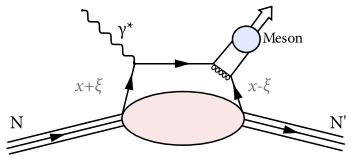

Figure 2.2: Meson production through DVCS.

through sum rules [Ji97b]

$$\int_{-1}^{1} H^q(x,\xi,t)\,dx = F_1^q(t), \tag{2.17}$$

$$\int_{-1}^{1} E^q(x,\xi,t)\,dx = F_2^q(t), \tag{2.18}$$

$$\int_{-1}^{1} \widetilde{H}^q(x,\xi,t)\,dx = G_A^q(t), \tag{2.19}$$

$$\int_{-1}^{1} \widetilde{E}^q(x,\xi,t)\,dx = G_P^q(t), \tag{2.20}$$

where F_1^q and F_2^q are the elastic Dirac and Pauli form factors , $G_A^q(t)$ and $G_P^q(t)$ represent the axial-vector and pseudo-scalar form factors of the nucleon for a quark flavour q. The form factors for the hadron are given by the sum $F_{1,2} = \sum_q e_q F_{1,2}^q$.

In the limit of vanishing four-momentum transfer t the second moment of the sum of the GPDs $H^q(x,\xi,t)$ and $E^q(x,\xi,t)$ is connected to the total angular momentum J_q of the quark flavour q by Ji's sum rule [Ji97b]:

$$J_q = \lim_{t\to 0} \frac{1}{2} \int_{-1}^{1} \left(H^q(x,\xi,t) + E^q(x,\xi,t) \right) x\,dx. \tag{2.21}$$

Together with the observation on the quark spin contributions to the spin of the nucleon it is possible to extract information on the orbital angular momentum of the quarks.

Apart from these limits and sum rules various interpretations of GPDs have been suggested. As an example, the transverse distribution of quarks can be extracted, so that a 2+1-dimensional picture of the nucleon can be derived [Bur07] (two spatial

dimensions for the transverse distribution plus an additional dimension for the longitudinal momentum distribution). It is also possible to access the symmetric energy-momentum tensor through GPDs and therefore determine the gravitational form factors of the nucleon [BR05]. An overview on GPDs and their possible interpretations can be found in reference [BR05].

2.3 Cross Sections

The initial and final states described in equation 2.1 on page 5 are not singular to DVCS, they are also describing the Bethe-Heitler process shown in Figure 2.1(b) on page 6, where the real photon is emitted by the lepton or the nucleon as initial state or final state radiation. These two processes are experimentally indistinguishable. The kinematical variables given above are also calculable for the BH process, although their physical interpretation is not valid in this case. As both processes, BH and DVCS, have the same final state their scattering amplitudes add coherently. The squared photon production amplitude then is given as

$$|\tau|^2 = |\tau_{\mathrm{BH}} + \tau_{\mathrm{DVCS}}|^2 = |\tau_{\mathrm{BH}}|^2 + |\tau_{\mathrm{DVCS}}|^2 + \underbrace{\tau_{\mathrm{DVCS}}\tau^*_{\mathrm{BH}} + \tau^*_{\mathrm{DVCS}}\tau_{\mathrm{BH}}}_{I}, \tag{2.22}$$

where I denotes the interference term between BH and DVCS. For an unpolarised proton target the cross section for the hard electro-production of photons can be given by [BMK02]

$$\frac{d\sigma}{dx_{\mathrm{B}}\,dy\,d|t|\,d\phi} = \frac{\alpha^3_{\mathrm{em}} x_{\mathrm{B}} y}{8\pi Q^2\sqrt{1+4x_{\mathrm{B}}^2M^2/Q^2}}\left|\frac{\tau}{e^3}\right|^2, \tag{2.23}$$

with the electromagnetic fine structure constant α_{em} and the lepton charge e. The azimuthal angle ϕ around the virtual photon direction is given by the lepton scattering plane defined by the ingoing and the scattered lepton and the photon production plane defined by the trajectories of the virtual and the real photon (see Figure 2.3).

As the cross section of the Bethe-Heitler process is calculable exactly in Quantum Electro-Dynamics (QED), it is possible to obtain the DVCS cross section to leading twist by measurement of the photo-production cross section and subtracting the BH cross section, if the latter is small. Since at Hermes kinematics the DVCS cross section is at least an order of magnitude smaller than the BH cross section [KN02], this method would lead to large uncertainties.

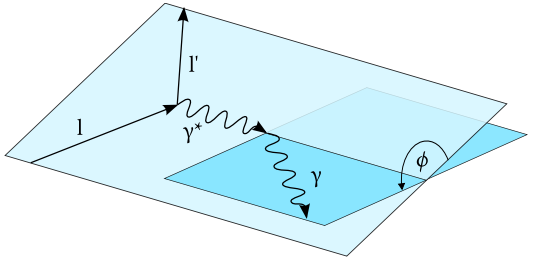

Figure 2.3: Definition of the angle ϕ. Here l denotes the incoming, l' the outgouing leption, γ^* is the exchanged virtual photon and γ the scattered real photon.

2.4 Azimuthal Asymmetries

Although it is not feasible to measure the DVCS cross section directly at Hermes, it is possible to access DVCS amplitudes using the interference with BH. The three summands of equation 2.22 can be expanded in Fourier series in ϕ:

$$|\tau_{\mathrm{BH}}|^2 = \frac{e^6}{x_{\mathrm{B}}^1 y^2(1+4x_{\mathrm{B}}^2M^2/Q^2)^2P_1(\phi)P_2(\phi)}\left(c_{\mathrm{o}}^{\mathrm{BH}} + \sum_{n=1}^{2} c_n^{\mathrm{BH}}\cos(n\phi)\right), \tag{2.24}$$

$$|\tau_{\mathrm{DVCS}}|^2 = \frac{e^6}{y^2Q^2}\left(c_{\mathrm{o}}^{\mathrm{DVCS}} + \sum_{n=1}^{2} c_n^{\mathrm{DVCS}}\cos(n\phi) + s_1^{\mathrm{DVCS}}\sin(\phi)\right), \tag{2.25}$$

$$I = \frac{\pm e^6}{x_{\mathrm{B}}y^3tP_1(\phi)P_2(\phi)}\left(c_{\mathrm{o}}^{I} + \sum_{n=1}^{3} c_n^{\mathrm{I}}\cos(n\phi) + \sum_{n=1}^{2} s_n^{\mathrm{I}}\sin(n\phi)\right), \tag{2.26}$$

where the + (−) sign of the interference term corresponds to a negatively (positively) charged lepton beam. The Fourier coefficients c_n and s_n depend on the kinematic variables x_{B}, y, Q^2 and t. $P_1(\phi)$ and $P_2(\phi)$ are the BH propagators, which introduce an additional dependence on ϕ. They can be approximated by $P_i = A_i + B_i\cos(\phi)$, whereby B_i is suppressed by at least an order of $1/Q$. The complete expressions for these propagators as well as for the Fourier coefficients can be found in [BMK02]. The BH term does not depend on GPDs, in case of an unpolarised proton target the cross-section is an even function in ϕ and hence only cosine-terms are non-zero.

No single-spin-asymmetries exists and only double-spin asymmetries are possible as in the case of elastic scattering. It is also possible to calculate the cross section exactly in QED.

The contribution of the pure DVCS cross-section is assumed to be rather small compared to the BH part at HERMES kinematics. The second largest contribution therefore arises from the interference term. This term can be described by interference amplitudes to express the observed cross-section moments in terms of the Compton form-factors $\mathcal{H}$, $\mathcal{E}$, $\widetilde{\mathcal{H}}$ and $\widetilde{\mathcal{E}}$. For an unpolarised hydrogen target (U) the interference amplitude C_U^I can be written at leading twist as:

$$C_U^I = F_1\mathcal{H}(\xi,t) + \xi(F_1+F_2)\widetilde{\mathcal{H}}(\xi,t) - \frac{t}{4M^2}F_2\mathcal{E}(\xi,t). \tag{2.27}$$

At HERMES kinematics the dependencies on $\widetilde{\mathcal{H}}$ and $\mathcal{E}$ are kinematically suppressed, the main dependency is on $\mathcal{H}$.

With this definition the Fourier coefficients at leading twist can be written as

$$c_{1,U}^I = 8K(2-2y+y^2)\mathfrak{Re}\,C_U^I \tag{2.28}$$

$$s_{1,U}^I = 8K\lambda y(2-y)\mathfrak{Im}\,C_U^I \tag{2.29}$$

where λ denotes the beam polarisation and K is a kinematical factor as defined in [BMK02]. This reference also lists the Fourier coefficients for longitudinally and transversely polarised targets.

Using appropriate azimuthal asymmetries it is possible to extract these Fourier coefficients, relevant for an unpolarised target are the beam-spin and the beam-charge asymmetry. Using a polarised target allows to access other combinations of the Compton form factors, some of the asymmetries which were measured at HERMES using a polarised target are presented in chapter 3.

Beam-Spin Asymmetry The beam spin asymmetry

$$A_{LU}(\phi) \equiv \frac{d\overrightarrow{\sigma} - d\overleftarrow{\sigma}}{d\overrightarrow{\sigma} + d\overleftarrow{\sigma}}, \tag{2.30}$$

where the indices denote a longitudinally (L) polarised beam and an unpolarised (U) target, is a cross section asymmetry built from two measurements with opposite beam helicity, denoted in the equation by arrows with opposite orientation. Assuming

the magnitude of the polarisation being the same in both helicity states, only the polarisation dependent Fourier coefficients (s_1^I, s_2^I, s_1^{DVCS}) are left in the numerator and only those independent of λ are left in the denominator (all others). Of those left in the numerator, only s_1^I is related to twist-two quark GPDs, while s_2^I and s_1^{DVCS} are suppressed at a twist-three level. The denominator is dominated by the $|\tau_{BH}|^2$ contribution at HERMES kinematics and is governed by the c_o^{BH} Fourier coefficient. Assuming that the propagators P_1 and P_2 in numerator and denominator cancel, the beam-spin asymmetry can be approximated at leading twist as

$$A_{LU} \approx \pm\frac{x_B}{y}\frac{s_1^I}{c_o^{BH}}\sin\phi. \tag{2.31}$$

If the above assumptions hold, the beam-spin asymmetry should be dominated by a $\sin\phi$ modulation which changes its sign with the beam charge.

Beam-Charge Asymmetry The beam-charge asymmetry is given by

$$A_C(\phi) \equiv \frac{d\sigma^+ - d\sigma^-}{d\sigma^+ + d\sigma^-}, \tag{2.32}$$

where $d\sigma^+$ and $d\sigma^-$ denote the cross sections measured with a positron and an electron beam, respectively. As the interference term is the only term dependent on the beam charge in equations 2.24 to 2.26, it is the only term left in the numerator. The denominator only contains the charge independent squared BH and DVCS terms. Assuming an unpolarised beam ($\lambda = 0$), only the Fourier coefficients c_n^I appear in the numerator, of which only c_0^I and c_1^I are related to the same leading twist quark GPD, the former is suppressed by an order of $1/Q$ compared to the latter. Further Fourier coefficients appear only at a twist-three level for quark GPDs or at twist-two level for helicity-flip gluon GPDs. The dominating term for the numerator is therefore c_1^I. As for the beam-spin asymmetry the denominator is dominated by the squared BH term at HERMES kinematics. Using the same assumption as before that the BH propagators in denominator and numerator cancel, the beam-charge asymmetry is approximately given at leading twist by

$$A_C(\phi) \approx -\frac{x_B}{y}\frac{c_1^I}{c_o^{BH}}\cos\phi. \tag{2.33}$$

2.5 From Asymmetries to GPDs

At leading twist the beam-spin and beam-charge asymmetries,

$$A_{LU} \sim s_1^I \sin\phi \sim \mathfrak{Im}\, \mathcal{C}_{up}^I \sin\phi \quad \text{and} \tag{2.34}$$

$$A_C \sim c_1^I \cos\phi \sim \mathfrak{Re}\, \mathcal{C}_{up}^I \cos\phi \tag{2.35}$$

are proportional to a modulation of the imaginary and real parts of the DVCS interference amplitude given in equation 2.27. The Compton form factors appearing in this equation are convolutions of a hard scattering amplitude and the twist-two GPDs H, $\widetilde{H}$ and E. The hard scattering parts are calculable exactly in perturbative QCD. Next-to-leading order calculations for DVCS have been carried out [JO98, BM98].

At small values of x_B and t, the dominant contribution to $\mathcal{C}_{up}^I$ originates from the Compton form factor $\mathcal{H}$, as can be seen from equation 2.27. Using the relations

$$\mathfrak{Im}\, \mathcal{H}(\xi,t) = -\pi \sum_q e_q^2 \left(H^q(\xi,\xi,t) - H^q(-\xi,\xi,t)\right), \tag{2.36}$$

$$\mathfrak{Re}\, \mathcal{H}(\xi,t) = \sum_q e_q^2 \left[PV \int_{-1}^{1} H^q(x,\xi,t)\left(\frac{1}{x-\xi} + \frac{1}{x+\xi}\right) dx\right] \tag{2.37}$$

it is possible to gain information on the GPD H. Here PV denotes Cauchy's principal value of the integral. The imaginary part of $\mathcal{H}(\xi,t)$ (and therefore the beam spin asymmetry) is related to the GPD H at $x = \pm\xi$. The x-dependence away from this line is only determinable via the real part, i.e. the beam-charge asymmetry. It is not possible to get from equation 2.37 directly to the quantity $\int_{-1}^{1} H^q(x,\xi,t)\, x\, dx$, which is required for Ji's sum rule. The beam charge asymmetry therefore can only constrain possible GPD models.

Analogous expressions exists for the other Compton form factors $\widetilde{\mathcal{H}}$, $\mathcal{E}$ and $\widetilde{\mathcal{E}}$, which can be accessed through asymmetries measurable on longitudinally or transversely polarised targets.

3 The HERMES Experiment

> "Muse, sing of Hermes, the son of Zeus and Maia, lord of Cyllene and Arcadia rich in flocks, the luck-bringing messenger of the immortals whom Maia bare, the rich-tressed nymph, when she was joined in love with Zeus, –a shy goddess, for she avoided the company of the blessed gods, and lived within a deep, shady cave."
>
> *Homer, Ode to Hermes*

The HERMES experiment was envisaged in 1987 as an experiment to resolve the so called *spin crisis*, after the observations of the EMC collaboration that only a small fraction of the nucleon's spin could be attributed to the spin of it's constituents (see eg. [LA88]). It was commissioned in early summer 1995 as one of the four experiments at the HERA electron[1] proton collider at DESY in Hamburg. As a fixed target experiment it uses the high current electron beam of HERA which has a beam energy of 27.5 GeV together with an internal gas target capable of operation with polarised or unpolarised gases. During the first five years of running (1995–2000) data were taken using atomic gas targets consisting of longitudinally polarised ^{3}He (1995), hydrogen (1996-1997) and deuterium (1997-2000) as well as several unpolarised targets (H_2, D_2, ^{3}He, ^{4}He, N_2, Ne and Kr). For the second phase of data taking (2002–2005) the longitudinally polarised gas target was substituted by a transversely polarised hydrogen target allowing measurements on the so called *transversity* and Sivers distributions and measurements with high density unpolarised hydrogen targets to study exclusive processes *en detail*.

The third and last phase of data taking which started 2006 focuses mainly on the aforementioned exclusive processes. To allow the detection of all particles resulting from the scattering process the HERMES spectrometer (which will be described in this chapter) was extended by a recoil detector, which will be the subject of chapter 5ff.

[1] The HERA accelerator is capable of accelerating and storing electrons as well as positrons. During the following section electron is used for both types of leptons, except when specifically mentioned.

This chapter will give a short overview of the HERA accelerator and the HERMES spectrometer. The HERMES polarised target is described elsewhere in great detail (e.g. [Tai06]) and will be omitted, as it was removed before the installation of the recoil detector.

3.1 The HERA accelerator

The HERA accelerator at DESY in Hamburg was built for precision measurements on the structure of the proton. A superconducting proton storage ring capable of a final energy of 920 GeV and an electron storage ring reaching a maximal energy of 27.6 GeV provide two colliding experiments and two fixed target experiments with beams. The circumference of the accelerator ring is roughly 6.3 km, consisting of four 90° arcs and four straight sections where the experimental halls are located [Sch85]. The beams are brought into collision in the northern and the southern experimental halls, where the experiments H1 and ZEUS are located. Both experiments feature a detector with nearly 4π angular coverage. In the West Hall the experiment HERA-B used the proton beam until 2003. The HERMES experiment situated in the East Hall uses only the electron beam. Both experiments place internal targets into the respective beam. An overview of the accelerators and the experimental halls is shown in figure 3.1 on the facing page.

Before entering HERA the electrons are accelerated in pre-accelerators to an energy of 12 GeV. They are then accelerated in HERA to the final energy by RF cavities operating at 499.667 MHz. The particles are contained in short bunches of a typical length of 9 mm, of which at maximum 220 can be placed inside the storage ring. Typically only 180 of these buckets are filled. The frequency between two buckets, the so called *bunch frequency* is 10.4097 MHz, corresponding to a distance of roughly 28,8 m between successive bunches. Initially a typical beam current of 50 mA is injected into HERA. Due to collisions with residual gas particles in the beam pipes and due to collisions within the beam the beam current decreases exponentially. After typically 8–12 hours the electron beam is dumped from the accelerator at a beam current of about 10 mA.

Electron beams in storage rings experience a self polarising effect due to an asymmetry in the emission of synchrotron radiation. This mechanism is called the *Sokolov-Ternov-Effect* [ST64], which leads to a transverse spin polarisation of the leptons. The maximum achievable polarisation is limited by beam-beam-interaction

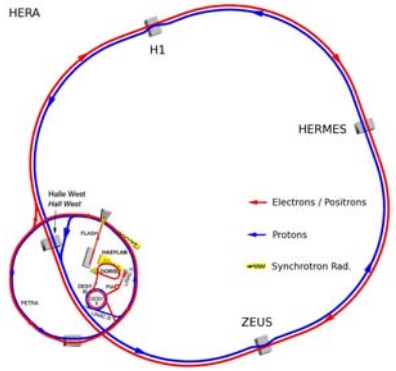

Figure 3.1: The accelerators at the German electron synchrotron DESY in Hamburg. Shown are all accelerators and the three particle physics experiments H1, ZEUS and HERMES.

at the collider experiments as well as non-perfect magnet arrangements. The polarisation is built up exponentially:

$$P_B = P_0 \left(1 - e^{-\frac{t}{t_0}}\right), \tag{3.1}$$

with a maximum polarisation P_0 of around 60% and a typical time constant t_0 of 30 min for HERA. Special magnet arrangements, the so called *spin-rotators*, turn the transverse polarisation into a longitudinal polarisation needed at the experiments and back. These rotators are placed in front and after HERMES (since 1995) and the collider experiments (since 2001).

The polarisation of the beam is monitored continuously with two Compton-Backscatttering-Polarimeters, one located in the west section of HERA monitoring the transverse polarisation (the TPOL, [B+93]) and one in the east section between the spin rotators to monitor the longitudinal polarisation (the LPOL, [B+02]). Both instruments are small calorimeters that measure scattered photons originating from collisions of circularly polarised laser light with the lepton beam. The TPOL uses an asymmetry in the scattering angle with respect to the orbital plane of the electrons,

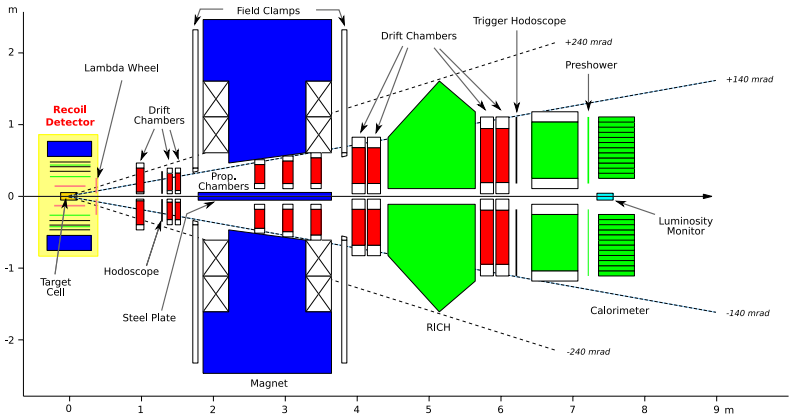

Figure 3.2: The HERMES detectors.

the LPOL an asymmetry in the energy of the backscattered photons. The LPOL reaches a fractional error of 1.6%, the TPOL of 3.4%. For data analyses the value determined by the best working polarimeter is used.

3.2 The HERMES detectors

The HERMES experiment uses a forward spectrometer to detect the reaction products of the interactions of the HERA beam with the internal gas target. During it's lifetime, the HERMES spectrometer has been changed in some details. The following section will describe the state in the years 2006 and 2007, leaving out the recoil detector which will be the subject of the main part of this thesis. A schematic overview is shown in Figure 3.2. A complete description of the original design can be found in [A+98].

The target gas is injected by a gas feed system into a target cell made of 75 µm thick aluminium foil [B+03]. The cell is shaped like an elliptical tube with a length of 150 mm and a cross section with a major axis of 21 mm and a minor axis of 9 mm. A water cooling is integrated in the holding structure of the cell. The cell's ends are

connected via spring fingers to the beam pipe to ensure an electrical continuous enclosure of the beam.

Still inside the vacuum of the beam pipe, the reaction products from scattering processes between the electron beam and the target gas pass a silicon detector, the Lambda-Wheel (LW) [HC98], installed in 2003. This detector consists of two layers of double sided silicon detectors with a thickness of 300 µm arranged in a circular shape. Each disc is made up from 30°-segments and has an inner radius of 7 cm and an outer radius of 17.5 cm. The strip width is 160 µm, which allows a tracking resolution similar to the HERMES spectrometer. In total the LWs provide 20976 readout channels. A thin stainless steel exit window separates the vacuum chamber from the outside atmosphere.

The main spectrometer is divided in two halves to allow the electron and proton beam pipes to pass the experiment. The first detector the reaction products pass after the LWs is the Drift Vertex Chamber (DVC), which, together with the LWs, allows tracking outside the standard HERMES acceptance. This chamber consists of six planes with the configuration XX'UU'VV'[2] with in total 1088 wires. The following Front drift Chambers (FCs) provide information on partial tracks inside the standard acceptance in the front of the spectrometer magnet. As the DVC the FCs feature six layers with an orientation UU'XX'VV' and in total 2304 channels.

About 2 m downstream of the interaction region a spectrometer magnet deflects the charged reaction products with a field of an integrated strength of $\int B\,dl = 1.3$ Tm. Inside this magnet three multi-wire proportional chambers with a moderate spatial resolution have been installed (Magnet Chambers (MCs)). The beam pipes are shielded from the magnetic field by a 11 cm thick steel plate. Still remaining effects on the beams are compensated by a correction coil. In front and behind the magnet, the field is contained by field clamps. The steel plate inside the magnet limits the minimal vertical acceptance of the spectrometer to ±40 mrad.

The tracks behind the magnet are measured by a series of Back drift Chambers (BC 1 to 4), which also have six planes each in an orientation of UU'XX'VV'. In total 7680 channels are read out from the BCs. Between BC 2 and 3 a dual radiator Ring Imaging Čerenkov Counter (RICH) provides particle identification data which allows to distinguish between pions, kaons and protons [A+02]. Čerenkov detectors are based on the effect that particles inside a dielectric medium with a refractive index

[2] The HERMES coordinate system is: z-axis is beam direction, y-axis is upward. In the chambers a wire configuration X corresponds to vertical wires, U and V to wires tilted −30° resp. +30° to the vertical.

n emit radiation if they are moving faster than the speed of light in the respective medium. This Čerenkov radiation is emitted under a characteristic opening angle $\theta_{\check{C}}$ with respect to the direction of the particle's motion. The angle $\theta_{\check{C}}$ is connected to the velocity v of the particle by

$$\cos\theta_{\check{C}} = \frac{1}{\beta n}, \tag{3.2}$$

where $\beta = \frac{v}{c}$ is the ratio of the velocity v to the speed of light in vacuum c. Particles with $\beta < \frac{1}{n}$ do not emit Čerenkov radiation. The number of photons emitted per unit wavelength and unit path length is given by

$$\frac{dN}{d\lambda\, ds} = 2\pi\alpha\left(1 - \left(\frac{1}{\beta n}\right)^2\right)\frac{1}{\lambda^2}, \tag{3.3}$$

which gets maximal if the velocity of the particle approaches the speed of light in vacuum. From this it can be seen that scattered electrons at any momentum will always produce a higher light output and a wider opening angle than hadrons at the same momentum.

A RICH uses a special mirror system to produce an image of the opening angle on a plane that is covered with photomultiplier tubes or other photo detectors. From the ring shaped image of the light cone the opening angle is reconstructed and together with momentum information the particle can be identified. As only a few photons per ring are collected and multiple tracks can overlap, the Particle Identification (PID) efficiencies of a RICH depend on the track multiplicities. The HERMES RICH uses two different radiators, a 5 cm thick layer of Aerogel with a refractive index of $n = 1.03$ at the upstream end of the detector and C_4F_{10}-gas with a refractive index of $n = 1.0014$ filling the space between the Aerogel layer and the spherical mirror. This dual radiator approach improves the PID capabilities with respect to a single radiator RICH as it allows PID over a larger momentum range [HERMES05].

A Transition Radiation Detector (TRD) and an electromagnetic calorimeter are the last two detectors the reaction products pass. The TRD consists of six modules, each containing a radiator with plastic fibres as radiator material and a gas filled proportional chamber with vertical wires. Particles passing through the boundary of two materials with different dielectric constants produce transition radiation, whose intensity is given by $I = m\gamma$. As both leptons and hadrons deposit energy by

ionisation in the chamber gas, but the leptons produce a much higher amount of transition radiation due to a higher γ, this detector also provides important particle identification data and allows the separation of pions from electrons with a rejection factor of 150 at 90% electron efficiency.

The electromagnetic calorimeter consists of two arrays of 42×10 lead glass blocks with a front area of 9×9 cm^2 and a length of 50 cm. It provides energy measurements for leptons and photons and also allows to separate hadrons which have a lower energy deposition at the same particle momentum due to a different shower evolution. The calorimeter suppresses pions by a factor $\geqslant 10$ at the first level trigger and $\geqslant 100$ in offline analyses.

Scattered electrons leaving the target under a very shallow angle can be detected by the luminosity monitor situated at the z-position of the calorimeter in close proximity to the beam pipe. This detector gives information on the obtained luminosity and also provides some trigger signals.

The HERMES acceptance is determined by the covered area of the above described tracking chambers. The tracks also have to pass the opening of the spectrometer magnet and have to hit the calorimeter to induce a trigger signal and allow particle identification. Due to the non-negligible length of the target cell the overall acceptance of the HERMES spectrometer is rather complicated. A good approximation is given in terms of the angles θ_x and θ_y calculated from the momentum components p_x, p_y and p_z of a charged track:

$$\theta_x = \arctan\left(p_x/p_z\right), \tag{3.4}$$
$$\theta_y = \arctan\left(p_y/p_z\right). \tag{3.5}$$

The acceptance by this approximation is then given by $|\theta_x| < 170$ mrad and 40 mrad $< |\theta_y| < 140$ mrad.

All tracking detectors are aligned using a laser alignment system. Additional alignment runs taken with the spectrometer magnet turned off supplement the alignment data and allow to align front and back chambers with respect to each other. Tilts and offsets of the whole detector with respect to the beam cannot be seen using internal alignment, but can be deduced from their effects on the reconstructed beam position and from offsets to the calorimeter.

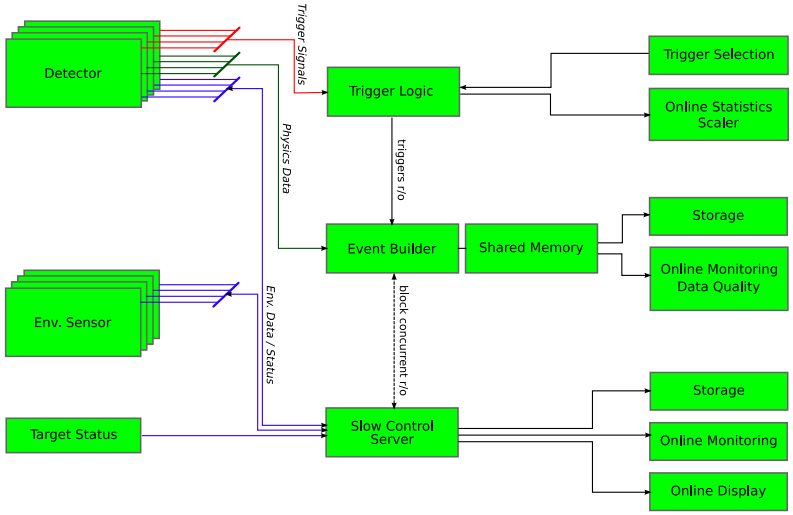

Figure 3.3: A simplified schematic of the HERMES DAQ system.

3.3 The HERMES Data Acquisition System (DAQ)

The HERMES data acquisition system is split into fast information (physics data) and slow information (sub-detector status messages, environmental data, etc.). Both data flows are read out separately and only merged in an offline stage. The following will give a short simplified overview on both data flows, as depicted in Figure 3.3 on the facing page. As the system was extended continuously during the lifetime of the experiment, several additions have been made to the original architecture with more recent electronics; a general description will always give rise to some exceptions, which will not be covered in this text.

A physics trigger is generated by a combination of fast detector signals coming from the hodoscopes; additional conditions can be a single cluster in the calorimeter or a signal in the luminosity monitor. Various non-physics triggers are available, as e.g. a signal noting the first bunch in the HERA bunch train. The required trigger for read out is set in the *trigger mask*, which is a 32-bit pattern selecting from trigger condition combinations. Various scalers monitor the occupancy of each trigger source.

On the arrival of a trigger matching one of the selected triggers by the trigger mask, the physics data digitised by Analog Digital Converters (ADCs) are transferred via a VME or Fast-Bus system to a First-In First-Out (FIFO) memory in each crate. The *event builder*, a Digital Signal Processor (DSP) acting as the interface between the various detector crates and the joined HERMES read out, then collects the data from each of these FIFOs and builds a common data structure, which is then transferred to a shared memory. Each triggered event is then stored on computer hard-disks and subsequently on tape, using the EPIO data format, which is provided by the CERN Software Library [CER02]. A sub-sample of the events in the shared memory is also read by on-line data quality monitoring tasks and on-line displays, including *wire-maps* which show the occupancies of each detector and *physics plots* which show quantities related to the measured physical processes, e.g. the reconstructed vertex position.

Various timescales segment the physics data taken. Every ten seconds information from scalers – like the luminosity determined by the luminosity monitor and the trigger dead-time – is included in the event stream in a *scaler event*. This ten second period is called a *burst*. If the file size of the data taken reaches 560 MB the file is closed and a new one is opened; this completes one *run*. The time between ramping up the electron beam and dumping it is called one *fill*, this usually takes about 8–12

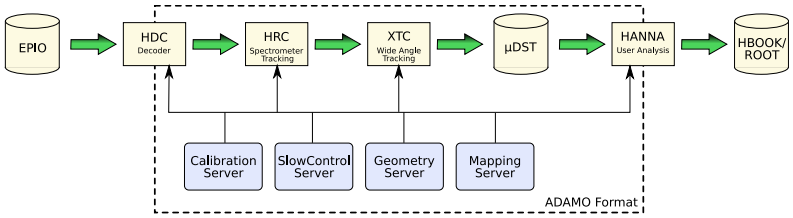

Figure 3.4: The HERMES software chain from raw data to physics analyses.

hours.

The slow control data flow is built around a client-server principle [W+95]. A central server collects and distributes the information of various hardware related clients. These hardware clients are reading out and controlling the detectors and environmental sensors, the read out happening around once every ten seconds. Monitoring clients are surveying the function of the detectors and the environmental conditions; these clients can either trigger alarms or issue commands to the hardware clients to take actions in case of deviation from the standard operational parameters. All important slow control data is shown in the control room on terminals by clients written in an extension to the TCL/TK scripting language, called PinK [A+95]. These clients, the so called *Pinkies*, inform the shift crew about the status of the experiment and allow to control it by issuing commands to the hardware clients. The monitored data, like voltages, temperatures, pressures, target status etc., are written to disks and to tape in an ADAMO database using the GAF format (for a description of the ADAMO system see [CER02]).

3.4 The HERMES analysis chain

The analysis chain as shown in Figure 3.4 is completely based on the ADAMO database format. The EPIO data coming from the DAQ system, which contains the raw data from each detector, is converted to an ADAMO database containing various tables for the sub-detectors. Each of these tables contains the calibrated response for the complete sub-detector. The conversion is done by a software called

HERMES decoder (HDC), which reads the calibration information from slow control servers. Mapping servers provide information on the mapping of a physical detector channel to a logical detector ID. HDC uses also geometry information provided by geometry servers to calculate space points from the raw detector information.

The decoded data is written into a UNIX pipe (or many, as the software chain can run in multiple instances in parallel) from where it is read by the HERMES reconstruction program (HRC). HRC is responsible for reconstructing tracks in the spectrometer using a tree-search algorithm [Wan96]. It reconstructs tracks in the front and the back region independently, using the signals of the wire chambers; as these regions contain no magnetic field a straight line is used to describe the tracks. Those partial tracks are then projected to the center of the magnet and if they join are declared to be a full track; each hit in the detectors is assigned to the corresponding track. From the reconstructed bending angle inside the magnet, momentum and charge are determined. The data of the hodoscopes, the TRD and the Calorimeter is used to identify the particles. At this stage the slow control data is joined with the physics data.

Data belonging to the Lambda-Wheel and the recoil detector are handed through HDC and are treated by a second tracking step. The extended tracking code, short XTC, reconstructs tracks outside the standard acceptance. As there is only very little overlap between the spectrometer and the Lambda-Wheel together with the Recoil Detector, this tracking code is independent of HRC. The LW tracks are assumed to be straight lines originating from the target region. The tracking code for the recoil detector is somewhat more complicated, the recoil detector being a small spectrometer on it's own.

The tracked data is now written on disk (and tape) into micro Data Summary Tape (µDST) files. From these files all user analyses start. All µDST files of a running year are called a production, designated by the year and a letter noting the number of iterations it has passed[3]. A user analysis uses the HANNA (HERMES analysis) framework to access the µDST files which are in the ADAMO database format. The data produced by these analyses is then usually stored in HBOOK [BG] or ROOT format [BR+97] and processed further in the PAW [BBC+87] or ROOT frameworks.

[3] The first data production without any corrections is the *a* production, after application of corrections the *b* production is created, and so on.

4 DVCS measurements at HERMES

"Where am I? What's that in there? Are those *my* feet?"
Father Jack Hacket (Frank Kelly) in the Series Father Ted

Various studies on Deeply Virtual Compton Scattering off different targets have already been done by the Hermes collaboration. Figure 4.1 sketches the particle paths for a typical event in the Hermes spectrometer. The scattered lepton and the created real photon pass the spectrometer in forward direction, while the recoiling nucleon leaves the target cell under large angles to the beam direction. As the recoiling nucleus cannot be measured by the spectrometer, all the analyses done so far were based on missing mass reconstruction, using information from the spectrometer to reconstruct the mass and momentum of the recoiling particle. The missing mass squared is given by

$$M_x^2 = \left(\mathbf{v}^* + \mathbf{P} - \mathbf{v}\right)^2, \tag{4.1}$$

where $\mathbf{v}^*$, $\mathbf{P}$ and $\mathbf{v}$ denote the four-momenta of the virtual photon, the target nucleon and the real photon respectively. Assuming that the proton stays intact and the real photon is the only particle produced, this missing mass should equal the mass of the proton M_p.

The results obtained by the missing mass method are limited by the spatial and energy resolution of the spectrometer so that only the leading asymmetry moments can be determined.

4.1 Beam Charge and Beam Spin Asymmetry

The Beam Charge Asymmetry (BCA) and Beam Spin Asymmetry (BSA) in DVCS on unpolarised hydrogen with a polarised electron/positron beam are treated in [Ell04]. These asymmetries are proportional to the real and imaginary part of the

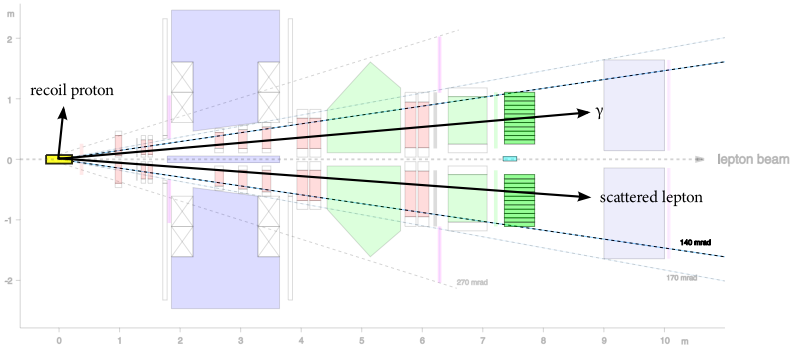

Figure 4.1: Sketch of the particle paths in a typical DVCS event.

Compton form factor $\mathcal{H}$, namely

$$A_C = \frac{N^+(\phi) - N^-(\phi)}{N^+(\phi) + N^-(\phi)} \propto \frac{\Re\mathrm{e}\,\mathcal{H}}{F_1} \cdot \cos\phi \tag{4.2}$$

for the Beam Charge Asymmetry and

$$A_{LU}(\phi) = \frac{1}{\langle|P_B|\rangle} \frac{N^{\rightarrow}(\phi) - N^{\leftarrow}(\phi)}{N^{\rightarrow}(\phi) + N^{\leftarrow}(\phi)} \propto \frac{\Im\mathrm{m}\,\mathcal{H}}{F_1} \cdot \sin\phi \tag{4.3}$$

for the Beam Spin Asymmetry. The superscripts at the counting rates N represent the beam charge resp. polarisation. The results published in [HERMES07] for the BCA are shown in Figure 4.2(a). Shown is the dependence of the Beam Charge Asymmetry A_C on the absolute value of the azimuthal angle ϕ, thus showing only cosine moments. The first cosine moment of the BCA has been determined to:

$$A_{C,\mathrm{Proton}}^{\cos\phi} = 0.063 \pm 0.029(\mathrm{stat.}) \pm 0.026(\mathrm{sys.}). \tag{4.4}$$

The missing mass dependency of the BCA is shown in Figure 4.2(b). Due to the bad resolution of the HERMES spectrometer for the scattered photon the missing mass range considered to contain exclusive events is quite large: $-1.5 < M_x < 1.7$. Figure 4.3 on the facing page shows the t-dependence of the $\cos\phi$ amplitude of the

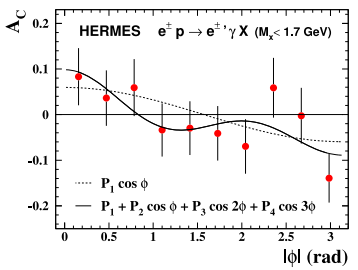

(a) Beam Charge Asymmetry A_C as a function of absolute value of the azimuthal angle ϕ.

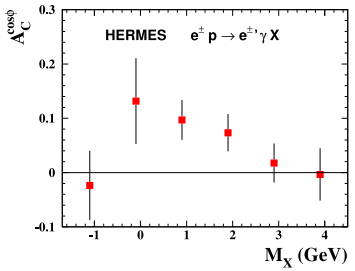

(b) The $\cos\phi$ moment of the BCA as a function of missing mass.

Figure 4.2: HERMES results on the Beam Charge Asymmetry (BCA) for DVCS on the proton as published in [HERMES07]. The error bars represent statistical uncertainties.

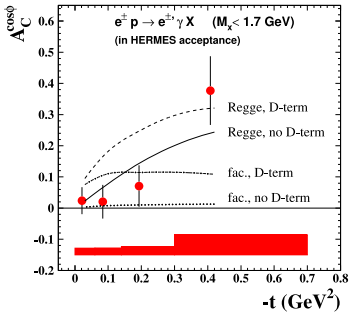

Figure 4.3: The $\cos\phi$ amplitude of the BCA as a function of $-t$. The error bars represent the statistical uncertainties, the error band represents the systematical uncertainties. The curves represent four different parameter sets for GPD models described in [GPV01] and [VGG99].

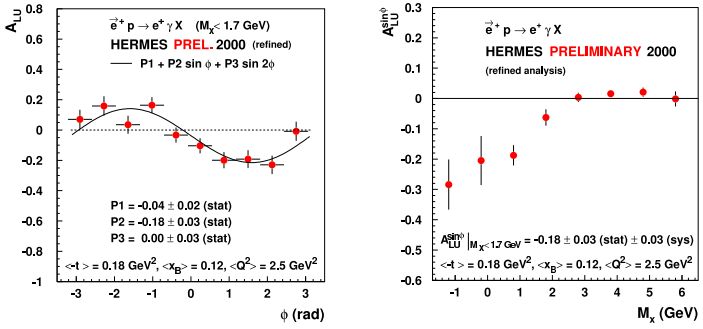

(a) Beam Spin Asymmetry A_{LU} as a function of the azimuthal angle ϕ.

(b) The $\sin\phi$ moment of the BSA as a function of missing mass.

Figure 4.4: HERMES results on the Beam Spin Asymmetry (BSA) for DVCS on the proton as published in [HERMES01]. The error bars represent statistical uncertainties.

Beam Charge Asymmetry. Also shown are theoretical calculations based on models developed in [GPV01] and [VGG99] with different parameter sets.

The results for the BSA using a longitudinal polarised target and an unpolarised beam have been published in [HERMES01] and are shown in Figure 4.4.

4.2 Transverse Target Spin Asymmetry

The Transverse Target Spin Asymmetry (TTSA) is the sole asymmetry where the GPD E is not suppressed:

$$d\sigma(e^+, p^\uparrow) - d\sigma(e^+, p^\downarrow) \propto \Im\mathrm{m}\ [F_2\mathcal{H} - F_1\mathcal{E}] \cdot \sin(\phi - \phi_s) \cdot \cos\phi + \dots . \tag{4.5}$$

Together with the GPD H determined from the BCA and BSA the GPD E gives access to the total angular momentum of the quarks inside the proton via Ji's sum rule. The TTSA is measured as:

$$A_{UT}(\phi, \phi_S) = \frac{1}{\langle |P_T| \rangle} \frac{N^\uparrow(\phi, \phi_S) - N^\downarrow(\phi, \phi_S)}{N^\uparrow(\phi, \phi_S) + N^\downarrow(\phi, \phi_S)}, \tag{4.6}$$

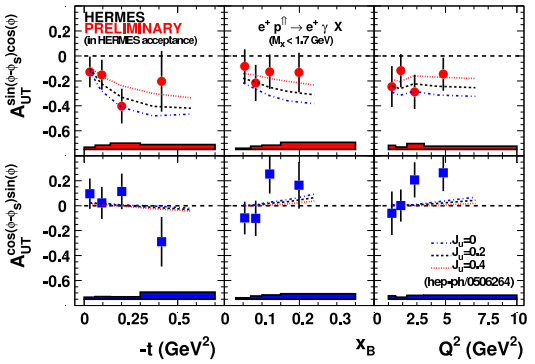

Figure 4.5: HERMES results on the $A_{UT}^{\sin(\phi-\phi_S)\cos\phi}$ and $A_{UT}^{\cos(\phi-\phi_S)\sin\phi}$ moments as function of $-t$, x and Q^2 compared to the predictions in ref. [ENVY06] based on the model described in [GPV01].

where ϕ_S is the angle between the target polarisation direction and the lepton scattering plane The superscripts at the count rates represent the transverse target polarisation. Expanding the first moments gives:

$$A_{UT}(\phi, \phi_S) \approx A_{UT}^{\sin(\phi-\phi_S)\cos\phi} \cdot \sin(\phi - \phi_S)\cos\phi + A_{UT}^{\cos(\phi-\phi_S)\sin\phi} \cdot \cos(\phi - \phi_S)\sin\phi. \tag{4.7}$$

Figure 4.5 shows the measurements in [Ye06]. The lines represent model calculations for various values of J_u with $J_d = 0$. It can be seen that only the term $A_{UT}^{\sin(\phi-\phi_S)\cos\phi}$ is sensitive to J_u. A model-dependent constraint on J_q is shown in Figure 4.6 on the next page.

4.3 Longitudinal Target Spin Asymmetry

From the Longitudinal Target Spin Asymmetry (LTSA) A_{UL} information on the GPD $\widetilde{H}$ can be gathered:

$$A_{UL} = \frac{1}{\langle |P_T| \rangle} \frac{N^\leftarrow(\phi) - N^\rightarrow(\phi)}{N^\leftarrow(\phi) + N^\rightarrow(\phi)}, \tag{4.8}$$

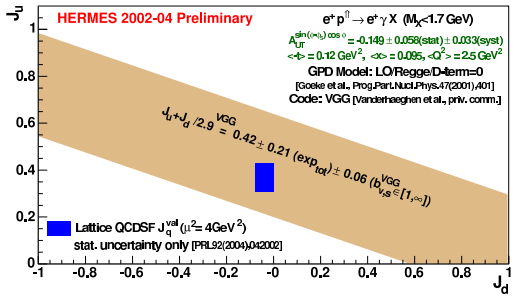

Figure 4.6: Model-dependent constraint on J_u and J_d obtained by comparing the extracted TTSA amplitude $A_{UT}^{\sin(\phi-\phi_S)\cos\phi}$ and the theoretical predictions based on the GPD model proposed in [GPV01]. The blue area shows the lattice QCD result obtained by the QCDSF collaboration for the scale $\mu^2 = 4$ GeV^2 for valence quark contributions only.

the superscript denoting the target spin (← positive orientation. Note that positive target spin is anti-parallel to the beam direction.) Rewriting the asymmetry as a sum of harmonics in $\sin\phi$ the amplitude can be approximated by:

$$A_{UL} \approx A_{UL}^{\sin\phi} \sin\phi + A_{UL}^{\sin 2\phi} \sin 2\phi \tag{4.9}$$

The $\sin\phi$ moment $A_{UL}^{\sin\phi} \sin\phi$ is sensitive to the imaginary part of $\widetilde{\mathcal{H}}$ at a level of twist-two. All dependencies on other Compton form factors are suppressed at least to a level of twist-three. The results on A_{UL} obtained in [Kop06] are shown in Figure 4.7 on the facing page.

4.4 Asymmetries on heavier targets

The versatility of the Hermes gas target allows also to study DVCS on heavier nuclei. In [Kra05] all asymmetries associated to the interference between the BH process and DVCS on a longitudinally polarised deuterium target with a polarised electron/positron beam have been extracted. A clear evidence for a beam spin and a

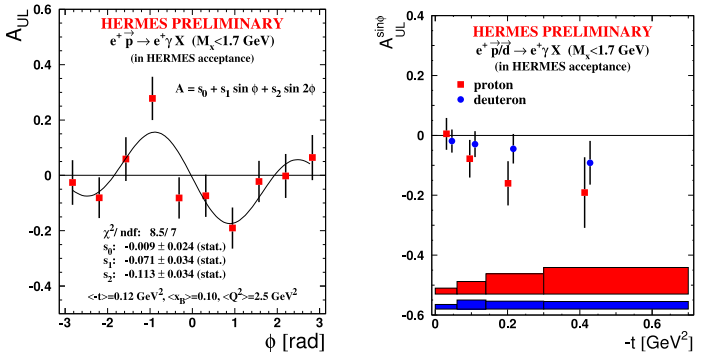

(a) Longitudinal Target Spin Asymmetry A_{UL} for the proton as a function of the azimuthal angle ϕ.

(b) The $\sin\phi$ moment of the LTSA for protons and deuterons as a function of t.

Figure 4.7: Hermes results on the Longitudinal Target Spin Asymmetry (LTSA) for DVCS.

beam charge asymmetry due to the interference between BH and DVCS has been found. Figure 4.8 shows the first cosine moment for the Beam Charge Asymmetry A_C as an example.

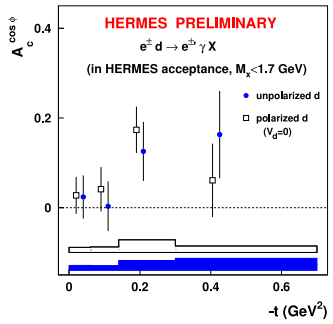

Figure 4.8:
The first cosine moment of the BCA on vector polarisation balanced (i.e. vector polarisation approx. 0, tensor polarisation approx. 1) deuterium and unpolarised deuterium as function of t (Plot taken from [Kra05]).

4.5 Requirements for a Recoil Detector.

These examples illustrate the possibility to constrain Generalised Parton Distributions already from existing HERMES data on DVCS. In order to obtain a higher accuracy in the determination of these asymmetries an addition to the HERMES spectrometer is needed to also detect the recoiling particle and therefore eliminate the uncertainties from the missing mass determination. The requirements for a Recoil Detector have been studied in [Kra00, Kra05]. The main purpose of this detector is the positive identification of recoiling protons emitted in hard exclusive photon or meson production. The angular resolution of this recoil detector is mainly determined by the angular resolution of the HERMES spectrometer and has been calculated in [Kra00] to be sufficient when the angle ϕ_P of the proton around the direction

of the lepton beam is known better than 0.1 rad. The resolution for the transverse momentum component needs to be smaller than 10%.

Figure 4.9 depicts the momentum and angular distribution of protons originating from various hard processes; panel a shows protons from pure DVCS, panel b from the interference between Bethe-Heitler process and DVCS, panel c and d from ρ meson resp. Δ resonance production. Also shown are the acceptances of the Silicon and the Scintillating Fibre Detector of the HERMES Recoil Detector, which were chosen according to the distributions. It can be seen that a large angular acceptance is needed in addition to the ability to measure the momentum over a very large range. Most protons from the DVCS process are generated with angles between 0.5 rad to 1.3 rad and momenta between 50 MeV/c and 600 MeV/c. Protons from the decay of Δ resonances have momenta below 1.4 GeV/c, pions typically have momenta below 800 MeV/c. The desired coverage of the Recoil Detector therefore needs to include momenta from as high as 1.4 GeV/c to a momentum as low as possible and an angular coverage from 0.1 rad to 1.35 rad. To obtain the high dynamic range for momentum detection energy information on a large energy range is needed from the detectors in addition to spacepoints for tracking. As the detector needs only to register events where the scattered lepton and/or the generated photon or meson are registered with the spectrometer, no trigger output from the Recoil Detector is required. A more detailed treatment on the requirements on the Recoil Detector as well as the chosen design are found in [HC01].

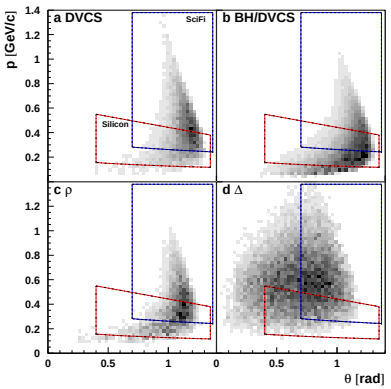

Figure 4.9: The angular and momentum distribution of DVCS and background processes.

5 The Recoil Detector

❝Never worry about theory as long as the machinery does what it's supposed to do.❞
Waldo & Magic, Inc. – Robert A. Heinlein

The Recoil Detector was the last upgrade to the Hermes experiment before it's shutdown end of June 2007. To allow the studies of GPDs and DVCS with greater accuracy than before it was necessary to detect the recoiling proton in addition to the scattered lepton and the produced photon already detectable with the Hermes spectrometer. Therefore a small complete spectrometer had to be constructed around the target cell which had to fit in the restricted space of the target region [HC01]. The detector needed to be able to provide tracking and momentum information on the recoiling particle as well as particle identification to suppress the influence of background events.

5.1 Design of the detector

Figure 5.1 gives an overview of the Recoil Detector. Around the target cell 16 silicon sensors are arranged in two layers in a diamond like shape still inside the HERA vacuum. Directly outside the vacuum chamber a scintillating fibre detector consisting of four layers of fibres is located. The outermost detector is a three layer Photon detector. All detectors are located inside a superconducting solenoid (not shown in the picture) with a field strength of 1 T at its centre.

The scintillating fibre detector [Hoe06] consists of four layers (two *barrels* of two layers each) composed by more than 7000 fibres; two layers are orientated parallel to the beam, two are offset by 10° (referred to as *stereo layers*). Each barrel consists of one parallel and one stereo layer, allowing to reconstruct space points for particle tracks passing the detector. Due to space constraints no external housing was possible and the detector is mechanically self supporting. The two barrels are placed at the maximum possible distance from each other, the inner just outside the

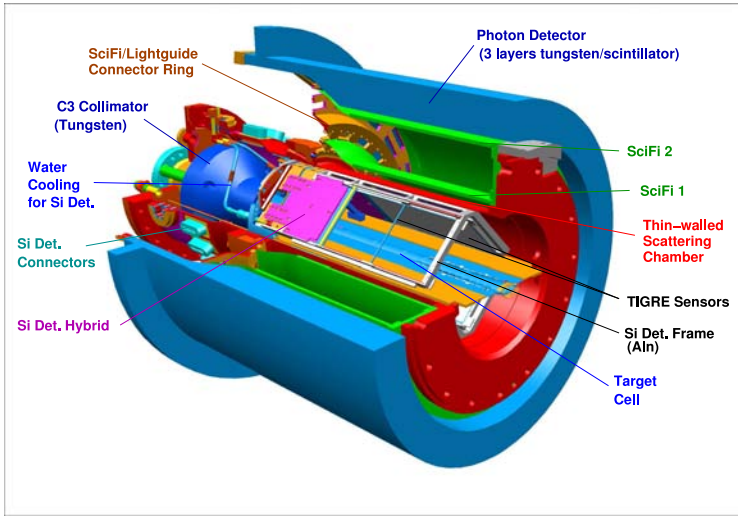

Figure 5.1: General Scheme of the HERMES Recoil Detector.

scattering chamber, the outer barrel closely fit into the Photon Detector. The fibres are read out at the upstream end of the detector using 4 m long transparent light guides connected to multi-anode photo-multiplier tubes. The read out electronics is based on GASSIPLEX read out chips [KBF+99], which integrate over multiple HERA-bunches. To separate hits originating from different bunches the dynode signals of the photo-multipliers are read out by a TDC. In conjunction with the silicon detector the scintillating fibre detector provides the necessary tracking and energy information to identify recoiling particles and determine their kinematics.

The photon detector [vH07] is designed primarily to detect photons originating from decays of Δ^+ resonances. Two decay channels of the Δ^+, namely $\Delta^+ \to p\pi^\circ$ and $\Delta^+ \to n\pi^+$ involve hadrons which could be wrongly identified as direct products of a DVCS process. To distinguish them from direct DVCS products, the produced π meson needs to be detected and identified. The π^+ in the second decay channel can be identified by the scintillating fibre detector, but for the identification of the photons originating from $\pi^\circ \to \gamma\gamma$ or $\pi^\circ \to \gamma\gamma\gamma$ an additional detector is necessary. This photon detector is based on a segmented shower detector design. It consists of three layers of tungsten as converter material for the photons alternating with three layers of plastic scintillators. The inner converter layer has a thickness of 6 mm corresponding to two radiation lengths; the outer two layers have a thickness of one radiation length (i.e. 3 mm). The scintillator layers are segmented; the inner layer consists of 60 strips of 2 cm width and 1 cm thickness parallel to the beam axis, the outer two layers are made of 44 strips of the same cross section but inclined by $\pm 45^\circ$ with respect to the beam axis. Although only very coarse, this spatial resolution allows to detect and reconstruct the decay products of the π° with sufficient accuracy. Each scintillator is read out via two wavelength shifting fibres, which are connected to multi-anode photo-multiplier tubes outside the magnetic field of the recoil magnet.

The recoil magnet consists of two superconducting Helmholtz-Coils immersed in a liquid helium bath. At the centre of the bore it provides a field of 1 T. An iron yoke supports the magnet mechanically and attenuates the field on the outside to a field strength of less then 0.002 T in 2 m distance of the bore. Inside the bore a field homogeneity of better than 20% is achieved.

5.2 The Silicon Counters

The silicon counters of the HERMES Recoil Detector are located inside the vacuum of the target chamber. They consist of 16 silicon sensors arranged in 8 modules which are surrounding the target cell in two layers arranged in a diamond like shape.

The silicon sensors are read out and controlled with HELIX 3.0 serial read out chips [FB98, Tru00]. The Silicon Detector has 128 strips per sensor side and 4096 strips in total, so that a serialised read out is needed to keep the number of signal lines in a feasible region. The HELIX 3.0 chips on the silicon modules are steered via the HeLix Control Unit, short HLCU. The data coming from the silicon is digitised by the HERMES-ADC (or HADC). Figure 5.2 illustrates the functions of the different hardware parts.

A module named ACC (Analogue Clock Control) is responsible for the merging of the signal lines into one cable to the silicon modules and also for the refreshing of the signals. Silicon modules and ACC get their supply voltages from special LV modules, Bias Voltage for the silicon sensors is supplied by a CAEN mainframe.

Most of the readout hardware has been developed for the Lambda-Wheels, a silicon detector in the HERMES front region. The already available knowledge and experience from the Lambda-Wheel Group and the lack of development time led to the decision to use this technology [KLS+02].

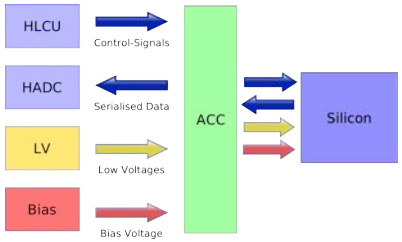

Figure 5.2: Functional schematics of the Silicon Detector.

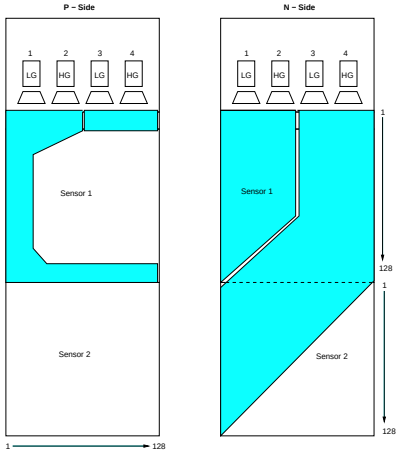

Figure 5.3: Schematics of a silicon module. The n-side strips are horizontal, the p-side strips vertical in this picture.

5.2.1 The modules

The complete silicon detector consists of 8 single modules mounted in two layers on two roof-like structures (called *Dächer*). The modules are constructed from a ceramic holding frame on which the two silicon sensors are mounted, connected to an aluminium heat sink on which the read-out hybrids are fit. Figure 5.3 depicts a schematic view of a module. The strips on the n-side are horizontally, the p-side strips vertical in this picture. At the top the four HELIX chips can be found. The shaded area designates the Kapton foils supporting the conductive paths connecting the sensors with the read out chips.

Due to the strict time constraints in the development of the HERMES Recoil Detector only existing designs for silicon sensors were taken into consideration. The TTT design of Micron Semiconductors Ltd, Sussex, fitted best the requirements of the recoil detector. These sensors were produced in a six inch wafer technology and provided the necessary resolution of better than 1 mm while on the same time covering a large area. The sensors were originally developed for the TIGRE Gamma-

Ray telescope [O+03].

The sensors are square shaped with a side length of 9.9 cm , providing an active area of 97.3 × 97.3 mm², with a thickness of 300 µm. Both sides are segmented into 128 strips, the p-side strips perpendicular to the n-side strips. The strip width is 758 µm. Some minor changes to the original design by Micron were made: the bias resistors were changed to 7.5 MΩ (p-side) resp. 6 MΩ (n-side) and the thickness of the oxide layer was changed [Kra05]. Both modifications were needed to operate the TIGRE sensors under high background conditions. Occasional peaks in the radiation in a storage ring can lead in the generation of large amounts of free charges inside the depletion zone. These charges effectively shorten the detector and would lead to a large voltage drop accross the coupling capacitors. Thickening the oxide layer reinforces the capacitors and allows them to withstand higher voltage drops. The bias resistance defines the time constant of the detector. The TIGREs original bias resistance of 50 MΩ would lead to a time constant of about 2.5 ms which would result in a charge pile up in the detector in the HERA environment. The lowered resistance results in a time constant of 0.38 ms, thus preventing the charge pile up for event rates lower than 1 kHz per strip.

The strip implants with p-doping on the junction side (p-side) were created by boron doping using an ion implantation density of $2.0 \cdot 10^{15}$ cm^{-2}, the n-implants on the p-side by phosphorous doping using an ion implantation density of $5.0 \cdot 10^{14}$ cm^{-2}. However, as these implantations were done through a thin oxide layer, which is then subsequently removed, and with an ion beam whose energy is not published by Micron Semiconductors it is impossible to calculate mean volume densities from these numbers. After the p-doping of the strip implants, and the creation of bias- and guard-ring the capacitor oxide is added to the sensor. Bias-resistors and the bases of the bond pads are created by adding a poly-silicon layer. After adding the aluminium layer for bond pads and charge collection lines, a thin passivation layer is put on top to protect most of the detector.

The geometrical shape of the strip implants is strictly rectangular. They are covered with a grid shaped metal mask for the charge collection. Each strip features two bond pads for AC-coupling, which are supported by a 0.8 µm poly-silicon layer in order to prevent the bonding procedure to damage the dielectric (silicon oxide). In addition each strip has an implant pad, which allows to connect directly to the implant layer below.

The guard and bias rings can be connected at all four corners of the sensor. There are two holes per ring in the passivation layer at each corner. It is possible to

distinguish p- and n-side by looking at these holes: on the p-side there are bond-pads on the guard- and bias-ring in front of the coupling capacitor pads. On the n-side they are only on the sides. The p-side also has an additional broad metallised ring outside the guard ring. It sits on top of an n^+-doped region and can be used to test the p-n-junctions if no contact to the backside is possible.

The n-side is similar to the p-side in setup, but has a slightly more elaborated doping. The nominal ion beam density for the n-implant is $5.0 \cdot 10^{15}$ cm^{-2}, the nominal ion beam density for the p-implant is $5.0 \cdot 10^{14}$ cm^{-2}. The p-mask is rather complicated, as the strips have no natural separation by p–n-junctions. To compensate for this a p-stop ring is laid around all strips and one p-stop ring is laid around each individual strip. Thus strip separation is only achieved when the detector is fully depleted. The strip number one can be found on the right side when the capacitor pads face the viewer. The strips are marked with crosses as on the p-side, starting at strip one every 16$^{\text{th}}$ strip. An overview of the TIGREs properties can be found in table 5.1.

Table 5.1: The properties of the TIGRE detectors.

detector size	99 × 99	mm²
active area	97.3 × 97.3	mm²
thickness	300	µm
strip width	758	µm
inter-strip distance	56	µm
coupling capacitance	850 – 900	pF
inter-strip capacitance	9	pF
bias resistance p-side	7.5	MΩ
bias resistance n-side	6	MΩ
depletion voltage	~ 50	V

5.2.2 The Readout Chips

To minimise the large number of channels which needs to be read out from a silicon detector, a serialising read out chip is generally used. This chip reads out the charge of all channels in parallel, stores it in an intermediate array of capacitors and feeds the charge then serialised channel by channel to the read out ADCs. Two serial

read out chips were specially developed for experiments at the HERA storage ring: the APC, used and developed at the experiment H1, and the HELIX series of chips developed for HERA-B and also used at ZEUS and HERMES. The first prototype for the Recoil Silicon Detector used the APC chips [Ste98a, Ste98b, V+04]. For the final design the HELIX 3.0 chip was chosen due to technical advantages and available expertise, as this chip-family is also used for the read out of the Lambda Wheels [KLS+02].

The HELIX chip family is extensively described in references [Tru00, FB98], here only a short overview will be given. These chips were developed for reading out the HERA-B silicon vertex detector. They were manufactured in a radiation tolerant AMS 0.8 µm CMOS process, to be able to withstand a radiation dose of about 1 kGy. This dose would be acquired during one year of running if the chips are mounted roughly 10 cm off the beam axis in the HERA-B setup. The sampling frequency of the chip is matched to the HERA bunch-crossing frequency of 10.4 MHz, one chip can read out 128 channels with peak sampling input amplifiers whose rise and fall times are shorter than 96 ns to not deteriorate the signals of subsequent bunches. The electronic noise at the input stage is on the order of 400 e^- + 40 e^- / pF for not irradiated chips. A trigger can be provided by the chips using a comparator stage before the pipeline storage cells. The Recoil Detector uses the last generation of this chip, the HELIX 3.0.

Each detector strip is connected to a low noise charge sensitive pre-amplifier and a shaper (the *front-end*) whose outputs are sampled into a storage pipeline with a sampling frequency of 10.4 MHz. The front-end output of each strip is AC-coupled to a comparator, which can provide a trigger signal (this is not used in the HERMES recoil detector setup). Each neighbouring four of these comparators are connected together with an OR-logic, so that in total 32 trigger signals are fed via bond-pads outside of the chip.

The storage pipeline has a depth of 141 clock cycles (128 cells to store events, eight to store already triggered events and six to cover for processing overhead) and a width of 128 + 1 channels (one is an additional "shaper only" channel, which could be used for common mode estimation; in the HERMES setup it is not used). Each storage cell consists of an 850 fF capacitor, which can be connected via a switch to the write- and read-line. Write and read pointers are increased every clock cycle, the difference (in clock cycles) between read and write pointer is set via the *latency* control register.

Upon arrival of a trigger the charge stored in the pipeline cells is retrieved by

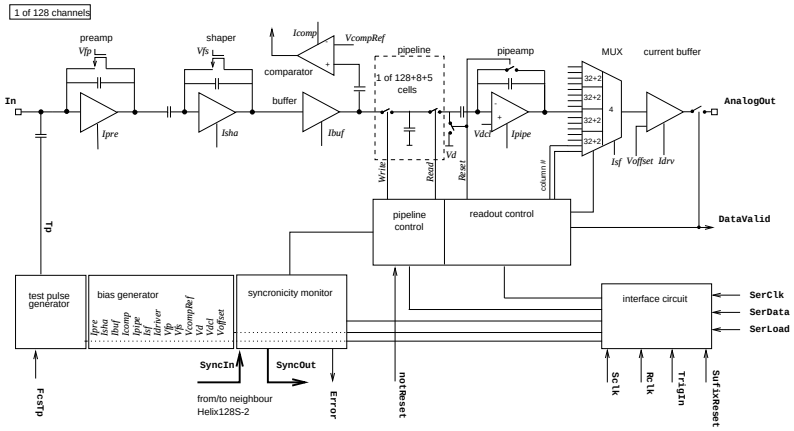

Figure 5.4: Block diagram of the HELIX read out chip.

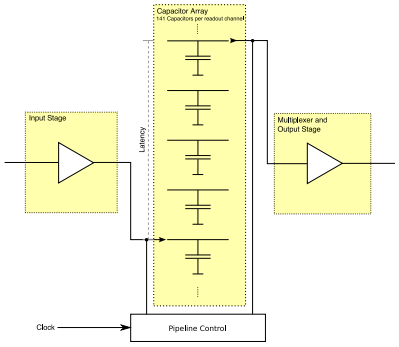

Figure 5.5: Schematic view of the HELIX pipeline storage.

the *pipeline readout amplifier*. This is then fed into a two-stage multiplexer, which subsequently switches the signals of the 128 pipeline readout amplifiers into a single output line. After these signals the address of the pipeline cell is also passed on the signal line (the so called *trailer*). Parallel to the data output the HELIX generates a data valid signal (`Sync-Out`), which is used to signalise the ADC the arrival of data. Daisy chained readout of multiple HELIXes is possible using the `HelixToken` signals. HELIX 3.0 chips have an additional fail-save mechanism that the daisy chained readout works even when one HELIX chip is not passing on the read-out token.

The various voltages and currents of the amplifiers and buffers of the HELIX are set by the registers shown in table 5.2 on the next page. The optimum values for these voltages and currents have been determined in a study with a charge injection device [GHR+05]. Programming the registers is accomplished via a serial interface, which is programmed by 20-bit words. These words are constructed of 8 bits of data to be put in the registers [1], a 5-bit register address [2], a 5-bit chip address [3] and a bit containing a broadcast-flag [4]. If this broadcast-flag is set, all HELIXes in a daisy chain are programmed with the respective values. If not set, only the HELIXes with an address corresponding to the address in the data-word are programmed. The address is assigned to the HELIX by connecting the corresponding bond-pads to +2 V (bit set) and -2 V (bit not set).

5.2.3 The Hybrids

The read-out chips are mounted together with some auxiliary electronics onto a printed circuit board made from Kapton-foil (called the *hybrid*). This Kapton foil also serves as a flexible lead (the *flex-foil*) to connect the hybrid to the feed-through connectors at the beam-pipe.

All signal lines from and to the HELIXes are not directly connected to the outside world. The digital trigger and clock signals are refreshed on the hybrid by LVDS line drivers. These signals are transferred via differential lines to the hybrid. The `SLOAD`, `not-RESET` and the `Sync-Out`-Signal, which are transferred on a single line, are repeated by a simple 2-input or-gate. The analogue output of the HELIX chips

[1] Bits `0x0` to `0x7`, Least Significant Bit is `0x0`
[2] Bits `0x8` to `0xC`
[3] Bits `0xD` to `0x12`
[4] Bit `0x13`

Table 5.2: The HELIX 3.0's internal registers.

Address (HEX)	Name	Description
01	*Ipre*	Pre-amplifier bias current. Influences the input signal peak time and undershoot.
02	*Isha*	Shaper bias current.
03	*Ibuf*	Buffer bias current.
04	*Icomp*	Comparator bias current.
05	*Ipipe*	Pipeline amplifier bias current.
06	*Isf*	Multiplexer bias current.
07	*Idriver*	Output amplifier bias current.
08	*Vfp*	Controls the input amplifier feedback resistance and it's gain.
09	*Vfs*	Controls the shaper feedback resistance, influences peak time and pulse length of signal.
0A	*VcompRef*	Comparator threshold level.
0B	*Vd*	Reset level of the pipeline amplifier.
0C	*Vdcl*	"Ground" level of the pipeline amplifier.
0D	*Voffset*	"Ground" level of the output amplifier.
11	*Latency*	Used storage depth of the pipeline.
12	*SyncReg*	Controls the generation of the *sync out* signal.
13	*ClkDiv*	Controls the generation of fail-save tokens and position in the daisy chain.
14	*TokenDelay*	Delay between receiving the daisy chain token and sending the data.

is fed through a MAX435 amplifier before it leaves the hybrid. To monitor the module conditions a PT1000 thermal resistor is mounted on the p-side hybrids and a radiation sensitive field effect transistor is mounted on the n-side.

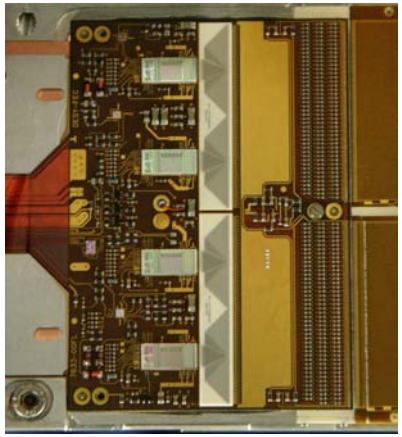

Figure 5.6: The Hybrid containing four HELIXes, a readout amplifier and a radiation monitor (n-side) or a temperature sensor (p-side). Also visible are the charge sharing capacitor array and the ceramic fan out.

The kapton foil of the hybrids extends to a flexible lead of about 20 cm length, at whose end a female 25-pin Sub-D connector made from ceramics is mounted. This connector is plugged to the vacuum feed-through connectors at the service chamber, which transfer the signals from inside the beam vacuum to the outside world. Due to the extreme thinness of the strip lines this flex-lead is extremely sensitive to mechanical stress and had to be handled with extreme care.

As it is necessary to not only detect the position but also the energy of the particles passing the detector over a wide energy range a charge splitting read out has been devised [R+04]. The input pads of the HELIXes are connected to a ceramic pitch adapter, which then connects to the capacitor array used to distribute the charge into a high gain and a low gain channel: each silicon sensor strip is connected directly to one HELIX read out chip (*high gain*) and via a 10 nF capacitor to a second HELIX

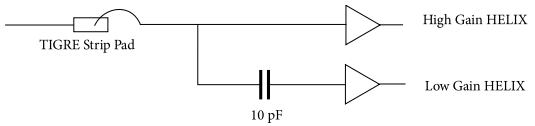

Figure 5.7: Scheme of the charge division read out.

chip (*low gain*), cf. Figure 5.7. This split up allows to read out energy depositions over a large dynamic range from Minimum Ionising Particles (MIPs) to protons stopped in the silicon. The high gain chip is able to read out energy depositions from 1 MIP equivalent up to 10 MIP equivalents, the low gain chip extends the read out range up to 70 MIP equivalents. The dynamic range of one chip alone would not allow a read out of a large signal range like this. There is also no other read-out chip available to measure signals over this wide range; with a dynamic range of over 1:70 the HERMES Silicon Recoil Detector is quite unique in high energy physics.

6 Intermezzo: Silicon Detectors

> ❝God is not interested in technology. He knows nothing of the potential of the micro-chip or the silicon revolution. He's obsessed with making the grass grow and getting rainbows right. . . ❞
> *Evil Genius (David Warner) in the movie Time Bandits (1981)*

First devised in the early 1950ies [McK51] semiconductor radiation detectors are now widely used in high energy and nuclear physics and are also successfully applied in medical and industrial applications. With the introduction of standard processes used in the manufacture of electronic devices to the fabrication of semiconductor radiation detectors [Kem80], they turned into a highly versatile and precise detector technology, featuring high spatial as well as high energy resolution. Semiconductor detectors can have thicknesses ranging from a few 100 µm (used e.g. for vertex detectors which require a minimum of material) to a few mm (as particle stopping detectors in nuclear physics) while featuring areas from a few cm^2 up to a few 100 cm^2 (single sensors like the TIGRE sensor used in the Recoil Detector) resp. hundreds of square metres (combined area of multiple sensors, eg. [CMS06]).

This chapter will give a short overview on the properties of silicon detectors and their read-out. For a more detailed treatment the reader is referred to Ref. [Pei92] and [Lut99].

6.1 General Principle

When an ionising particle passes a semiconductor medium, it looses some energy by producing electron-hole pairs inside the medium. If no outside potential is applied, these pairs recombine shortly afterwards. Applying a voltage along the semiconductor it is possible to separate the pairs and in principle to detect a current produced by them. As in pure semiconductors the intrinsical charge carrier density n_i is orders of magnitude higher than the amount of generated charge carriers this

is mostly not feasible. To successfully detect the created electron hole pairs it is necessary to create a zone depleted from free charge carriers.

The basic structure of a semiconductor radiation detector is a reversely biased p-n-junction. At the junction a depletion zone is formed whose width is given by the sum of

$$W_{\mathrm{p}} = \sqrt{\frac{2\epsilon V_B}{eN_a\left(1 + N_a/N_d\right)}} \qquad \text{and} \tag{6.1}$$

$$W_{\mathrm{n}} = \sqrt{\frac{2\epsilon V_B}{eN_d\left(1 + N_d/N_a\right)}}, \tag{6.2}$$

where W_{p} is the extension into the p-side and W_{n} the extension into the n-side; ϵ is the dielectric constant, V_B the applied bias voltage and e the electron charge, $N_{a,d}$ the number densities of doped impurities (donors and acceptors). The depletion zones extend to the two sides of the junction inversely proportional to the number of dopants N_d and N_a. Using a highly doped p-side ($\mathrm{p}^+\mathrm{n}$ junction) the depletion region would be very wide on the n-side and only very shallow on the p-side. In this case, the n-side of the junction acts as an active volume for the detector, allowing the creation of electron-hole pairs, while the p-side only is used to deplete free carriers and can therefore be very shallow.

Although the depletion region is free of majority charge carriers, electron-hole pairs are generated thermally. Without an external potential these would recombine, however if a bias voltage is applied they are separated and have little chance to recombine. Under the influence of the external field they give rise to a current, the *leakage* or *dark current*. This current consists of two parts: one generated by electron-hole pairs appearing inside the depletion zone which is proportional to the width of the depletion zone (and therefore to $\sqrt{V_B}$) and one which is generated by charge carriers in the neutral region outside the depleted zone, which depends only on material parameters. To decouple the read-out electronics from this dark current, a coupling capacitor between the electronics and the sensor is used.

As there is a voltage dependent charge associated with the depletion zone, a junction capacitance can be defined by

$$C_j = \frac{dQ}{dV_B} = \sqrt{\frac{e\epsilon N_a N_d}{2\left(N_a + N_d\right)V_B}}. \tag{6.3}$$

Assuming $N_a \gg N_d \gg n_i$ this can be expressed in terms of the material resistivity ρ and the majority carrier mobility μ as

$$C_j = \sqrt{\frac{\epsilon}{2\mu\rho V_B}}. \tag{6.4}$$

This junction capacity decreases with increasing bias voltage until the sensor is fully depleted. Together with the coupling capacity it determines the noise properties of the read-out amplifier, as shown in section 6.3.1 on the following page.

In order to obtain position information from the silicon sensor it is necessary to segment it in small divisions. Two different approaches are feasible. First the detector can be segmented into small pads or pixels. The connection to the read-out electronics proves difficult, a common approach is to couple a highly integrated read-out chip by bump bonding to the back side of the detector or to use a hybrid device which already includes the read-out electronics in a single piece of silicon. Pixel detectors are a quite recent development but are already widely used in applications which require precise position detection, from particle physics [ATLAS] to medical applications [Pfe04].

The second and so far the most used approach is to segment the detector into an array of parallel narrow strips. One sided detector designs are relatively easy to manufacture by embedding p-doped strips into n-type silicon. Strip widths down to 20 µm can be achieved. A two sided sensor is a bit more complicated as the n^+-strips on the n-side need to be electrically separated from each other. This can be achieved by implanting blocking p^+-electrodes (*p-stops*) between the n^+-doped strips.

6.2 Readout Process

Semiconductor detectors feature a very high integration density providing a plethora of readout channels on very small space. They are quite often used in areas where the space is extremely limited, e.g. as vertex detectors. As it is not possible to read-out each channel by an own ADC, front-end chips directly connected to the sensors serialise (and in some cases digitise) the signals. The detector signals are fed through a pre-amplifier, the signal is then stored in a buffer and transferred via a multiplexer to an ADC. The chips also feature control registers and supply electronics. These read-out chips are specially designed for the application they will be used for, as parameters like dynamic range and sampling frequency need to fit the requirements

of the experiment (these special designs are often referred to as Application Specific Integrated Circuit (ASIC)). An overview of the chip used for the Recoil Silicon Detector is given in section 5.2.2. An overview of common read-out chips used in high energy physics so far can be found in [FR00].

6.3 Noise

Special care has to be taken on the noise in a semiconductor detector. As the signals are quite low (a Minimum Ionising Particle (MIP) passing through 300 µm of silicon produces around $2.2 \cdot 10^4$ electron-hole pairs [Group02]) and there is no intrinsic charge multiplication, the noise in the amplification system and in the detector can be quite prominent. The electronics noise consists of a constant part, particular for the design, and a part which depends on the detector parameters, mainly the capacitance of the strip being read out to its neighbours and to the back side of the detector. The following sections will give a short overview adapted to the situation for the recoil silicon detector. A more detailed treatment for the successor of the HELIX chip, the Beetle chip, can be found in [KS05].

6.3.1 Amplifier Noise

The front end of the HELIX 3.0 read-out chip is a charge sensitive amplifier consisting of an inverting amplifying circuit coupled to a feedback capacitor (C_f). A switch in the feedback loop (or a high-ohmic resistor) is needed to bring the circuit into operating condition. A schematic can be found in figure 6.1(a). In the ideal case the amplifier delivers an output voltage proportional to the input voltage ($U_{out} = -AU_{in}$). The detector presents a capacitive load C_D to the amplifier, additionally the amplifier has a capacitive load to ground C_i, which is usually dominated by the gate capacitance of the input transistor.

Applying an input charge Q_{in} will result in an output voltage change of

$$U_{out} = -\frac{Q_{in}}{C_f + \frac{C_D + C_i + C_f}{A}}. \tag{6.5}$$

For large amplification this can be approximated by $U_{out} = -Q_{in}/C_f$, assuming that the charge has been completely transferred from the detector to the feedback capacitor. In the low frequency range the input impedance of the amplifier can be

represented by a capacitance $C_{eff} = (A+1)C_f + C_i$. To ensure a complete transfer of the generated charge from the detector to the read out electronics a high value of C_{eff}, i.e. a low input impedance, should be chosen.

To describe the noise properties of the amplifier, a single voltage source U_n connected to the input of the amplifier is modelled, representing the effects of all sources transferred to the input. The presence of this voltage will result in an output voltage even if no signal input is present. This voltage source represents the so called *serial noise* (Figure 6.1(b)). To calculate the corresponding noise charge it is easiest to consider the charge necessary to get a zero output voltage. One then finds

$$-Q_n = U_n(C_D + C_{in} + C_f). \tag{6.6}$$

From this formula it is easily seen that the noise in a good approximation is given by $Q_n = a + b \cdot C_D$, where C_D is the capacitive load at the input and a and b are constants typical for the amplifier [Lut91].

As a realistic detector is not represented by a simple capacitor an additional noise source is needed to describe the detector. The biased detector will draw some leakage current I, which has statistical fluctuations due to the discrete nature of the charge carrier. This is called shot noise and has first been described in [Sch18]. The variations are approximated by a Gaussian distribution and are independent of the frequency f. The spectral power density of the variance is given by

$$\frac{d\langle I^2\rangle}{df} = 2Ie. \tag{6.7}$$

Additionally thermal and low frequency noise have to be considered. Thermal noise is caused by the thermal fluctuations of the electron distribution in a conductor. It is also referred to as Johnson-Nyquist noise, first described in [Joh28]. Voltages and currents generated by thermal fluctuations of the charge carriers velocities are independent of the frequency. In case of a physical resistor, thermal noise can be described as a current source I_n parallel to the resistor with a spectral power density of

$$\frac{d\langle I_n^2\rangle}{df} = \frac{4kT}{R}. \tag{6.8}$$

Shot noise and thermal noise are modelled as a current source parallel to the detector capacitance and referred to as *parallel noise*.

Additional low frequency noise is present in most electronic devices. The source of this noise is not unique and shows different mechanisms for different electronic devices. The power spectrum of this noise has an approximate $1/f$ dependency. It is also referred to as flicker noise.

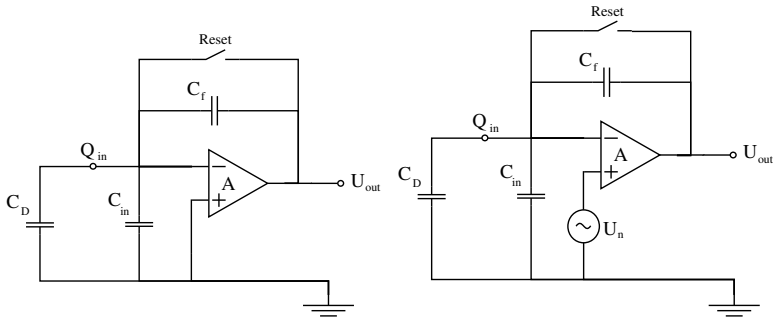

(a) An ideal amplifier (b) An amplifier with serial noise

Figure 6.1: Principle of a charge sensitive amplifier.

The shot noise originating from the bias currents evaluates numerically to

$$\frac{d\langle I^2\rangle}{df} \Big/ \frac{[\mathrm{nA}]^2}{[\mathrm{Hz}]} = 2Ie \approx 0.32 I_{\mathrm{bias}} / [\mathrm{nA}] \tag{6.9}$$

and the thermal noise due to resistors parallel to the detector capacity C_D or the feedback capacity C_f to

$$\frac{d\langle I_\mathrm{n}^2\rangle}{df} \Big/ \frac{[\mathrm{nA}]^2}{[\mathrm{Hz}]} = \frac{4kT}{R} \approx \frac{1.6 \times 10^{-8}}{R_{\mathrm{bias}} / [\mathrm{M\Omega}]}. \tag{6.10}$$

Typical bias currents observed for the Recoil Detector modules are in the order of 2 µA for sensors without radiation damage. The TIGRE sensors are biased via poly-silicon bias resistors of 6.5 MΩ, the feedback resistor parallel to C_f of the HELIX is also in the order of MΩ. Thermal noise from the bias resistor and the feedback resistor can be neglected safely therefore.

In addition to the shot noise of the bias current, also noise originating from the biasing circuitry has to be added to the parallel noise (represented by a current source $i_{\mathrm{n,bias}}$ in the biasing circuit). As the detectors are shielded from the detector current by capacitive coupling, the equivalent noise charge is given by the integral over time of the current fluctuations folded with a weighting function describing the filtering of the connected read-out circuit.

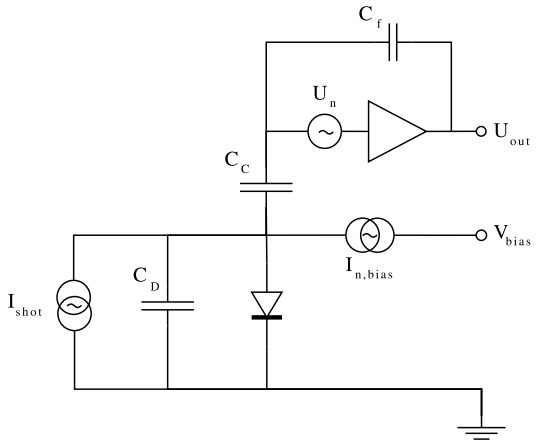

Figure 6.2: Equivalent circuit diagram for a capacitively coupled detector connected to a charge sensitive amplifier. The detector is represented by a reversely biased diode in parallel with a capacitor and a shot noise current source.

Figure 6.2 shows an equivalent circuit of a capacitively coupled detector. The noise is modelled by a serial noise voltage U_n, representing noise sources within the amplifier, the shot noise of the detector leakage current I_{shot} and the noise current of the biasing circuit $I_{\mathrm{n,bias}}$. The serial noise generated in the amplifier produces an output signal dependent on the detector capacitance, while the signal of the parallel noise sources I_{shot} and $I_{\mathrm{n,bias}}$ is the time integral of the current flowing into the amplifier. While the detector leakage current is essentially shot noise, thus showing a white noise spectrum, both the serial amplifier noise and the bias current noise can

have a noticeable low-frequency component which can be assumed to have an $1/f$ power density spectrum. The amplifier noise is mostly generated at the input stage of the read out chip. All subsequent stages generate also noise, however due to the amplification the signal becomes larger and the noise to signal ratio N/S smaller.

A full analysis of the dependence of the noise on the signal shaping time is cumbersome and not possible without knowing the internals of the read out chip, but it is possible to show the following proportionalities on the filtering time constant τ for the ratio of noise N over signal S [Lut99]:

$$N/S_{\text{white, serial}} \propto \frac{1}{\sqrt{\tau}}, \tag{6.11a}$$

$$N/S_{1/f\text{, serial}} \propto 1, \tag{6.11b}$$

$$N/S_{\text{white, parallel}} \propto \sqrt{\tau}, \tag{6.11c}$$

$$N/S_{1/f\text{, parallel}} \propto \tau. \tag{6.11d}$$

Shot noise of the leakage current and noise generated by the bias circuits affect all strips of the detector simultaneously. In the ideal case of all detector strips having the same electrical properties this leads to noise of the same strength in all channels which can be interpreted as a pedestal shift called Common Mode Noise (in the cited literature also found as correlated or coherent noise). This noise can be easily corrected, at least in theory. As only a few strips of the detector get a signal for a physics event, the non-hit channels can be used to calculate the amount of common mode noise by averaging over their pedestal subtracted value.

A complete model of the noise is difficult to achieve, as the equivalent network soon gets complicated. A circuit diagram of the TIGRE sensor and the connected HELIX front end chips can be seen in Figure 6.3, not shown is the charge splitting into a high and a low gain path, which introduces additional capacitances.

6.3.2 Signal modelling and corrections

The signal Q_i^k measured by a strip k in an event m can be described by the following model:

$$Q_m^k = S_m^k + P^k + N_m^k + C_m, \tag{6.12}$$

with S_m^k being the actual signal generated by the passing particle, P^k the pedestal of strip k, N_m^k the individual uncorrelated noise of each strip and C_m the common

mode noise for the event i. Crosstalk and charge sharing between neighbouring strips are included in the strip signal S_m^k and are not corrected for in this model. The pedestal is assumed to be of a constant value and therefore can be determined in special pedestal runs by averaging over all M events without physics signals present:

$$P^k = \frac{1}{M} \sum_{m=1}^{M} Q_m^k. \tag{6.13}$$

In the case of a symmetric distribution of the noise this leads to the actual pedestal value; if the noise is asymmetric (emphasising higher or lower values) the calculated pedestal will not be the real pedestal, but a slightly higher or lower value. These differences will mostly be corrected when subtracting the common-mode noise.

The common mode noise can be calculated from the K channels not hit as an average over these channels. For the HERMES Recoil Detector, the first 16 not hit channels out of the first 32 channels will be used for this:

$$C_m = \frac{1}{K} \sum_{k=1}^{K} (Q_m^k - P^k). \tag{6.14}$$

This assumes the common mode to be the same for each strip, which is the case if they are electrically identical. In the following a more general approach is shown.

The uncorrelated noise cannot be corrected for, but an estimate of its strength can be given from the average deviation of the measured values of events without physics signals from the calculated pedestals:

$$\left\langle N^k \right\rangle = \sqrt{\frac{1}{M} \sum_{m=1}^{M} (Q_m^k - C_m - P^k)^2}. \tag{6.15}$$

The simple common mode noise model fails if the individual strips are not electrically identical, resulting in a common mode of varying strength for each strip. The silicon modules for the HERMES Recoil Detector are read out via flexfoils with different trace lengths for each strip which result in slightly different capacitances and resistances. A different strength of the common mode for each strip can be measured. In a first approach, it is assumed that each strip has a weighting factor w^k which could depend on the common mode strength. The signal model gets then extended to

$$Q_m^k = P^k + S_m^k + N_m^k + w^k(C_m) C_m. \tag{6.16}$$

The weighting factors w^k can be calculated from pedestal runs by

$$w^k(C_m) = \frac{Q_m^k - P^k}{C_m}. \tag{6.17}$$

A more general approach taking into account also nonlinear dependencies of the weighting factor from the common mode can be easily constructed. The weighting factor has to be substituted then by a polynomial or other function of C_m and can be obtained from a fit to the distribution of the residual versus the common mode calculated by equation 6.14.

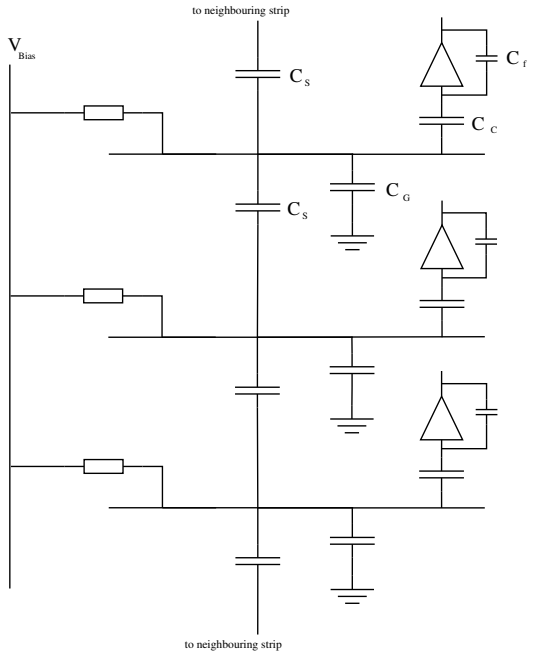

Figure 6.3: Circuit diagram of the TIGRE sensor and the connected HELIX front-ends.

7 Monte Carlo Simulations

> "I had a continual restless feeling that there was nothing at all real about Monte Carlo; that the sea was to blue to be wet, the casino to white to be anything but pasteboard, and that from their very greenness the palms must be cotton."
> *Willa Cather – Willa Cather in Europe, Ch. 14.*

Monte Carlo simulations are a valuable tool in physics to study the physics processes as well as the detector responses. As often it is not possible to create an analytical model for the physics process as well as the complex detector system, a statistical model is made. A sample of products of a physical reaction is generated, these are then tracked through a model of the detector system and the response function of the detectors is simulated. This statistical sample can then be compared to real data. This chapter will give a brief overview of the Hermes Monte-Carlo chain and a description of the Recoil Silicon Detector simulation.

7.1 The HERMES Monte Carlo

The Hermes Monte Carlo (HMC) chain is based on the GEANT Monte Carlo framework (Version 3) provided by the CERN Software Library. It is basically split into three parts, first a generator creating the reaction products of a physical reaction like Deep-Inelastic Scattering; second a tracing stage, which proceeds the reaction particles through the detector and takes care of processes like bremsstrahlung or generation of secondary particles inside material the particles pass, as well as calculating the energy deposition in a detector; and third a digitisation stage which simulates the electrical response of the detectors to the energy deposition of the passing particles. The output of HMC is in a format readable by the Hermes reconstruction program and can therefore be processed with the full analysis chain also used for physics data.

Various generators (inside the GMC wrapper) exist for the different physics processes, amongst others one for Deep-Inelastic Scattering. It generates events

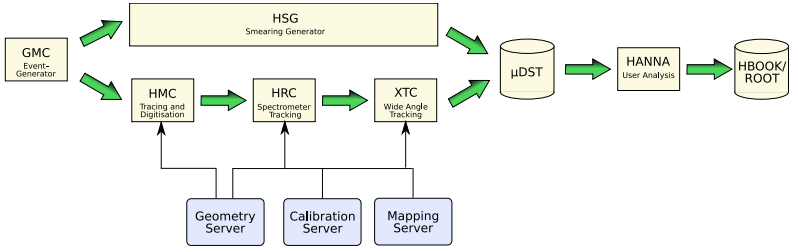

Figure 7.1: The HERMES Monte Carlo chain. The data generated by GMC can either be passed through HMC for a complete detector simulation or through the smearing generator HSG for a statistical detector model.

with random Q^2 and ν according to the DIS cross-section and produces a random azimuthal angle ϕ. A routine based on the Lund model [AGS83, And98] produces then the outgoing hadrons at the vertex for this event, based on models of Parton Distribution Functions. The scattered lepton and the secondary hadrons are then handed over to the tracking stack.

The tracing stage is included inside HMC. It contains a model of the HERMES detector including the support structures and inactive detector material. This model is stored inside a geometry server, which also is used for the HERMES reconstruction program. For each particle the path through the detector is simulated taking into account the interaction cross sections for the material it traverses as well as the cross sections for bremsstrahlung and similar processes. When the particle crosses an active detector volume, the energy deposition is recorded.

Digitisation also happens inside HMC. After the tracing the detector response for each hit is simulated. The signal according to the recorded energy deposition is calculated, an additional noise simulation is added. Fake hits due to electrical noise can also be generated. Depending on the detector type simulated the digitisation takes into account detector and read-out electronics saturation as well as various noise sources. The output of HMC is then passed through the HERMES reconstruction program, using the same routines as for the data of the actual detectors. It produces therefore similar output as the actual detector responses recorded at the experiment, plus the Monte Carlo information such as particle type and the originally generated

kinematics.

The amount of effects simulated in the tracing and digitisation stage can turn out to be computational expensive. The complete tracing and digitisation of 100 000 events for the HERMES spectrometer only (Recoil Detector not included) takes about 24 hours. To reduce this time a smearing generator was implemented, which simulates kinematical effects and smearing of the detector on a statistical basis [Hilo5]. Using this smearing generator the simulation of 100 000 events is reduced to about 15 minutes.

7.2 Silicon digitisation

The modelling of the silicon detector is based on the signal model shown in section 6.3.2. It is done on three levels: first the space-points describing hits are converted into detector strip information, second a loop over single hits is done to take care of electronics and detector noise added to the actual hits, then a third phase adds up multiple hits in a single strip and produces additional hits due to noise. According to the usual HERMES MC scheme, three different routines including different levels of sophistication can be chosen to digitise the hits, the most advanced version is yet to be finalised, the differences can be seen in table 7.1 on the next page.

The conversion from space points to strip coordinates is described in [Sheo4]. The coordinates given by the Monte Carlo are the entry coordinate, where the particle enters the detector, and the center coordinate, where the particle passes the center plane of the detector. From these the exit coordinate is calculated and the hit strips are determined. If more than one strip is hit, the energy deposition is split accordingly.

In the next step all hits are then converted from energy deposition to ADC values. This conversion is done using averaged calibration factors determined from the Erlangen Tandem Test. As there are different modules involved in processing the signal, each of these modules needs to get calibrated independently. Therefore the conversion from the deposited energy $E^k_{\mathrm{dep},i}$ to the digitised signal $\mathfrak{S}^k_i$ uses multiple calibration parameters:

$$\mathfrak{S}^k_{i,L} = \underbrace{E^k_{\mathrm{dep},i} \cdot g_{\mathrm{Si},L}}_{U^k_{\mathrm{ACC},i}} \cdot g_{\mathrm{ACC}} \cdot c_{\mathrm{HADC}}, \tag{7.1}$$

$$\mathfrak{S}^k_{i,H} = \mathfrak{S}^k_{i,L} \cdot h. \tag{7.2}$$

Mode	Features
`NONE`	• energy to ADC conversion • saturation as cutoff • no noise, crosstalk, CMN
`FAST/REAL`	all from `NONE` plus • gaussian noise added to hits • crosstalk with averaged values • noise hits • dead strips • charge sharing between strips • CMN with various models • hit threshold
`EXPERT`	all from `REAL` plus • individual parameters for each strip • possible non-linearities • sensor dependent saturation

Table 7.1: The different digitisation modes for the Silicon Detector available in the Monte Carlo.

The digitisation routine uses the same factors for all strips, as the strip to strip variations are small. Here $g_{\mathrm{Si},x}$ is the response of the detector to an energy deposition $E^k_{\mathrm{dep},i}$; g_{ACC} is the amplification factor of the ACC line driver module and c_{HADC} is the conversion factor from voltage to ADC channels of the HADC. The high gain value is calculated from the low gain value using the ratio h between them determined in the test beam. This calibration model is the same as in the data analysis chain, except for the averaged calibration factors. In the data analysis chain variation between the different strips are also taken into account, thus resulting in specific calibration factors $g^k_{\mathrm{Si},x}$ and h^k for each strip. Saturation of the read out chips is modeled as a simple cut off at a certain value determined in the experiment. For each hit additional hits caused by crosstalk to the neighbouring strips are generated.

Following the conversion is the generation of noise and noise hits, which can be tuned to fit the real noise situation or for studies, as well as switched off completely. In the simplest form a Gaussian random noise is added to each hit. For a more realistic simulation, noise hits can be generated using a Poisson distributed number of noise hits and a random Gaussian energy deposition. Low and high gain are treated independently as it is assumed that noise hits are generated in the readout chips or later. The common mode noise can be chosen as a simple shift of all strips of one read out chip or a model which modulates this shift with a Gauss shaped function of the strips with random width and center.

A last treatment is the summing up of different hits. If two particles pass the detector close to each other it can happen that the digitisation produces two hits in the same strip. The last routine in the digitisation process sums up these hits and merges them into one combined hit. If dead strips are to be simulated, the hits in these strips are deleted from the data set. A common threshold is applied to all hits, those below the threshold are deleted.

Figure 7.2 shows the Monte Carlo simulated energy deposition measured at the n-side versus the energy deposition measured at the p-side for cosmic muons passing the detector, for comparison a plot with experimental data from a dedicated cosmics run is also included. The noise has been overestimated to show the effect on the energy deposition. The energy deposition has been normalised for the incident angle. In the experimental data additional effects originating from high common-mode can be seen which are not included in the Monte Carlo simulation, as they were only present at the test experiment.

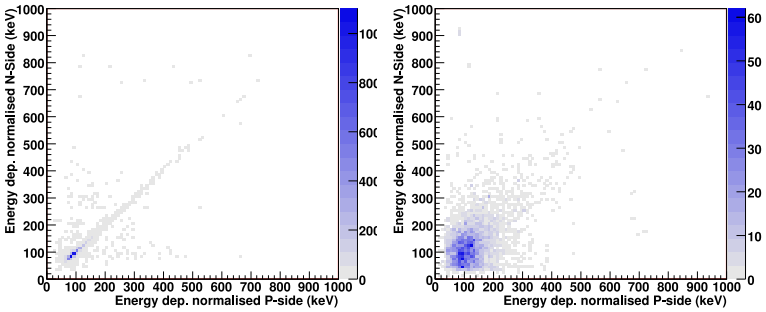

(a) Monte Carlo, without noise simulation

(b) Monte Carlo, with noise simulation (not tuned)

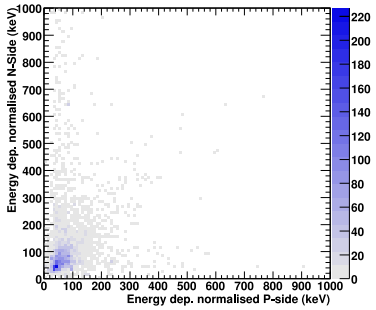

(c) Experimental Data (Test-Experiment, 500.000 events)

Figure 7.2: Energy deposition measured by the n-side versus the energy deposition measured on the p-side for Monte Carlo data without and with noise simulation and for experimental data. All plots are for cosmic ray data.

8 Test Experiment and other Studies

> ❝Rationally let it be said in a whisper,
> experience is certainly worth more than theory❞
> *Amerigo Vespucci – Letter to*
> *Lorenzo di Piero Francesco de' Medici, 1500*

Before the installation, all parts of the Recoil Detector were extensively tested. The silicon prototypes were tested at the Erlangen Tandem facility, at DESY Test-Beam T22 [GHK+04a] and at a test beam at the GSI in Darmstadt. The production modules were tested and calibrated at DESY Test-Beam T22 [HMG+05] and at the Erlangen Tandem [BKP+05]. Directly after manufacturing, all modules were also subject to a LASER-test at DESY Zeuthen [GHK+04b]. A bench test and a test experiment together with the full Recoil Detector completed the testing phase. These last two tests and their conception formed the main part of this thesis, together with the installation and comissioning of the silicon modules.

8.1 Benchtest

From December 2004 to January 2005 the silicon detectors were subject to a bench test. This was the first time eight modules were tested together, so far only basic tests with two modules at the same time had been done. Goals of the bench test were checking the functionality of all detector modules after they have been transported to the east hall, testing all involved electronic modules and testing the detector system as a whole. A long term study to check the running of the detectors over a time span equivalent of two or more fills also was performed.

8.1.1 Setup

Starting from a simple setup, the bench test electronics evolved into a shape close to the final installation. The cabling was chosen to be similar to the test experiment

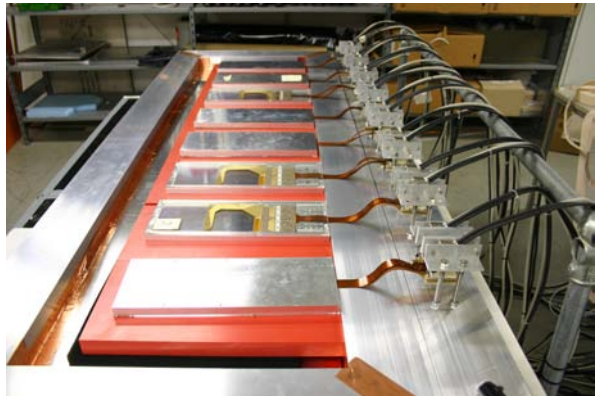

Figure 8.1: Photo of the bench test setup. Eight modules are placed on plastic plates to prevent capacitive coupling to the aluminium plate beneath. During the tests a light tight box was placed on top of the setup.

and the final installation, regarding to length and signal characteristics. The bench test was also used to improve the electronics setup and as a testbed for the software development.

The bench test was done in room 202 in the East Hall. The modules were placed inside a Faraday cage formed by a wire mesh top and an aluminium plate as base. A light tight box surrounded the cage. To insulate the modules from capacitive coupling to the aluminium plate plastic plates were placed in-between the module housings and the base plate. Figure 8.1 shows a photo of the bench with eight modules, the Faraday cage removed.

Up to four HADCs and two HLCUs were used to read out and control the modules. The trigger was generated by down-scaling the 10.4 MHz clock supplied to the modules, the setup was modelled after the laser test stand used at DESY Zeuthen [GHK+04b]. In the later phase a software generated trigger and NIM-electronics setup as in the final experiment were used. The parameters for the HLCUs, HADCs and HELIXes were taken from the Erlangen Calibration setup.

8.1.2 Software

For the test beams at DESY Zeuthen and T22 a LabView based software capable of reading out one HADC was used. As for the final experiment a faster readout software was required, which needed to be consistent with the HERMES read out, it had to be re-written. As a starting point the read-out software used at the Erlangen calibration was used. Some of this software was written in Python and had to be ported to C. All fundamental read out routines could be taken over with only minor modifications.

At the time of writing the following features are implemented:

- read configuration data from files,
- initialise single HADCs and HLCUs individually,
- program single HELIXes and program all HELIXes at one HLCU at the same time (broadcast),
- read out in individual buffer mode (word by word),
- read out in single buffer mode (one block containing all data),
- provide 4 different trigger signals on the output of the SIS3100 controller,
- read-out initialised by internal or external trigger signal,
- works for 1 (for testing) to 16 modules (complete sub-detector).

An automatically generated documentation[1] of the source code can be found in [KMP05]. The software has been integrated into the Recoil Detector control software. It is used also in the HERMES setup to initialise the detector and to take cosmics data.

8.1.3 Noise behaviour

Most of the bench test time was used to optimise and understand the noise performance of the silicon modules. The initial setup of the modules placed onto an aluminium plate proved to be the source of very high common mode noise. Placing insulating material between the modules and the aluminium plate reduced the common mode noise drastically (see figure 8.2 on the next page), while the uncorrelated noise did not change significantly. As a consequence two 5 cm thick plastic pieces were put beneath each of the detector modules, to reduce the capacitive coupling to the aluminium plate.

[1] generated with the doxygen documentation system (http://www.doxygen.org)

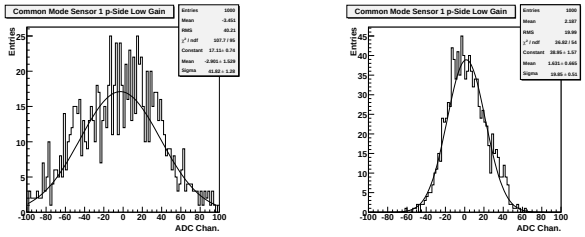

(a) Without distance piece.

(b) With 5 cm thick Styrofoam.

Figure 8.2: Influence of capacitive coupling on the Common mode noise.

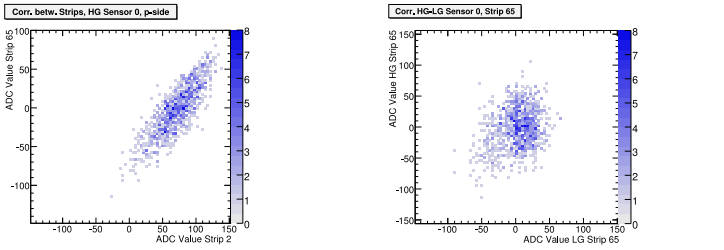

(a) Correlation within one chip.

(b) Correlation High Gain to Low Gain.

Figure 8.3: Correlation of the noise in different strips.

The noise after pedestal correction showed a strong correlation between the strips connected to one HELIX read out chip, however no clear correlation between the high gain and the low gain chip can be seen. In 8.3(a) on the facing page the noise signal of a strip at the center of the detector (strip 65) is plotted against the signal of a strip at the edge of the same sensor (strip 2). The signals are clearly correlated. Figure 8.3(b) shows the signal of the high gain channel of a strip (strip 65) plotted against the low gain signal of the same strip. No correlation is visible. As the separation of the high and low gain signals happens directly before the read out chips, it is an indication that the noise is coupled in directly on the hybrid and not on the flex foils or the sensors; experiences from the test experiment later showed that this assumption might not hold for the final setup.

The grounding was done as foreseen in the final setup, most variations resulted in little or no changes. No difference could be seen between cable shielding connected to ground or floating. However tying the floating power supplies to chassis ground lead to a strong raise of the noise. Placing ferrite cores on the cables introduced no change. The HELIXes proved to be very sensitive to variations in the supply voltages. A small change in the supply voltages resulted in large changes in the common mode noise. This has been observed also in the test-experiment and will be described later on. Varying the timing parameters showed nearly no influence on the noise, as was expected.

8.1.4 Test-pulse

The HELIX 3.0 chip has an integrated circuit which feeds a test-pulse charge into the input amplifiers triggered by a pulse applied to the respective input pad on the chip. This can be used to check the basic functionality of the system starting at the input amplifiers of the HELIX. Via capacitors a charge equivalent to the energy deposition of 1 to 4 MIPs in a 300 µm thick silicon sensor is fed into the input amplifiers by a current source internal to the HELIX; the first strip is fed with a ±1 MIP signal, the second a ±2 MIP, the third a ±3 and the fourth a ±4 MIP signal, the polarity of each changing after each test pulse sent. This pattern repeats over the whole chip. Due to variations on the chip and at the coupling to the sensors, these signals are only roughly the size of 1 – 4 MIP equivalents, with variations up to a factor of two, so that the test-pulse is not usable for calibration purposes. It can only be used to monitor the relative gain of each strip over time.

Due to high common mode present in the test setup, the raw data without common

mode correction shows quite smeared signals with large variations (Figure 8.4 on the next page), and a correction is necessary. Without any common mode present, one would expect a twofold stair like pattern repeating every four strips with signals at ±1, ±2, ±3, ±4 MIP. Due to high noise and a shift in the baseline of the pattern for different polarities of the signal this pattern gets smeared. As all strips get a signal fed in, common mode correction can not be done on the HADC but has to be done offline. A method which proved useful is to look at the 2 – 4 MIP signals relative to the 1 MIP signal for each event, as seen in figure 8.5 on the facing page for all HELIXes of a module. Figure 8.6 shows 21 strips of one HELIX chip in more detail, Panel 8.6(a) without correction, Panel 8.6(b) shows the test pulse signals relative to the 1 MIP signal. For each group of four strips, the ±1 MIP signal of the groups first strip is subtracted for each event. This method removes the baseline-shift seen for the signals of different polarity as well as the effects of the common mode. Still the strip to strip and chip to chip variations in the signal height, which are much larger than the variations seen at the test beams, show that the test pulse signal is not usable for an absolute calibration, but is a valuable tool to check the read out system and the basic functionality of the HELIX chips.

8.2 East Hall Test Experiment

In August 2004 the whole detector was mounted in the East Hall to test the overall system integration and to do first detector studies of the complete detector with cosmic rays. This was also a test for the mounting procedures, for the tools developed to handle the detectors and for the supporting structures. The superconducting magnet was commissioned and experience gained in filling and running the magnet. During the test experiment the readout and control software evolved into a first version usable at the final experiment. Slow Control and integration into the HERMES DAQ were tested.

8.2.1 Setup

The test experiment was constructed in an area of the East Hall still outside the concrete block shielding of the experimental area. All dimensions were chosen to correspond as closely as possible to the final mounting in the experiment. As a support structure two non-magnetic steel plates were fixed to the floor of the

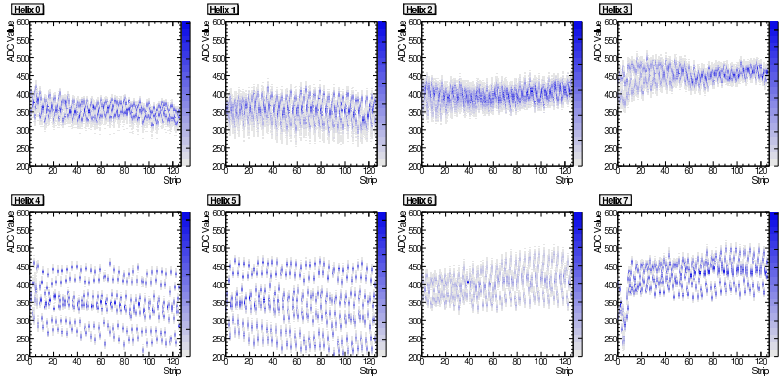

Figure 8.4: The test pulse signals with no signal corrections for all helixes of a single module (Homer): top half are the low gain chips, bottom half the high gain, the left two plots are p-side each, the right two n-side.

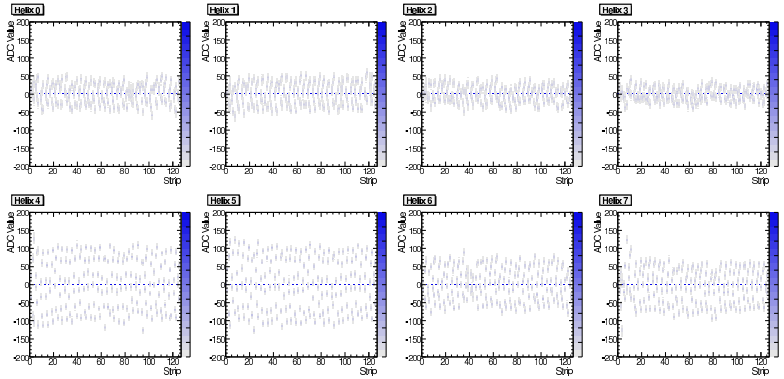

Figure 8.5: The test pulse signals relative to the one MIP signal for all helixes of a single module (Homer): top half are the low gain chips, bottom half the high gain, the left two plots are p-side each, the right two n-side.

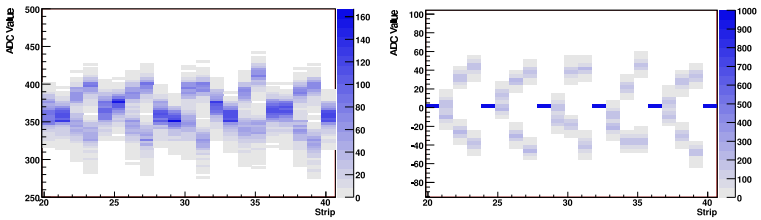

(a) No signal correction (b) Relative to the one MIP signal

Figure 8.6: The test pulse signals with no signal corrections for 21 strips of a single HELIX chip (HELIX 1).

experimental hall. On one of these plates the detector setup was mounted, on the other a platform for the mounting of the electronics racks which would go into the experiment was fixed. The electronics racks were separated into the ones to go inside the experimental area and the racks to be placed into the electronics trailer. The grounding of all electronics was floating with respect to the detector support, the ground connection was done via the electronics trailer. An independent readout via a dedicated computer was used during testing and cosmics data taking. To check the integration into the HERMES DAQ a connection to the HERMES read out crates in the electronics trailer and to the HERMES trigger was made.

The superconducting magnet was connected to a 500 l liquid helium dewar, which needed to be exchanged after only about 4 hours of magnet running. As an exchange of the dewar lead to a heat up of the superconducting coils above the critical point no continuous operation was possible, only short tests of the operation with full magnetic field strength were done. A detailed description of the commissioning and the modifications to the original design can be found in [Sta06]. After the modifications the magnet was commissioned successfully. It could be shown that the sub-detectors work without disturbance in the full magnetic field of 1 T strength.

For noise studies pedestal runs were taken using a software generated trigger. Data for cosmic muons were taken with a trigger formed by a coincidence between the upper and the lower half of the parallel layer of the photon detector. In total 1527 runs were taken with the cosmics trigger, of which around 400 lasted around three

hours and are usable for analysis. Around 5000 runs were taken using the pedestal trigger and were used for various noise studies and to test the hard- and software.

8.2.2 Results

As already observed in the bench test, the silicon modules suffered from quite high Common Mode Noise. Figure 8.7 shows the raw spectrum of one sensor. The strips 85, 86 and 96 of this sensor are broken and show no signals. An online cut of 60 ADC channels was applied. The Common Mode Noise strength rises with the strip number, in addition the first few channels also show high noise. This has been observed for most sensors. The band stretching between 300 and 600 ADC channels belongs to events with very high Common Mode Noise, where the HADC's online Common Mode correction fails. The HADC calculates the common mode from the first 16 strips below a threshold (*high threshold* set in the HADC configuration register) out of the first 32 strips. If less then 16 strips within the first 32 are below the threshold, the common mode calculation fails and a wrong value is subtracted. If all 32 are above threshold, the online correction is not done, the HADC reports a Common Mode of zero. This data should therefore be discarded.

Changes in the grounding scheme only resulted in little changes of the Common Mode Noise. The HELIX supply voltages showed some influence on the strength of the Common Mode, although the strongest changes were observed at the edge of the specified working region of the supply voltages. Figure 8.8 shows the value of the Common Mode averaged over all high resp. low gain chips of a module as a function of the HELIX supply voltages V_{DD} (negative) and V_{SS} (positive). A general decline in the common mode strength for more positive values of V_{DD} and V_{SS} can be seen. As these changes were slightly different for each chip an individual tuning of these voltages proved to be necessary. At voltages close to the maximum resp. minimum allowed values, the noise changes quite strongly, as the HELIX is not operating stable anymore.

The strength of the Common Mode Noise is different for each strip, the correlation between the strips is getting lower for greater distances between the strips. Figure 8.9(a) shows the noise signal of a strip close to the center of the sensor versus the calculated common mode (the average of the signal of all strips). No physics signal is present. Using the assumption that the Common Mode Noise has the same strength on each strip this dependency should show a slope of 1: the Common Mode Noise should be the average noise signal of all strips, influencing all strips equally. As

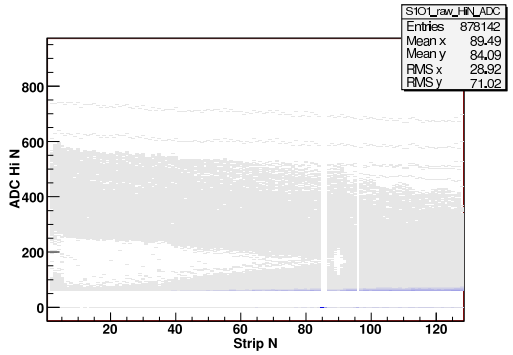

Figure 8.7: Pedestal subtracted data spectrum of one Sensor (S1O1). The very high common mode is clearly visible as the band stretching between 300 and 600 ADC channels.

can be seen from Figure 8.9(b), the slope descends with the strip number, which needs to be taken into account when correcting for the Common Mode Noise. At higher Common Mode values also a deviation from linearity can be seen, which can be taken care of by using a fit polynomial of higher order to parametrise the dependency.

In order to apply a correction for this dependency to the data off-line, the Common Mode needs to be calculated reliably. Events which have a very high Common Mode, leading to a wrong online correction, can therefore not be corrected offline and should be discarded. In the case of unsparsified data and no online Common Mode correction, an offline correction can be done.

Figure 8.10 shows the noise reduction using weighted common mode: shown is the width of the pedestal after noise reduction using a common mode subtraction as implemented in the HADC (black circles) and using two methods using weighted common mode. Model 1 is using a linear dependence of the noise to the common mode (red squares) as described above, Model 2 is using a quadratic dependence (blue triangles). These data are based on pedestal runs. The difference between using only linear correction factors or assuming a quadratic dependence is negligible. The noise can be reduced to a pedestal width of about five to seven ADC channels

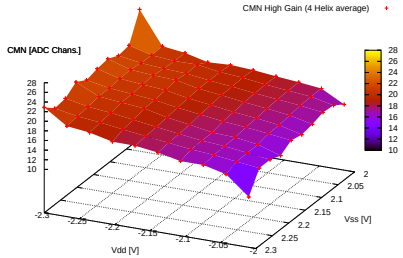

(a) High Gain.

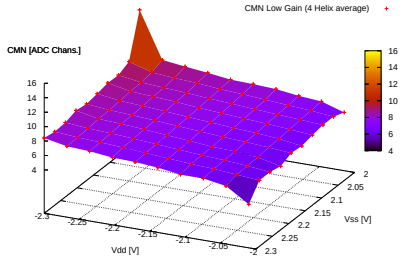

(b) Low Gain.

Figure 8.8: Dependence of the Common Mode Noise on the HELIX supply voltages.

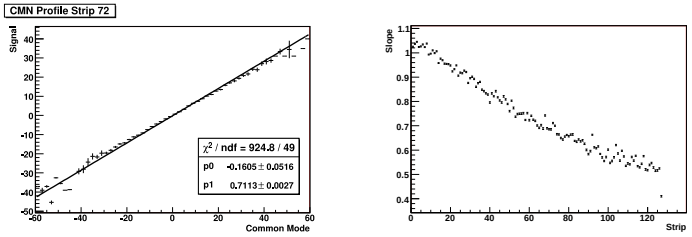

(a) Noise Signal of a single strip versus Common Mode for a pedestal run.

(b) The slope of the fit to Noise Signal versus Common Mode for all Strips.

Figure 8.9: Dependance of the noise signal in a strip on the Common Mode Noise and on the strip position.

(corresponding to about 30 to 40 keV uncertainty in energy deposition).

Figure 8.11 shows the reduction of hits above threshold for a sparsified run using the different methods for Common Mode Noise correction, Figure 8.11(a) using the slopes determined in a pedestal run directly before the run to be corrected, Figure 8.11(b) using the slopes determined from a pedestal run three days before. Again the difference between a quadratic or a linear fit to determine the slope of Noise Signal to Common Mode strength is negligible. The number of noise hits in the first 20 strips is practically zero for all methods, as these strips are used for the Common Mode estimation. As the correlation decreases with rising strip number, the noise and the number of noise hits increases with the strip number. A weighted Common Mode correction reduces the noise hits quite well.

In studies done after the test experiment was finished it was found that the common mode was mostly caused by an interference between the different modules. A minor modification in the electrical setup of the modules removed this interference and only a very low common mode was seen afterwards. Figure 8.12 shows the three weighted common mode corrections applied to data taken after the modification. Little effect on the data can be seen, the pedestal width is already before correction below three to four ADC channels, thus at the level observed in the test beams before.

Even though the noise in the test experiment was much above the expected value it still was possible to detect cosmic muons with the silicon detector. Figure 8.13

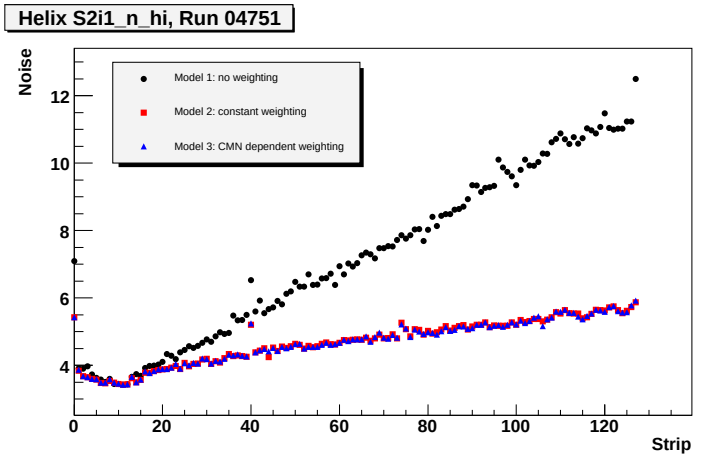

(a) Sensor 2, n side.

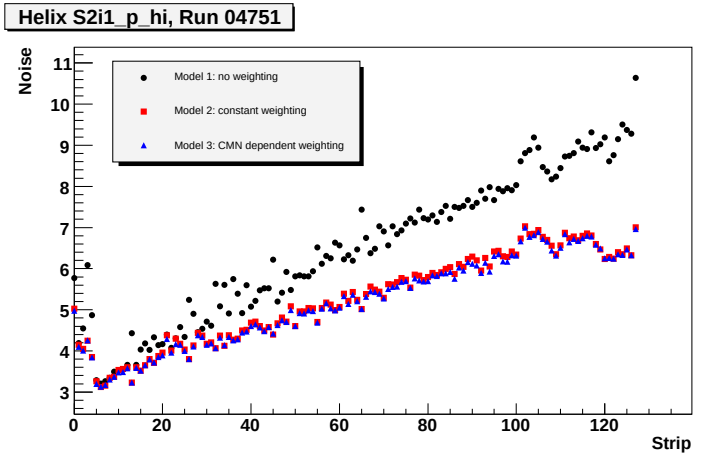

(b) Sensor 2, p side.

Figure 8.10: The effect of different methods to correct for Common Mode Noise.

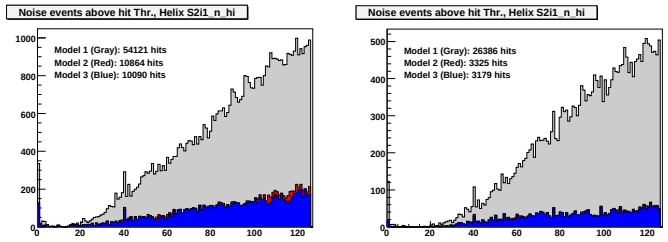

(a) Pedestal run from directly before. (b) Pedestal run from three days before.

Figure 8.11: Reduction of the number of hits above threshold with different Common Mode subtraction methods.

shows the incidence angles of cosmic muons reconstructed with the Scintillating Fibre detector (spherical coordinates, y-axis is upwards). The trigger was provided by a coincidence between the whole upper and the whole lower halves of the Photon Detector. For track reconstruction a hit in the outer and the inner SciFi detector were connected by a straight line. The position of the intersection with the xz-plane is shown in Figure 8.14. The majority of the tracks is located to the outer edges of the covered area. Due to the barrel shape of the SciFi detector the probability for having two hits in the SciFi is larger at the edges as more fibres can be hit by particles coming mostly from above. More hits are found at negative x-values, this is consistent with the asymmetry found in the angular distribution in ϕ shown in Figure 8.13, which is an indication of a slight misalignment. The alignment of the detectors is not included.

The tracking routine in the HERMES extended tracking program XTC calculates the intersection of the track with the silicon detectors. Figure 8.15 shows the position of reconstructed hits against the position of the calculated intersection of the track with the silicon detectors. A clear correlation can be seen, the smearing in position is around two to three strips.

In order to detect the hits, the timing of the HELIX needs to be adjusted correctly. The HELIX features a storage pipeline with a depth of 128 events, of which only one is read out. This is determined by the *latency* set in the HELIX and HLCU

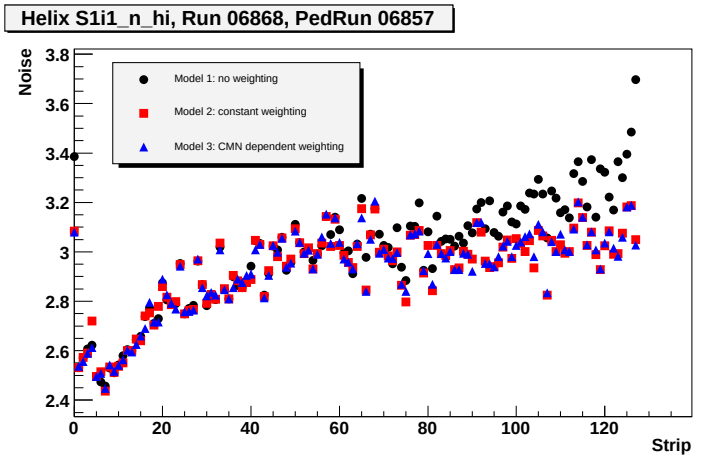

(a) n side

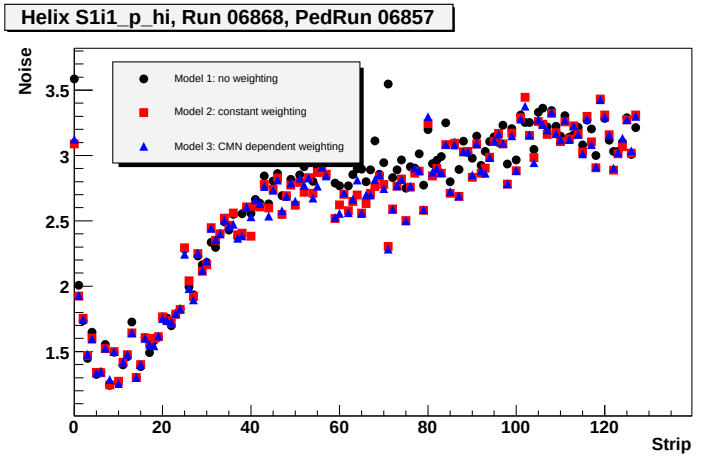

(b) p side

Figure 8.12: The different methods to correct for Common Mode Noise for a run with low Common Mode.

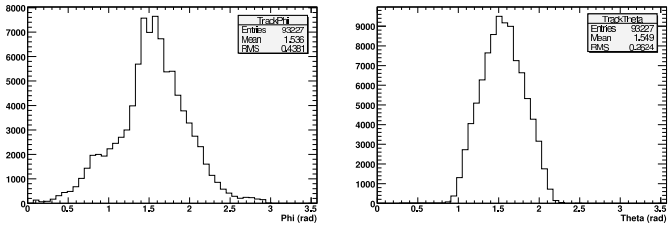

(a) Azimuthal angle φ (b) Polar angle ϑ

Figure 8.13: Incidence angle of the cosmics track reconstructed with the SciFi detector. The y-axis of the HERMES coordinate system points upwards and corresponds to $\varphi = \vartheta = \pi/2$.

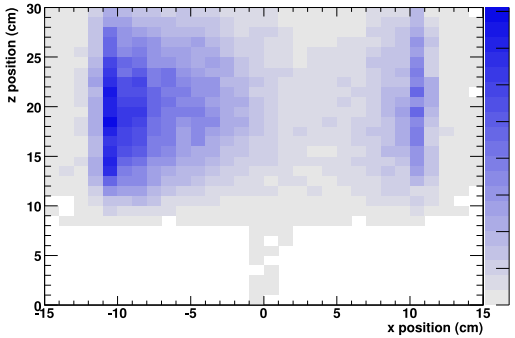

Figure 8.14: Position of the intersection of the reconstructed track with the xz-plane.

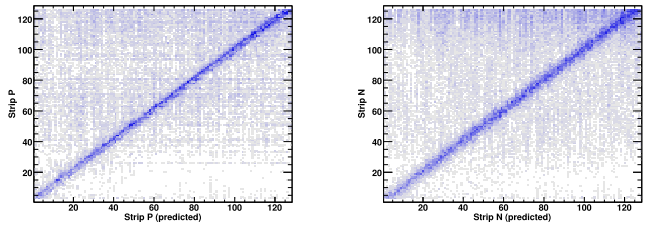

(a) p side (b) n side

Figure 8.15: Hit strip versus prediction by XTC.

configuration, as explained in section 5.2.2. This latency is calculated as the number of HERA clock cycles between the actual event and the arrival of the trigger. To detect cosmic muons with the HELIX chips, which are optimized for a bunched beam, the bunch structure of the HERA ring needed to be simulated. The randomly arriving trigger signal was synchronised with HERA clock cycles, thus the actual time between the event and the trigger could vary within 96 ns. As the sampling of the input signal at the HELIX happens at a fixed time after arrival of a trigger, this leads to a smearing in the energy deposition measurement. To correct for this, a TDC was installed, sampling the time between the actual trigger signal and the next HERA clock cycle.

Figure 8.16 shows the same plots for data taken with an incorrect latency setting. Here the HELIX pipeline cell corresponding to the 96 ns time slice before the actual event has been read out. The n-side still shows some correlated events, this is an indication that there was a small overlap in the timing such that the peaking time of the input amplifier stretched over two sampling time slices. This is caused by an incorrect setting of the timing difference between the p- and the n-side of the detector.

To reconstruct the energy deposited by cosmic muons it was necessary to reduce the noise present in the data. Events with a common mode above 30 ADC channels were discarded, for all events the linear weighted common mode correction as described above was applied afterwards. A hit found in the silicon sensors was considered to belong to a cosmic particle if it was within 1 cm of a track intersecting

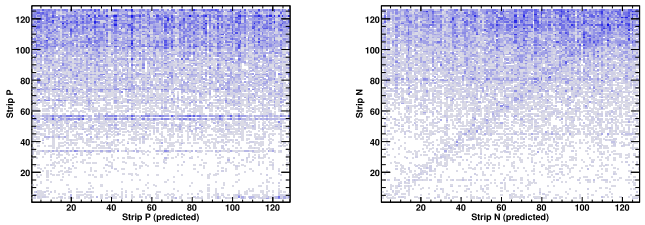

(a) p side (b) n side

Figure 8.16: Hit strip versus prediction by XTC for data taken with incorrect timing.

the silicon. Hits further away than 2 cm of a track were taken as noise hits. The TDC data has not been included in this analysis.

Figure 8.17 compares the energy deposition for hits associated with a track (shaded) with the equivalent energy deposition of noise hits. The ADC threshold was set to 10 ADC channels, equivalent to 57 keV energy deposition. The noise distribution shows a distinctive peak around 700 keV and raises also to lower energies. This is probably caused by failed common mode correction, the common mode being so high that all of the first 32 strips were above threshold for common mode calculation. For the hits associated to the track, on the p-side (Figure 8.17(a))it is not possible to distinguish a peak from the pedestal flank reaching above the ADC threshold, while on the n-side (Figure 8.17(b)) a peak can be seen in the data. Figure 8.18 shows the energy deposition corrected for the incidence angle of the track with respect to the sensor. Fitting a Landau distribution to these histograms gives a most probable energy deposition of 60 keV for the p-side and of 72 keV for the n-side. For the p-side this fit is not trustworthy, as the data cannot be distinguished from noise. For the n-side it is more convincing although the most probable energy deposition seen is slightly lower than the expected value of 79.2 keV for a minimum ionising particle in a 300 µm thick silicon sensor [Group02]. The thicknesses of the sensors installed are between 297 µm and 318 µm, so an energy deposition up to 7% higher could be expected. The lower value seen is due to a still preliminary calibration of the sensors based on very high energy depositions from protons and a still significant dilution with noise hits. Taking the most probable energy deposition as measured and given

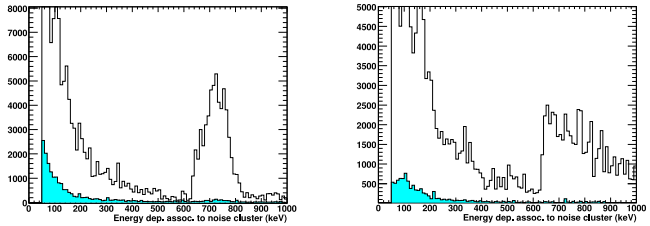

(a) p side (b) n side

Figure 8.17: Energy spectrum of noise hits (white) in comparison with the spectrum of hits related to a track (shaded).

a pedestal width of around 6 ADC channels after offline common mode correction (equiv. 34 keV), the signal to noise ratio is around 2:1.

A similar analysis has been performed by I. Vilardi, L. Lagamba and F. Stinzing. Using hits in the Photon Detector a corridor was defined, along which hits in the silicon were searched. The analysis also included a cut to a small timing window measured by the TDC, therefore reducing the smearing due to the rise time of the HELIX input amplifier. To reduce the noise, only events were taken if a single hit in the inner and also in the outer silicon layer were found. The resulting statistics is much lower in this approach, but the energy deposition is determined more precisely. Figure 8.19 shows the results for the n-side of a single sensor for muons passing at an angle of 45° to the detector. The most probable energy deposition is 19 ADC channels (taking into account the 50 channel offset present in the data), corresponding to an energy deposition of 76 keV per 300 µm silicon [VL05].

It could be shown that —even though the noise was much higher than expected— it was possible to detect Minimum Ionising Particles with the Silicon Recoil Detector and to determine their energy deposition within reasonable errors. Together with the measurements at the Erlangen Tandem accelerator it was shown that the detector can operate at the full dynamic range from MIPs up to protons stopped in the silicon [Vog08]. For moderate common mode noise an offline correction for the strip dependence of the noise can be done. Electrical modifications done after the test experiment lowered the noise present in the system drastically, thus allowing to

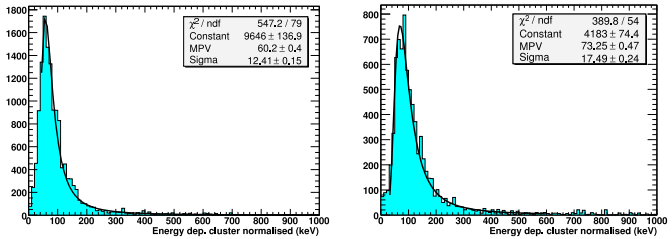

(a) p side (b) n side

Figure 8.18: Energy deposition of cosmic muons corrected for incident angle.

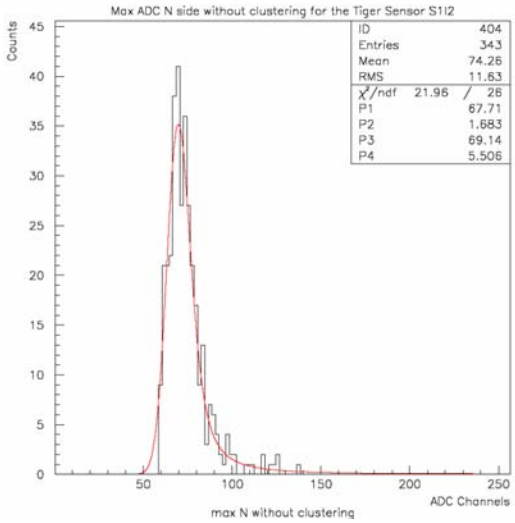

Figure 8.19: Energy deposition for cosmic muons reconstructed by I. Vilardi.

determine the energy deposition of MIPs with a much better signal to noise ratio of about 5:1, as shown in the next chapter.

9 First Data

"Look! It's moving. It's alive. It's alive..."
Henry Frankenstein (Colin Clive) in the movie Frankenstein (1931)

During the winter shutdown 2005–2006 the Recoil Detector was installed at the Hermes experiment, commissioning and data taking started in February 2006. Inside the scattering chamber large pulsed electric and magnetic fields are induced by the bunched electron beam circulating in the HERA ring. These fields can induce resonances inside the scattering chamber and depolarise spin-polarised hydrogen and deuterium [Tai06], they are also a very hard environment for an energy measuring silicon detector. To reduce the wake fields and the energy losses of the beam due to these fields, the beam has to be contained in a continous and smooth beam pipe. The energy loss in a non-smooth beam pipe section could easily reach a couple of kilo-Watts. To ensure the continous electrical enclosure, the target cell is connected by specially designed spring fingers to the beam pipe. Before installation an RF-Test simulating the HERA beam with sine waves (frequency domain measurements) and short pulses (time domain measurements) travelling through a small wire prooved the spring fingers working. It also showed the influence of the electromagnetic fields on the silicon detector to be small, however a small but constant pedestal shift was observed [YDG+05].

In the first weeks of HERA running very high noise and a strong dependence of the pedestal position on the beam parameters was observed. Figure 9.1 shows the development of the average noise width (Panel 9.1(a)) and the average pedestal position (Panel 9.1(b)) of one Helix chip over a complete HERA fill. The first two vertical lines from the left mark the beginning and end of a beam tuning. The third line corresponds to a sharp drop in the electron beam lifetime. During the beam tuning the position of the beam was varied and a strong change in noise and pedestal position could be seen. The lifetime drop showed no effects.

In parallel the target cell also showed a strong temperature dependence on the beam parameters. It could be traced to various possible sources: a wrongly mounted

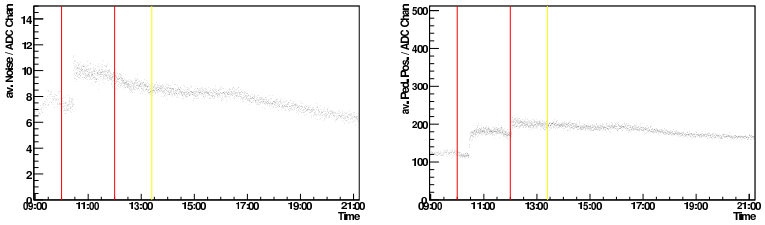

(a) Noise (b) Pedestal position

Figure 9.1: Noise width and pedestal position over a fill before installation of the electromagnetic shielding.

junction piece, which caused an discontinuity in the beam pipe; the target optical monitor, a measurement device no longer used, which could induce resonances with the new target chamber; and an insufficient cooling of the target cell in conjunction with a too thin target cell wall. After correcting these possible sources the target temperature stayed constant. During the exchange of the junction piece the silicon detector was also covered with an electromagnetic shielding made of copper and gold covered kapton. This reduced the noise notably.

A pedestal shift was still observed afterwards. The pedestal position of a single strip showed a correlation to the beam current, most strips' pedestal position varies about 10 ADC strips as shown for a typical strip in Figure 9.2(a). Shown is the position of the pedestal with beam relative to it's position without beam for varying beam currents. Figure 9.2(b) shows the strip with the largest change in pedestal position. The strip directly next to it (shown in Figure 9.2(c)) and the corresponding low gain strip (Figure 9.2(d)) have a much weaker variation in pedestal position in correlation to the beam current. No systematic dependence of the variation on the strip position has yet been found. The variation is reproducible: each colour in the plots represent a period of a couple of months of data taking, where the dependence of the pedestal position on the beam current is stable and therefore can be corrected offline. The width of the curve is around 5 ADC channels.

Figure 9.3 depicts the pedestal position of a single strip over the whole period of

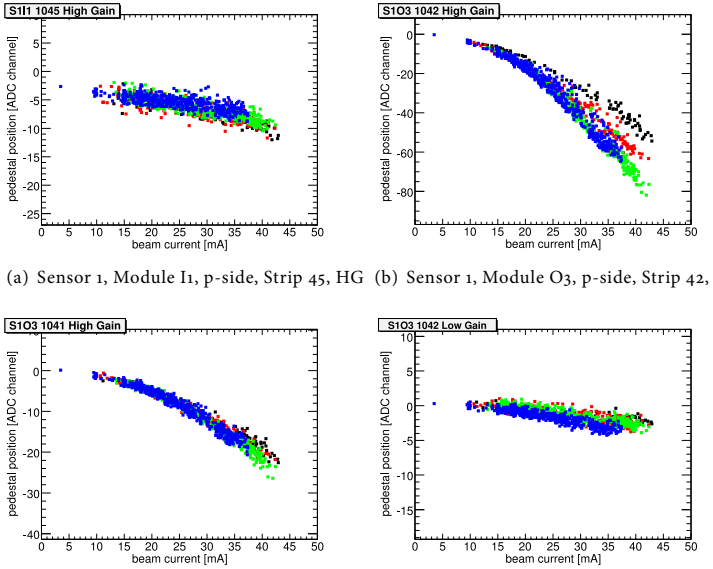

(a) Sensor 1, Module I1, p-side, Strip 45, HG (b) Sensor 1, Module O3, p-side, Strip 42, HG

(c) Sensor 1, Module O3, p-side, Strip 41, HG (d) Sensor 1, Module O3, p-side, Strip 42, LG

Figure 9.2: Shift of the pedestal position of a single strip with varying beam current.

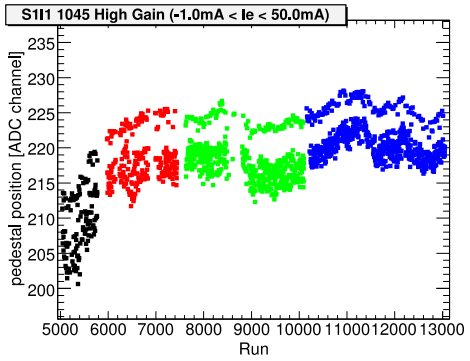

Figure 9.3: Pedestal position of a single strip over the whole period of data taking.

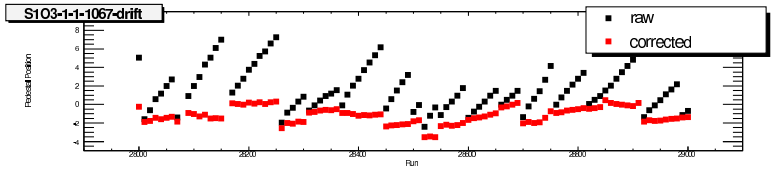

Figure 9.4: Pedestal position of a single strip over some HERA fills before and after correction.

data taking. The upper band corresponds to the pedestal position without beam (taken in a servicing run before each fill), the lower band shows the pedestal position with beam, showing the dependence on the beam current as stated above. The colours correspond to the phases of stable dependence to the beam current, as in Figure 9.2. The servicing runs before each fill determine the position of the pedestal, a correction for the pedestal shift with varying beam current is applied to the data, based on a fit to the dependence of the pedestal position to the beam current as shown in Figure 9.2.

The effect of this correction is shown in Figure 9.4 for a single strip. The strip shown is read out always to serve as a base point for the common mode correction

described in the next paragraph. Shown is the position of the pedestal during the fill relative to the pedestal position determined with a servicing run before the fill. The black squares denote the uncorrected position, the red ones the corrected position. The variation with beam current is clearly seen with the uncorrected data, each continous rising section corresponds to one HERA fill. The corrected data varies less then 1 ADC channel during one fill, however jumps between the pedestal position measured without beam and the pedestal position during a fill of around 2 to 3 ADC channels are observed, resulting in the steps seen between the fills. These jumps will be taken care of in the next version of the correction algorithm.

To correct for common mode effects, a spline based common mode correction is applied to the data. Every 8th strip of each sensor is read out unsparsified. For each event a spline is laid through these data points and then used to correct the data. This method is reducing the common mode better than the methods shown before, but requires the unsparsified read out of the spline's base points. It was developed by A. Mussgiller. Figure 9.5 shows the effect of the correction for a single HELIX chip for completely unsparsified data. In Figure 9.5(a) the pedestal subtracted data with common mode correction as done by the HADC is shown. The first 16 strips show low noise, the average noise width is around 5 ADC channels; the noise width rises to higher strip numbers. Figure 9.5(b) depicts the same with the spline correction applied. For the strips used as base points for the spline fit the noise is effectively reduced to zero; the noise of all other strips is enlarged in the order of the pedestal width of the spline base-point's uncorrelated noise width. The average noise for all strips is around 3 ADC channels, thus allowing the detection of Minimum Ionising Particles with a signal to noise of about 5 : 1. The noise width stays constant over the sensor.

Figure 9.6 shows the energy deposition for Minimum Ionising Particles determined from the signals of 10 strips on the n-side of a sensor. The plot is based on data from 10 HERMES runs, selected were particles with a reconstructed momentum larger than 1.5 GeV/c. The energy deposition is corrected for the incidence angle. Taking into account the measured thickness of the sensor of 299 µm, a most probable energy deposition of 79.1 keV would be expected. The lower value observed is due to a still preliminary calibration, which is derived from proton data with high energy depositions.

In Figure 9.7 the energy deposition of particles in the inner silicon layer is plotted against their energy deposition in the outer layer. The two solid lines represent the expected energy deposition based on a simulation with the GEANT4 toolkit

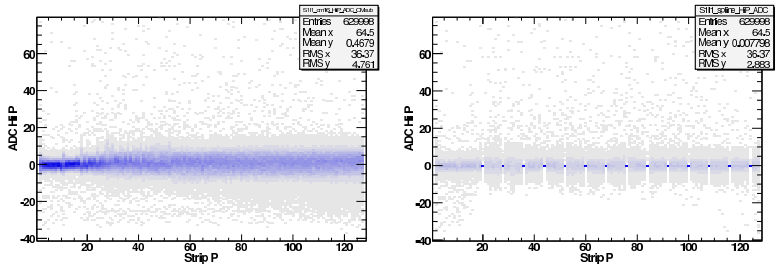

(a) With HADC CMN correction (b) With spline CMN correction

Figure 9.5: HADC common mode correction and spline based common mode correction.

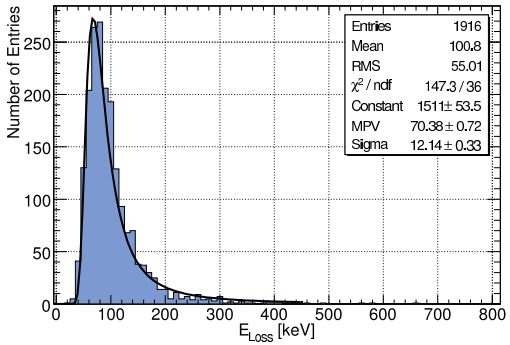

Figure 9.6: Energy loss for cosmic muons (data of 10 strips, outer layer quadrant 4, sensor 1, n-side).

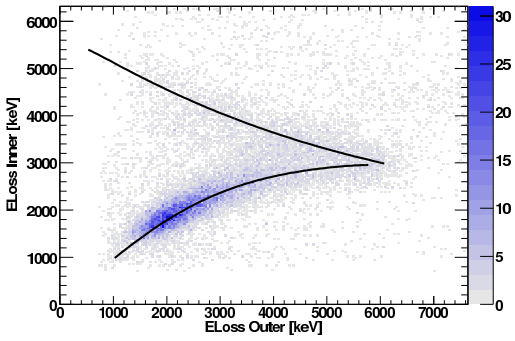

Figure 9.7: Energy deposition in the inner silicon layer versus energy deposition in the outer silicon layer.

[GEANT403]. Low energy protons passing the inner layer and getting stuck in the outer layer represent the upper branch in the plot. The punch-through point at an energy deposition of 6.2 MeV in the outer silicon layer is clearly visible, marking the highest energy deposition observed for protons. The lower branch are particles passing both layers of silicon. The energy of the particles rises in the upper band from the left to the right, in the lower band from the right to the left. The data is a combination of data from the high gain and low gain HELIXes.

The signal in the high gain channel plotted against the signal in the low gain channel of a HELIX chip is shown in Figure 9.8. The high gain channel goes into saturation at around 600 ADC channels (corresponding to an energy deposition of 3.4 MeV), energy depositions above this are measured using the low gain channel up to an energy deposition of about 12 MeV. The small branch with a deviating slope is caused by high gain strips, where the neighbouring strip's high gain HELIX channel is already in saturation. If an HELIX channel goes into saturation, its input capacity changes. This changes the capacitive network built by the neighbouring strips and the charge division into high and low gain, resulting in a slightly different charge split up. This effect will be included in the calibration.

Figure 9.9 shows the angle θ of proton tracks reconstructed from silicon hits alone

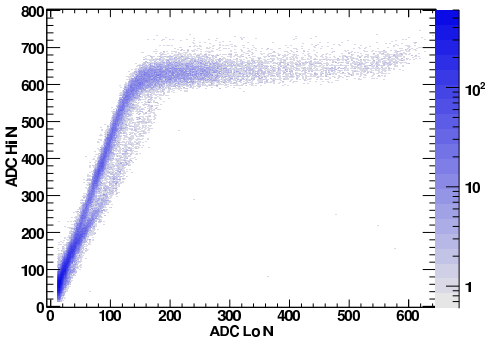

Figure 9.8: Signal in the high gain channel against signal in the low gain channel.

against the momentum of the scattered lepton determined with the spectrometer. For comparison the Monte Carlo simulated data for Deep-Inelastic Scattering (Figure 9.9(b)) and for elastic e-p-scattering (Figure 9.9(c)) are shown. It is possible to separate these two scattering processes quite well using silicon data alone. The elastic e-p-scattering can be used for an additional detector calibration, as the kinematics are exactly calculable; using the scattering angle of the lepton measured by the spectrometer, the energy of the proton is calculable.

The particle identification capabilities of the silicon detector are shown in Figure 9.10. Shown is the energy loss in the outer silicon layer plotted against the momentum reconstructed from the particle track, for the inner silicon layer the plot looks very similar. The data were taken using a positron beam. Only tracks with three or four reconstructed space points in the Recoil Detector were used, low energy particles which do not reach the Scintillating Fibre Detector are not included. The momenta were reconstructed from the curvature of the track in the magnetic field of the recoil detector's magnet. Negative momenta represent particles with negative electric charge, mainly π^- and K^-. In the right half (positive momenta) the separation between the lower band corresponding to π^+/K^+ and the upper band corresponding to protons is quite distinct. A good particle identification is needed to distinguish mesons produced directly fom DVCS processes from mesons originating from decay

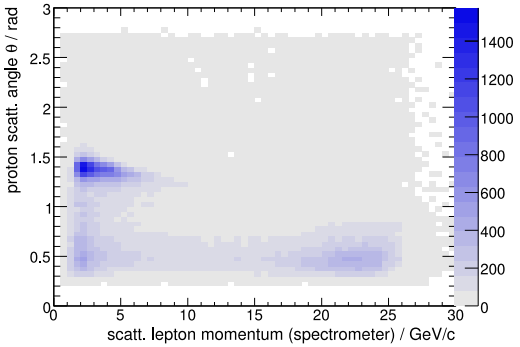

(a) Data measured.

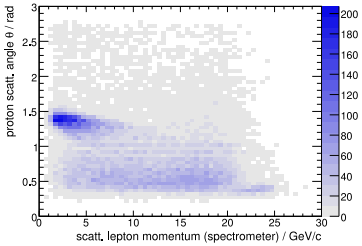

(b) Monte Carlo DIS.

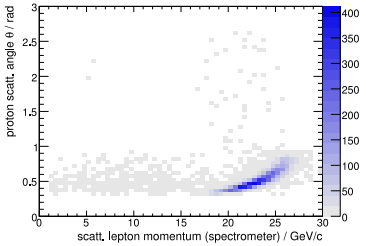

(c) Monte Carlo elastic e-p scattering.

Figure 9.9: The angle θ of a track reconstructed by silicon data against the momentum reconstructed with the spectrometer.

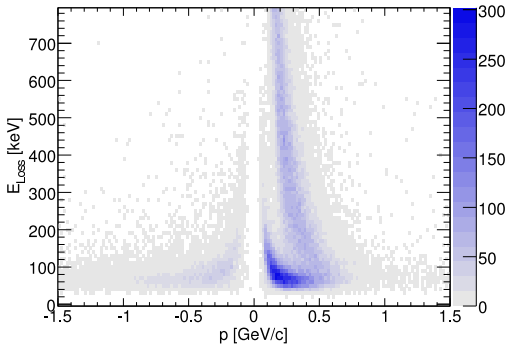

Figure 9.10: Energy loss in the outer Silicon layer against momentum reconstructed by track reconstruction for the Recoil Detector only.

processes like $\Delta^+ \to n\pi^+$ (see Section 2.2). The tracking algorithms used for this plot do not yet include the correct beam position, but assume the beam to pass at $x = 0$ and $y = 0$. The separation between protons and pions is expected to improve with the inclusion of the correct beam position.

The HERMES Silicon Recoil Detector has been taking data from May 2006 up to the end of HERA running at June, 30th, 2007. In total, 28 million DIS events (42k DVCS events) have been observed by HERMES with a positron beam, a hydrogen target and the full Recoil Detector in operation. Using a deuterium target, data from 7 million DIS events (10k DVCS events) were collected.[1] About 60 to 70% of these events were within the acceptance of the Recoil Detector. In comparison, HERMES has detected about 10 million DIS events using a polarised target during the data taking phase from 2002 till 2005 before the installation of the Recoil Detector.

The improvement in Missing Mass resolution can be seen in Figure 9.11, based on Monte Carlo data (not yet normalised to the amount of data taken). The background due to semi-inclusive scattering is reduced to practically zero, the background con-

[1] Additional 7 million DIS (5k DVCS) events on hydrogen and 0.8 million DIS (1k DVCS) events on deuterium with an electron beam were detected in the early commissioning phase of the Recoil Detector, where only the Scintillating Fibre Tracker was fully operational.

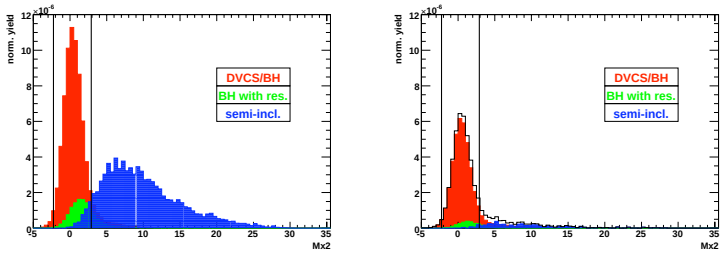

(a) Without Recoil Detector (b) With Recoil Detector

Figure 9.11: Distribution of the Missing Mass squared without and with the Recoil Detector (from Monte Carlo).

tribution of resonances produced in a Bethe-Heitler process is strongly suppressed. The two vertical lines represent the so far used cuts on the missing mass to ensure exclusivity. With the Recoil Detector in operation these cuts are no longer necessary.

A projection done by V. Korotkov based on Monte Carlo data for the Beam Spin Asymmetry error bars is shown in Figure 9.12. The open data points represent the HERMES measurements on the BSA published in [HERMES01], the filled points show the projection for the error size based on an integrated luminosity of 1 fb^{-1}. The number of bins in Φ is twice the number of bins in the published data, while the size of the error bars in the asymmetry is practically halved. Figure 9.13 (kindly provided by C. Riedl) gives a first glance at the Beam Spin Asymmetry on hydrogen. The plot is based on all data taken in 2007 with a hydrogen target (excluding a few runs which were not available or caused problems due to the very preliminary status of the data production). It was produced with the analysis code and the calibration data used for BSA analysis before the installation of the Recoil Detector, so the actual values have to be taken with a grain of salt and most probably will change. No information from the Recoil Detector was used for this analysis. The offset to positive values visible in the asymmetry is most probably caused by using a not up to date calibration of the calorimeter, similar effects have been seen in earlier analyses

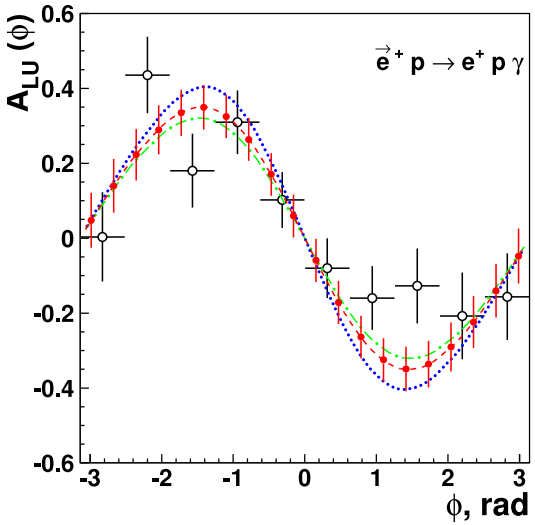

Figure 9.12: Projections for the errors on the Beam Spin Asymmetry, calculated by V. Korotkov. The open points are data measured by HERMES the filled points show the projections for the size of the error bars, based on an integrated luminosity of 1 fb^{-1}

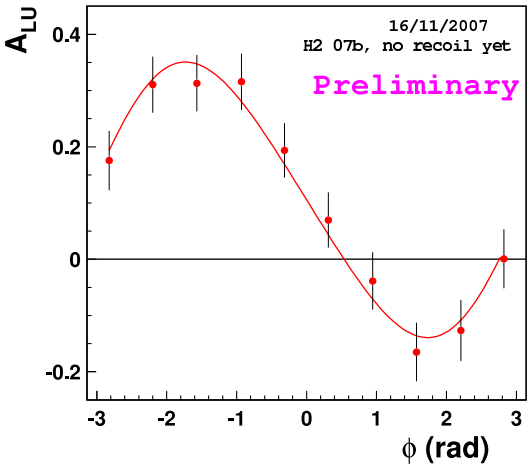

Figure 9.13: A first glance at the Beam Spin Asymmetry on hydrogen, using all data taken in 2007 on a hydrogen target. The results are based on an older analysis code, which does not include the recoil detector. It also does not use the correct calibration for the detectors, the actual values will change.

and disappeared when a correct calibration was included. Although the analysis is still at a very early stage, the great improvement in statistics already can be seen, the error is comparable with the projections shown in Figure 9.12. The systematic error will be greatly reduced when information from the Recoil Detector will be included.

Although situated within the harsh environment of the HERA beam pipe the Silicon Detector operated as planned. The high transient electromagnetic fields due to the circulating electron bunches inside the beam pipe made it necessary to correct for higher common mode noise and for a pedestal shift, which was shown to be feasible. The dynamic range of the detector is sufficient to determine the energy depositions from Minimum Ionising Particles to protons stopped in the sensors. Together with the other detectors of the HERMES Recoil detector a particle identification for protons and pions can be obtained. It could be shown, that the HERMES Recoil Detector is an ideal tool to suppress background events from the HERMES DVCS data sample. Together with the vast amount of data taken a great improvement in the measurement of the BSA is expected, which will allow to gain more precise information on GPDs.

10 Summary

> ❝But from a narrative point of view, in 105 pages nothing happens. Except this: 'What with one thing and another, three years passed.'❞
> *The Princess Bride, Chapter 4 – William Goldman*

GENERALISED PARTON DISTRIBUTIONS provide a unique way to gain more information on the substructure of the nucleon. So far measurements done by HERMES and other experiments have provided data on the longitudinal momentum distribution (Parton Distribution Functions) and the transverse spatial distribution (Form Factors) of the nucleon's constituents. Generalised Parton Distributions unite these two aspects in a single description and contain also additional information on the quark-gluon substructure of the nucleon. The most prominent example of this is Ji's sum rule, an integral over the sum of two GPDs, which allows the measurement of the quark's total angular momentum.

The cleanest way to experimentally determine GPDs is through Deeply Virtual Compton Scattering, the hard exclusive production of a real photon by scattering leptons off a hadron, and especially its interference with the Bethe-Heitler process. Various asymmetries with respect to the charge and spin of the incoming lepton as well as the spin of the target nucleon allow to access the real and imaginary parts of Compton Form Factors and through these to GPDs. The HERMES experiment has measured some of these asymmetries using the technique of missing mass reconstruction, as the recoiling nucleon is scattered under large angles and not detectable by the HERMES spectrometer. The versatility of the HERMES internal gas target allowed the study of DVCS on spin polarised as well as unpolarised hydrogen and deuterium targets and also on unpolarised heavier gases.

The resolution of these measurements however is limited by the accuracy of the missing mass reconstruction, which is dominated by the spatial and energy resolution of the spectrometer. Only the leading moments of some asymmetries could be measured. To obtain a higher accuracy the recoiling nucleon needs to be detected, thus eliminating the uncertainties originating from the missing mass

reconstruction. Requirements of this detector are the ability to measure the momenta of recoiling particles over a very wide range, from Minimum Ionising Particles up to protons stopped in the first detector layers, as well as the capability to identify and separate hadrons from mesons. A large spatial coverage is needed to enclose the target as complete as possible.

At the HERMES experiment the Recoil Detector was installed in the winter shutdown 2005–2006 and has been taking data from May 2006 till the end of HERA running on June 30th, 2007. The detector consists of three sub-detectors: a Silicon Detector located inside the scattering chamber, a Scintillating Fibre Tracker and a Photon Detector. It is located inside a 1 T superconducting magnet.

The Scintillating Fibre Tracker consists of four layers with more than 7000 fibres arranged in two cylinders, one directly around the scattering chamber, one at the inner edge of the Photon Detector. It provides space points for tracking as well as energy measurements. The Photon Detector is placed into the magnet's bore and consists of three layers of scintillators, one parallel to the beam, the other two with $\pm 45^\circ$ with respect to the beam axis. Before each layer a tungsten converter is placed. It's main purpose is the detection of photons originating in the decay of π^0 mesons which are produced by the decay of Δ resonances to a proton and a π^0, thus tagging the proton as not being the direct product of DVCS.

The Silicon Detector is located inside the scattering chamber, still within the HERA vacuum. It consists of 16 sensors with a size of 10×10 cm^2 arranged in 8 modules in two layers around the target cell. Each sensor features 128 strips on both sides, the strips on the n-side being perpendicular to those of the p-side. To be able to determine the energy deposition over a huge dynamic range from MIPs to protons stopped in the sensors a charge splitting read out has been devised. Each sensor is read out by a HELIX read-out chip connected directly to the sensor and additionally by a HELIX chip connected via a 10 pF capacitor, splitting the signal into a high gain and a low gain path. Energy depositions from the equivalent of 1 MIP up to the equivalent of 70 MIPs can be measured.

Before the installation in the experiment, the Silicon Detector modules were tested in a bench test and together with the complete Recoil Detector in a test experiment. During the work of this thesis, these tests were devised and performed. The necessary read out software had to be rewritten during this work. It was shown that the sensors worked according to specification, however due to high noise an improved noise correction was necessary. Various models were tested, which reduced the influence of the common mode noise significantly. A small change in the electrical setup done after the test experiment lowered the noise drastically. Despite the higher noise cosmic muons could be detected and their energy deposition measured with a signal to noise of 2:1.

In the winter shutdown 2005–2006 the detector was installed and successfully integrated in the HERMES experiment. Analysis tools and first data analyses were developed in the course of this work. Shortly after the installation very high noise in the silicon detector—correlated with the beam current—and an overheating of the target cell were observed. After solving some mechanical and electrical problems, the detector worked well. However a pedestal shift correlated to the beam current was seen, which can be corrected for offline.

The common mode noise seen showed a different influence on different strips. To correct for it, every 8th strip of each sensor is read out unsparsified; a spline is laid through these data and used to correct the common mode. An average noise of 3 ADC channels is observed, the pedestal width at the unsparsified strips is forced to zero by this method.

Energy depositions from Minimum Ionising Particles up to protons stopped in the silicon could be measured with the Silicon Detector. Minimum Ionising Particles can be detected with a signal to noise of 5:1. Together with information from the Scintillating Fibre Tracker protons can be distinguished from pions and other mesons. The HERMES Silicon Recoil Detector has been successfully commissioned and has taken data from May 2006 till the shutdown of the HERA storage ring end of June 2007. It could be shown that the charge sharing read out allows energy measurements over a very wide dynamic range and that an energy measuring silicon detector can successfully operate in the harsh environment inside the HERA beam pipe. The HERMES experiment has seen 28 million DIS events using a hydrogen target and a positron beam, an additional 7 million DIS events using a deuterium target. This is around four times the statistics achieved in the previous phase of running from 2002 till 2005 without the Recoil Detector. First analyses on the Beam Spin Asymmetry already show a great improvement in the size of the error. Including the data from the Recoil Detector will greatly improve the systematical error and allow a much more precise determination of the asymmetry. The HERMES Recoil Detector proofed to be a valuable tool in suppressing the Background in the measurement of DVCS processes.

A The Silicon Readout

The silicon readout hardware consists mainly of three modules: the ACC, a repeater board which merges the different control and read out lines onto a single cable for each silicon module side; the HADC which does the actual read out and digitisation; and the HLCU which steers the Helix chips and supplies the needed clock and trigger to the silicon modules.

A.1 The Analogue Circuit Control (ACC)

The Analogue Circuit Control, short ACC, is a repeater board for the analogue and digital signals coming from and going to the Helixchips. The digital signals coming from the HLCU are refreshed by TTL line drivers. The sync out signal coming from the Helix chips is also repeated by a TTL line driver. This signal has to be converted to NIM standard (for the HADC trigger input) with a high impedance converter: the TTL line driver on the ACC cannot drive a 50 Ω-terminated line. A Maxim amplifier drives the analogue signal line going to the HADC. A scheme of the ACC can be found in figure A.1 on the next page, a photograph is shown in Figure A.2.

The ACC also merges the two signal cables (CAT6, RJ45 connectors) from the HLCU, the signal cable to the HADC (CAT6, RJ45 connectors), the bias supply and the Helix low voltage supply cables into a single cable for each detector side. Various jumpers allow to connect or disconnect the cable shields to the detector ground level.

A.2 The Hermes ADC (HADC)

The Hermes ADC (or short HADC) was developed by NIKHEF for reading out the Lambda Wheels, which are based on the same readout chip as the Recoil Detector silicon modules. To profit from the already available experience and to re-use already

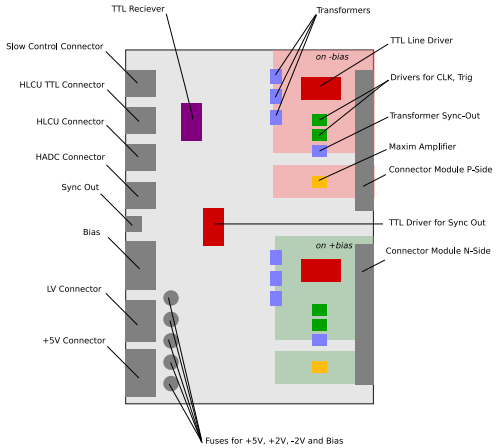

Figure A.1: Layout and descriptions of the individual parts of the ACC.

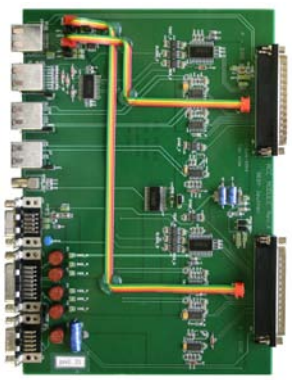

(a) Top view

(b) Front view

Figure A.2: Photo of an ACC.

existing read-out software these modules were also chosen to read out the recoil silicon.

Each HADC is divided into four 10-bit analog digital converters, each of which can read out one side of a module; in total each HADC can therefore read out two modules. It has an on board signal processing unit, realised in FPGA logic, to do on-line pedestal subtraction, common-mode noise correction and hit detection, allowing to read out only channels which have a signal higher than an adjustable threshold. Four subsequent events can be stored into so called ADC pages. The HADC can be read out in two different ways, either via accessing single 32-bit buffers in a simple VME single word read access, or in a block read mode, where each HADC acts as a single huge buffer containing all information. A third mode to read out multiple HADCs acting as one single buffer, handling the read out via VME interrupts 6 and 7 signals, is foreseen, but it was never used.

Input signals On the front panels there are two RJ45 inputs for the analogue signals, the upper one connected to ADCs 0 and 1, the lower one to ADCs 2 and 3. Each of these inputs should only be used for a specific side, as they are still on

detector potential. In the recoil detector setup as in the Lambda Wheel setup, the upper ADCs (0 and 1) are used to read out the p-side (or junction side) and the lower ADCs (2 and 3) are used to read out the n-side (or ohmic side) of the modules. The signal lines are on bias potential up to the HADC. For this setup a special switch box is needed to separate the p- and n-side signals from each of the two modules connected to one HADC and merge the two p-side and the two n-side signal lines into one cable each.

Additionally to the analogue signal inputs, there are four Lemo inputs for digital NIM signals: the 10.4 MHz HERA-clock; the trigger input, which is the sync out signal (TTL) coming from the HELIX chips inverted and converted to NIM-level ($(128 + 8) \times 4$ clock cycles length, or 52.2 µs); and a Reject and Accept pulse. The Accept and Reject pulses are needed, if the HADC is read out in block read mode, an event will be transferred to the readout buffer if an Accept pulse arrives a certain time after the trigger signal (at least six clock cycles after the beginning of the sync out signal, latest before the initiating of the read out). If a reject pulse arrives, this event will be discarded.

Jumper settings The HADC has 45 jumpers, most of which should not be changed. A description of the jumpers and the default settings are found in table A.1 on the facing page. Jumpers with two pins are either open or closed, Jumpers with three pins are either position one (left or top pins connected, the position is defined that, when looking at the module, the front panel is on the left side) or position two (right or bottom pins connected). The signal lines need to be terminated, the clock and trigger signals should be terminated if the setup requires it. At the recoil installation the clock lines of the HADCs are not terminated, it is done externally. The trigger lines are terminated. The signal coupling should always be AC.

Event processing The automatic event processing running in the HADC occurs in four steps. In the first step the signals from the HELIX-chips are digitised by a ten-bit ADC while the HELIX sync-out signal is present. In the second step a previously loaded pedestal value for each channel is subtracted, leaving a small positive but constant value (50 ADC channels, hard coded in the HADC) to avoid negative results which may be caused by some remnants of common-mode noise left in the system. The amount of the common-mode noise is determined in the third step, where the average of 16 out of the first 32 live strips in each chip is determined,

Table A.1: The HADC Jumpers and their default settings.

Jumper	Default	Function
1	open	ADC-0, pos-signal, closed DC, open: AC-coupling
2	open	ADC-0, neg-signal, closed DC, open: AC-coupling
3	open	ADC-0, open: low gain, closed: high gain
4	pos 2	ADC-0, pos-input, pos 1: DC, pos 2: AC coupling
5	pos 2	ADC-0, neg-input, pos 1: DC, pos 2: AC coupling
6	closed	ADC-0, open: no termination (do not use!), closed: 100 Ω
7	pos 1	ADC-1, pos-input, pos 2: DC, pos 1: AC coupling
8	closed	ADC-1, open: no termination (do not use!), closed: 100 Ω
9	pos 2	ADC-1, neg-input, pos 1: DC, pos 2: AC coupling
10	open	ADC-1, open: low gain, closed: high gain
11	open	ADC-1, pos-signal, closed DC, open: AC-coupling
12	open	ADC-1, neg-signal, closed DC, open: AC-coupling
13	pos 1	clock-0 skew (do not change)
15	open	50 ohm termination on CLK-input
19	open	50 ohm termination on Accept-input
20	pos 1	clock-0 skew (do not change)
22	open	50 ohm termination on Reject-input
26	open	50 ohm termination on TRIG-input
27	pos 2	clock-1 skew (do not change)
29	closed	connects IRQ-6 to VME-bus
31	pos 2	clock-1 skew (do not change)
32	closed	connects Dtack to VME-bus
33	closed	connects IRQ-7 to VME-bus
34	open	ADC-2, pos-signal, closed DC, open: AC-coupling
35	open	ADC-2, neg-signal, closed DC, open: AC-coupling
36	open	ADC-2, open: low gain, closed: high gain
37	pos 2	ADC-2, pos-input, pos 1: DC, pos 2: AC coupling
38	pos 2	ADC-2, neg-input, pos 1: DC, pos 2: AC coupling
39	open	ADC-2, open: no termination (do not use), closed: 100 Ω
40	open	ADC-3, open: no termination (do not use), closed: 100 Ω
41	pos 1	ADC-3, pos-input, pos 2: DC, pos 1: AC coupling
42	pos 2	ADC-3, neg-input, pos 1: DC, pos 2: AC coupling
43	open	ADC-3, open: low gain, closed: high gain
44	open	ADC-3, pos-signal, closed DC, open: AC-coupling
45	open	ADC-3, neg-signal, closed DC, open: AC-coupling

skipping those channels which have a content greater than a predefined value (*high threshold*), thus avoiding the inclusion of real hits in the common mode estimate. The result is then subtracted from all strips of this chip (the above mentioned offset of 50 ADC channels is not subtracted!). According to the documentation of the Lambda Wheel [The] this procedure reduces the effect of the common-mode noise on the measured width of the baseline to less than 10%, even when the common-mode itself is twice the random noise on a strip. After the pedestal and common-mode subtraction a hit detection is done. Only strips above a preset threshold are kept in memory for read out. The registers used for the event processing are shown in table A.2. If the common-mode is so strong, that all of the first 32 strips are above the *high threshold*, neither common-mode nor pedestal subtraction is performed, but the unprocessed event is passed to the readout buffer.

Strips can be marked dead by setting the 11th bit in it's pedestal register to `0`. When the HADC is initialised, the pedestal memory is set to `0` for all strips, strips have to be explicitly enabled to get read out.

Table A.2: The HADC registers used for event processing. The pedestal memory consists of a 10-bit pedestal value, the 11th bit is used to enable and disable the read out of a channel (1 = read out, 0 = ignore).

Register	Valid Bits	Content
`0x000000` ... `0x000ffc`	11	Pedestal Memory ADC0 (1024 values)
`0x001000` ... `0x001ffc`	11	Pedestal Memory ADC1 (1024 values)
`0x002000` ... `0x002ffc`	11	Pedestal Memory ADC2 (1024 values)
`0x003000` ... `0x003ffc`	11	Pedestal Memory ADC3 (1024 values)
`0x004000`	10	Hit threshold ADC0
`0x004004`	10	Hit threshold ADC1
`0x004008`	10	Hit threshold ADC2
`0x00400C`	10	Hit threshold ADC3
`0x004010`	10	High threshold ADC0
`0x004014`	10	High threshold ADC1
`0x004018`	10	High threshold ADC2
`0x00401C`	10	High threshold ADC3

Controlling of the HADC The control status register defines the operation of the HADC, its settings are shown in table A.3 on the following page. The number of HELIX chips is coded in bit `1`. If the bit equals zero, 4 HELIX chips are installed in one chain, if equal one, 8 HELIX chips are installed in one chain. The test-mode bits are for maintenance and need to be set to `0xF`, a documentation was not available to the recoil group. By default the polarity of ADC0 and 1 is 0, of ADC2 and 3 the polarity is 1. These settings ensure positive signals for both sides of the detector.

"Extended header" defines if the trailers are checked and the respective words are generated in the header. During normal operation extended header, common-mode and pedestal subtraction should be on, while trigger interlock should be off. The IRQ 7 bit controls the module behaviour if it is read out in the multiple HADCs block read mode; IRQ = 0 means the module generates a IRQ6 when the event is finished, while when IRQ = 1 an IRQ7 is generated. For all modules except the last in the read-out chain, this bit should be off.

The counter called "COUNT" in the status register is incremented as soon as a trigger arrives. The actual event is available about 60 µs after the arrival of a trigger and can only then be read out. When the read out is finished the counter is decremented again.

The "CARD ID" is set by switch SW3. In block read mode this will be part of the first header word. The number set on switch SW3 will be inverted in the electronics: e.g. when the switch reads D (binary `1101`, 13 decimal), it reads back binary `0010` (decimal 2).

The incoming signal to the ADCs can be shifted by a programmable offset. If internal trigger generation is set, a trigger can be generated if the signal is above a threshold. These settings are made in the registers described in table A.4.

Trailer Checking is enabled for ADC 0 and 1 by setting register `0x004050`, for ADC 2 and 3 by register `0x004054`. Switching the Acquisition mode and clearing the HADC can be done by accessing the registers shown in table A.5. The status register described in table A.6 controls the behaviour of the four ADCs and selects the used trigger source.

The HADC has to be initialised before data taking. This is done in `daq4servicing` in the following order:

1. Switch off Acquisition mode,
2. Send a *Global Clear*,
3. Send a *Clear Flags*,
4. Set the config and status registers,

Table A.3: The HADC control and status register (base address + 0x004020)

Bit	Name	Content
0	ACQ	Acquisition Mode
1	NO_HELIX	Number of Helixes. Bit=0: 4, Bit=1: 8
2	EXTHDR	Extended Header
3	COMMOD_SUB	Common Mode Substraction
4	PEDESTAL_SUB	Pedestal Substraction
5	TRIG_ILOCK	Trigger Interlock
6 – 9	TEST_MODE	NIKHEF-internal ADC test-mode (always set to 0xF!)
10	IRQ_7	If Bit is set the IRQ is 7, else it's 6
11	POL_0_1	Polarity of ADC for channels 0, 1
12	POL_2_3	Polarity of ADC for channels 2, 3
13	SYNC_ERR	Sync Error: acquisition length longer than physically possible.
14	DPM_OFLOW	Acquisition buffer is full (dpmfull LED)
15	TRIG_REJECT	Trigger Reject
16 –19	CARD_ID	Card ID (set by Jumper SW_3)
20 –22	COUNT	Number of pages acquired

Table A.4: The HADC DAC Offset and Threshold registers

Register Address	Bits	Content
0x004040	0-11	Offset DAC for ADC 0
	12-23	Threshold for ADC 0
0x004044	0-11	Offset DAC for ADC 1
	12-23	Threshold for ADC 1
0x004048	0-11	Offset DAC for ADC 2
	12-23	Threshold for ADC 2
0x00404C	0-11	Offset DAC for ADC 2
	2-23	Threshold for ADC 2

Table A.5: The HADC instruction registers

Register Address	Instruction
0x00402C	Clear
0x004064	Clear Flags
0x004068	Acquisition mode on
0x00406C	Acquisition mode off
0x004074	Clear Counters

Table A.6: The HADC ADC status registers

Register Address	Bits	Content
0x004058		ADC mode and status ADC 0 and 1
	0-3	Data Valid Delay in clock cycles
	4	Invert clock of sync logic
	5	Invert trailer bits
	6-12	Trigger select
		6: Data valid 0 (int. generated)
		7: Data valid 1 (int. generated)
		8: Invert DV0
		9: Invert DV1
		10: external trigger
		11: invert external trigger
		12: DV0 & DV1 & ext. Trigger
0x00405C		ADC mode and status ADC 2 and 3 (bits as above)

5. Set the offsets,
6. Set the thresholds,
7. Load the pedestals,
8. Switch on acquisition mode again.

A.2.1 The Helix control unit (HLCU)

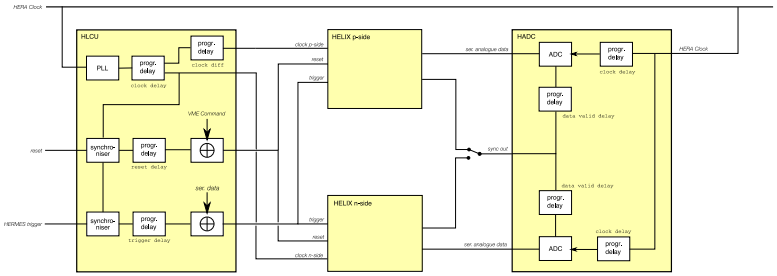

Figure A.3: Schematics of the delays.

The silicon modules are controlled and programmed by the HLCU (Helix Logical Control Unit). This module handles the triggering for the silicon and switches the HELIXes between read out and data acquisition mode. As input it gets the HERA Clock and the HERMES Trigger via Lemo inputs on the front panel. A test pulse and a reset signal can be passed in the HLCU via two additional Lemo inputs. All externally provided signals are NIM-Signals. Programming of the HLCU and the HELIXes is accomplished via the VME interface. The VME register addresses relative to the base address can be found in table A.7.

The base address is set with jumpers GA 0…4 (see figure A.4). All accesses are 32 bit (data) and 24 bit (addresses). If no jumpers are installed the module address is by default `0x180000`, otherwise the address bits 19…23 are set by the jumpers. An installed jumper corresponds to a 1 in the bitpattern making up the address.

The Control and Status register contains information and flags about the HLCU status. Details are found in table A.8. The flags can be set via the Bit-Set register and cleared via the Bit-Clear register.

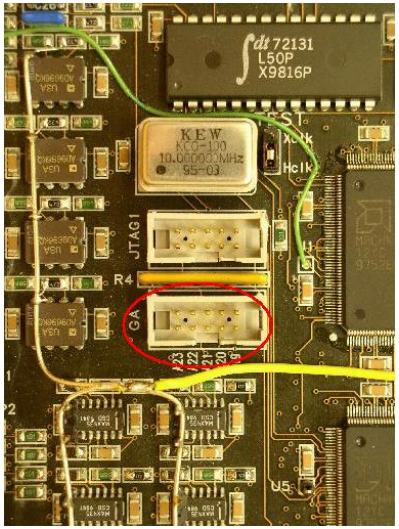

Figure A.4: Address Jumpers of the HLCU.

Table A.7: The VME address map of an HLCU.

Address	Length	Access	Valid bits	Function
0x000000	0x4	R	8	Baseaddress register
0x000100	0x4	R	10	Control/status register
0x000104	0x4	W	10	Bit-Set register
0x000108	0x4	W	10	Bit-Clear register
0x000200	0x4	W	27	HELIX write-FIFO
0x000204	0x4	R	27	HELIX read-FIFO
0x000300	0x4	R/W	9	Clock delay
0x000304	0x4	R/W	8	Clock difference
0x000308	0x4	R/W	8	Trigger delay
0x00030C	0x4	R/W	8	SLoad delay
0x000310	0x4	R/W	8	Reset delay
0x000314	0x4	R/W	8	Testpulse difference

Table A.8: The bits of the HLCUs Control and Status register.

Bit	Name	Meaning
CSR[0]	HLCU_RUN	HLCU Run-Bit
CSR[1]	HLCU_ERROR	HLCU Error-Bit
CSR[2]	SYSRESET	HLCU Not-Reset-Bit
CSR[3]	RESET_WRFIFO	Command: Reset Write-FIFO
CSR[4]	RESET_RDFIFO	Command: Reset Read-FIFO
CSR[5]	NOT_RESET	Helix-RESET-Line
CSR[6]	WRFIFO_EMPTY	Write-FIFO is Empty
CSR[7]	WRFIFO_FULL	Write-FIFO is Full
CSR[8]	RDFIFO_EMPTY	Read-FIFO is Empty
CSR[9]	RDFIFO_FULL	Read-FIFO is Full

The HELIXes are programmed via the HELIX-write-FIFO. The HELIX read-FIFO contains the data that was sent to the HELIX. The structure of these registers is found in table A.9.

Table A.9: The bits of HELIX fifos (write and read).

Bit		Meaning
WRFIFO[0…19]		Data sent to helix-chain with SLOAD
	0– 7	Register Value
	8–12	Register Address
	13–18	Chip-Address
	19	Chip-Address Broadcast-Bit
WRFIFO[20…21]		Segment to broadcast onto (0…3)
WRFIFO[22]		Enable all segments to broadcast

One HLCU can control four Silicon Modules. Each module is connected via two RJ45 cables, labelled “current” and “TTL”. The current lines provide the clock and the trigger signals for both sides of a module as LVDS signals. The TTL lines transmit the test-pulse for p- and n-side, the reset signal and the SLOAD-signal for the Helix chips. On the ACC the corresponding connectors are labeled HLCU LVDS (current signals) and HLCU (TTL signals).

The clock provided by the HLCU can be delayed to ensure optimum sampling of the detector signal, as the sampling point is defined by the raising edge of the clock. In silicon detectors the charge collection time is smaller for the ohmic side (n-side) than for the junction side (p-side). The clock can be delayed by a programmable delay via the parameter *clock delay*; the junction side clock is then additionally retarded by another programmable delay with the parameter *clock difference*.

The provided trigger signal can also be delayed via the parameter *trigger delay*. It should arrive on both sides so that a positive edge of the clock signal is within the trigger signal. The same applies for the SLOAD signal, which can be retarded with the parameter *SLOAD delay*. A scheme of the signal delays can be found in figure A.3.

To check the charge collection of the Helix a test pulse can be passed to the it. This testpulse signal should appear before the trigger and needs to be at least 2 µs

long. The test pulse injects into the HELIX a charge equivalent of 2, 1, -1 and -2 times 24.000 electrons (the charge generated by a MIP in a 300 µm thick silicon sensor). It injects 2 MIPs into HELIX channels 1, 5, 9, …; 1 MIP into channels 2, 6, 10, …; -1 MIP into channels 3, 7, 11, …; and -2 MIPs into channels 4, 8, 12, … The polarity of the signal changes after each injection.

Table A.10: The HLCU input signals. All Signals are according to the NIM standard.

Name	Signal
Trigger	~ 100 ns (1 clock cycle) pulse, starting the read-out of the HELIX chips. Please note: when two clockcycles are present within the duration of the trigger, *two* events will be triggered.
Clock	the sample clock for the HELIX chips, duty cycle about 50%.
Reset	blocks the HELIX read-out when active, after reset the pipeline address counter in the HELIX is set to zero. Min. length 3 clock cycles.
Testpulse	a signal at least 2 µs long, arriving some time before the trigger

A.3 Auxiliary hardware

All supply voltages for the ACCs and the HELIXes are generated by low voltage modules designed by NIKHEF for the Lambda Wheels, which were manufactured by Glasgow University. The HELIX chips are connected to the LV-modules, the ACCs get the necessary 5 V supply voltage from the AUX module. The output of the LV and the AUX modules is monitored by the SpiCan module, which can also switch the LV modules on or off. The bias voltage for the silicon sensors is created by standard CAEN high voltage boards integrated into the HERMES HV control chain.

(a) Front view (b) Side view

Figure A.5: Photograph of a LV module. Shown is an older version, the Bias connector at the top has since been removed.

A.3.1 LV Supply

The LV supply provides the two voltages for the HELIXes, VSS (-2 V) and VDD (+2 V). These voltages also supply some electronics on the ACC, namely the Maxim amplifier. One LV module can supply one silicon module; the voltages and currents for p- and n-side can be set seperately via screws at the front of the LV module. The maximum current output is 2 A. The Voltages are controlled by an UC3834 linear regulator. The "Top" half of the LV module is connected to the n-side, the "Bot"(tom) half of the module is connected to the p-side of the silicon detector module. The outputs are floating with respect to ground; when connected to a biased silicon module the top and bottom half of the LV supply will be on bias potential of the n- and the p-side, respectively.

The LV supplies have been manufactured to be identical to the ones used by the Lambda Wheels, except that the connector for the pass through of the bias voltage has been removed. The backplane layout is identical, so it is possible to use the same spares as the Lambda Wheels.

Two LV modules are supplied by one low capacitance transformer with ±5 V, which is controlled by a set of MAX466 ICs to an accuracy of 5%. In total four of these transformers supply the LV crate. An additional standard transformer provides the supplies for the AUX and the SpiCan modules described later.

Each power-supply module half employs a Cirrus Logic CS5525 16 bit MicroWire ADC to measure the output voltages, currents, and the temperature. The chips digital

outputs are used to control a multiplexer and to switch on or off the power suppliy to the HELIXes. This is controlled by the SpiCan Module.

The four output bits of the CS5525 are wired this way:

- A3 switches the power supply off when set to 1, on when 0
- A0..A2 select the measurement channel.

The four channels multiplexed to the ADC are set up like this:

- Ch 0 : +2 V output voltage, $U_{out} = U_{adc}/0.0333$
- Ch 1 : +2 V output current, $I_{out} = U_{adc}/0.0304\ ^{V}/_{A}$
- Ch 2 : −2 V output voltage
- Ch 3 : −2 V output current
- Ch 4 : Temperature measured by NTC
- Ch 5 : 100 mV reference voltage
- Ch 6 : +2 V status (red/green led digital signal, > 0 V : green)
- Ch 7 : −2 V status (red/green led digital signal, < 0 V : red)

The voltages should be adjusted such that at the connector at the flexfoils arrives VSS = -2.05 V and VDD = +2.15 V. These voltages can be measured using special adaptors which go in between the gender changers (or the connectors at the service chamber in the final experiment) and the Cables ACC-Hybrid. Increasing the Voltage is done by turning the adjustment screw clockwise for the negative voltage and counter-clockwise for the positive voltages.

A.3.2 AUX Module

The AUX modules provide the +5 V supply voltages (VCC) for the TTL components on the ACC. As this voltage can deviate from the nominal value by some percent without affecting the functionality of the TTL repeaters it is not possible to adjust it manually. It is regulated by MAX667 ICs with an accuracy of 4%. The output is floating with respect to ground. One AUX module can supply four ACCs.

A.3.3 SpiCAN Module

The crate housing the LV and AUX modules is controlled by the SpiCAN module via CAN bus. CAN is the acronym for Controller Area Network, which is a standard used in automotive industry, but also finds application in high energy physics (see for example [HB]). It was developed by Bosch in the 1980's and is now an international

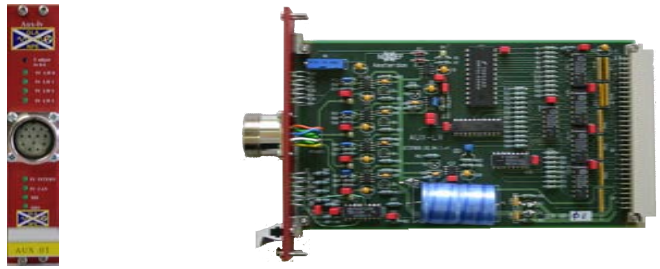

(a) Front view (b) Side view

Figure A.6: Photograph of an AUX module.

standard (ISO 11898). The CAN standard describes the physical level of communication on a two wire serial bus. The higher level standard chosen for the format of the messages is CANopen [Botooa], which is based on CAL (CAN Application Layer) developed by Philips Medical Systems.

The SpiCAN controller module is based on a Philips P80C592 8-bit micro-controller running at 16 MHz. It is programmable via a RS232 port at the front panel. The module ID and the communication speed can be set via two rotary switches at the front. Communication to the HERMES slow control chain is done via a CAN-to-USB-interface module connected to the computer `slowroc`. A more detailed description of the SpiCAN module is found in [Botoob].

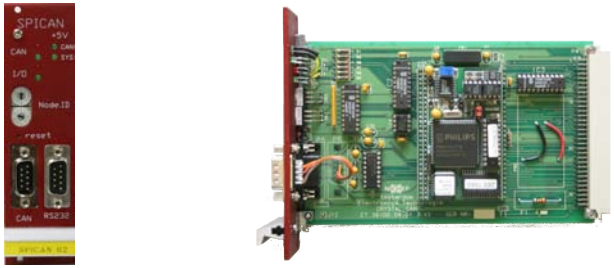

(a) Front view (b) Side view

Figure A.7: Photograph of an SpiCAN module.

B Timing of the Silicon Detector

This HowTo will provide the reader with the necessary information to set the correct timing for the recoil silicon detector, however it will not spare the reader to have read the manuals and descriptions of the modules; a working knowledge of the involved hardware is necessary. As changing the timing involves setting the parameters of at least two modules which influence each other, it is not trivial. Once the correct timing is set, it should not be changed rapidly, as gain and efficiency of the detector depend on it.

B.1 Latency

The Helix 3.0 readout chips used in the silicon modules feature a circular pipeline buffer. At each falling sample clock[1] the 128 input amplifiers of the chip deposit a charge proportional to the input charge on each strip into a capacity in a sample and hold array of 141 columns. This enables a storage depth of 141 bunches. The latency register selects which of these pipeline cells is read out after a trigger arrives (see Figure B.1 on the next page). The value should be the number of clock cycles between the actual event in question and the arrival time of the trigger at the Helix chips plus one (this additional clock cycle is due to some Helix internal delays). In the case of the Hermes recoil detector the following delays have to be taken into the calculation: 465 ns between the bunch crossing and the arrival of the trigger in rack E1, 55 ns for the cable from E1 to the recoil racks in E3 (calculated), 478 ns for the trigger processing in the NIM electronics and the HLCU (measured by F. Stinzing), 175 ns for the CAT6 cable between the ACCs and the HLCUs (measured with a test signal), 25 ns for the cables between the ACCs and the hybrid. Summing up all these

[1] The Helix is controlled via two different clocks, the sample clock and the readout clock, which can run at different frequencies. In our case both are identical as the respective input pads on the chip are shortened together.

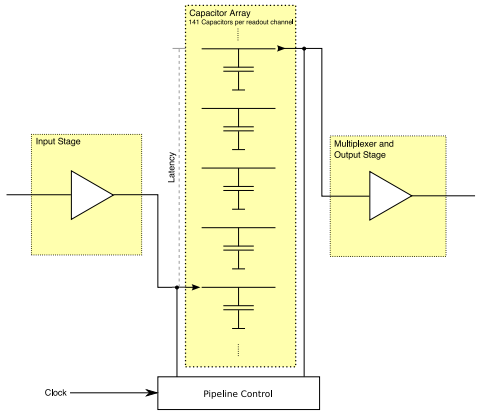

Figure B.1: A schematic view of the circular buffer of the HELIX readout chip.

delays leads to a total delay of 1198 ns or 12 clock cycles, adding the additional clock cycle for internal processing in the HELIX, a latency of 13 should be used.

The correct setting can be tested in two ways: checking filled versus empty bunches or by looking at tracks. For the first method one would use the bunch free trigger provided by the HERMES-DAQ. If the latency is set correctly, signals are suppressed in bunch free events.

The second method looks at continuous tracks. For a wrong latency the tracks in the scintillating fibre detector and the silicon detector should not line up. This needs a working analysis chain and involves a little bit more work than the first method, but it should give better results as it looks directly at physics signals. The `xtc` tracking software has been extended by S. Yaschenko to reconstruct the expected hit position in the silicon using track information from the SciFi detector. The expected hits are then filled into the `rdCluster` table and can be compared with the clusters seen by the detector. An analysis of A. Musgiller, D. Zeiler and A. Trottman showed that the correct latency setting is 13 clock cycles, as calculated.

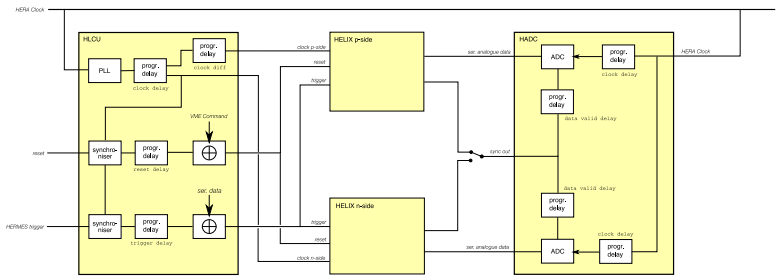

Figure B.2: An schematic overview on the various delays. For simplicity the ACC modules have not been drawn, as they only repeat the signals and are not relevant for the timing.

B.2 HLCU and HADC timing parameters

Variable delays on the HLCU steer the sampling times for the detector signals at the HELIX by shifting the clock delivered to the chips. The HADCs sampling time can be shifted with a programmable delay to coincide with the stable plateaus of the HELIX' output, which are also governed by the sampling clock delivered to the read out chips. As there is no direct connection between HADC and HLCU the timing of the HADC also has to be adjusted every time the timing of the HLCU is changed by more than a couple of ns. An overview of the various delays used can be found in figure B.2.

As a general rule one should adjust the timing starting from the HLCU. Trigger and reset delay need to be checked with an oscilloscope directly at the RJ45 output of the HLCU, the clock delay and clock difference should be adjusted in a scan while HERMES is in operation. The procedure is described later on. In the method described about 10 HERMES-runs were taken per setting to collect enough statistics. Small changes in the HLCU timing should not change anything in the signal seen at the HADC, if the timing changes are larger than 10 ns then the HADC needs to be adjusted too. Adjusting the HADC is done with pedestal runs, which can be taken during HERMES-operation, as long as the recoil detector is taken out of the readout.

B.2.1 HLCU

The HLCU needs two input signals, clock and trigger. The signals for the test pulse and the reset line are optional. All input signals are NIM level signals on standard LEMO connectors. The clock input is the HERA clock, it runs at 10.4 MHz with a duty cycle of about 50%. The trigger should be a pulse with length less than 100 ns. It needs to be timed, that only one clock cycle is present during the active phase of the trigger; when two clock-cycles are present, two events will be triggered.

The reset pulse blocks the HELIX-readout and resets the pipeline address counter to zero. It needs to be at minimum three clock cycles wide. This feature has been implemented for the use of a second level trigger, allowing to discard the data at an early stage if the event is not of interest. As the HERMES DAQ does not provide a second level trigger it is not used at the Recoil Detector and the Lambda Wheels.

The test pulse is passed to the HELIXes to generate a test signal at the input stage of each channel. Its duration needs to be longer than 2 µs. The test pulse should arrive at the HLCU some microseconds before the trigger. In the test experiment a test pulse of 5 µs length arriving 1.57 µs before the trigger gave a good signal when read out with latency 18. If the test pulse is needed, a latency scan around the calculated value (difference in clock cycles between the trigger and the test pulse arrival time) should be done to get the maximum signal.

Setting the correct timing for the output signals of the HLCU is not as complicated as it might look at a first glance. Most of the delays provided by the HLCU either never need to be touched or are robust against changes. All delays change by roughly 0.5 ns per DAC step. A more exact calibration has been done for the Lambda Wheels, showing that these values vary only by 0.03 ns between the different DACs.

The most important delay is the *clock delay* as it determines the sampling time of the HELIXes. An additional delay for the p-side clock (*clock difference*) takes care of the different charge collection times for n- and p-side[2]. This difference is a parameter defined by the detector material and does not need to be changed if the timing changes. *Clock delay* and *clock difference* can only be set per HLCU, different values for single modules or HELIXes are not possible.

To determine the optimum values for both clock delay and clock difference a timing scan has been done. If the need arises to re-do this scan, the following method provided sound results. First a scan over various settings of *clock difference* with a fixed clock delay was done to determine the timing for the p-side. For each setting

[2] The drift mobility of electrons is about a factor of three higher than the mobility of holes

around 10 HERMES-runs were taken. This data was then histogrammed for signals on the p-side of the detector versus signal on the n-side of the detector and fitted with a linear function (see Figure B.3 on the next page). The n-side HELIXes saturate earlier than the p-side HELIXes (as can be seen by the non-linear raise for n-side ADC values larger than about 450 in the shown plot), high ADC values should therefore be excluded from the fit. The slope of these fits is then plotted versus the clock difference and fitted with a second order polynomial. The maximum of this polynomial marks the highest signal gain on the p-side and therefore the best timing setting (see Figure B.4 on the following page). As the individual HELIXes on each detector side vary by up to a few nanoseconds (especially on the p-side), the average value was taken as valid for all four HELIXes of each side. A difference in the sampling time between High- and Low-gain chips has been observed and was also expected, as the raise and fall times of the input amplifiers are different due to different chip settings and input capacitances. The variations between different modules were minimal, so the same setting was chosen for all modules.

The same is then done for *clock delay*. A scan was taken over various settings of clock-delay to determine the timing for the n-side, keeping the sum of *clock delay* and *clock diff* constant to not shift the timing for the p-side. The same histograms were created, this time determining the maximum signal gain on the n-side. The timing parameters gained from these measurements in three independent analyses by A. Mussgiller, D. Zeiler and the author were a *clock difference* of 44 and a *clock delay* of 30.

The trigger sent to the HELIX chips can be delayed via the *trigger delay*. It should be set that the positive edge of the clock arrives somewhere in the middle of the trigger. As this timing is not needed to be very precise, no difference between p- and n-side is made. The reset signal sent to the HELIXes while programming (or after the corresponding VME command has been sent to the HLCU) should be adjusted via the *reset delay* that its trailing edge is close to the falling edge of the clock. Additionally the test pulse can be delayed via the *test pulse delay* to optimise the charge generation, but as the test pulse is only used to check the basic functionality of the detector and cannot be used for quantitative studies, changing it should not be needed.

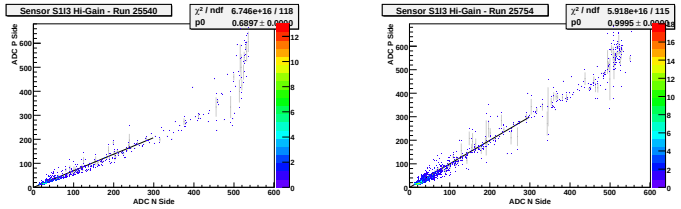

(a) *clock difference* = 20 (b) *clock difference* = 60

Figure B.3: Scatter plot of the signal on the n-side of a detector versus the signal on the p-side for two different settings of *clock difference*. A profile histogramm is superposed in gray, the black line is a linear fit $p_0 \cdot x$ on the profile.

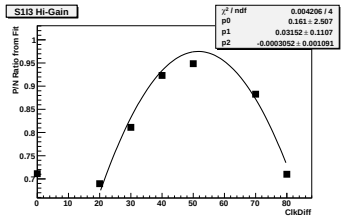

Figure B.4: The ratio of p-side signals to the n-side signals for different values of *clock difference*

B.2.2 HADC

The HADC needs three input signals, all NIM level: first the clock, usually HERA clock or another 10.4 MHz clock. Second, on the input labelled "trigger", the *Sync Out* signal[3] coming from the HELIXes is fed in; this signal triggers the digitisation of the analogue input data. And last, the Accept signal can be connected. When the HADC is read out in a single block read access, the Accept signal is necessary to start the header word preparation. If the header is not read out *en bloc* but reconstructed from the various registers, the Accept signal is not needed. The Accept signal is a short pulse, which has to arrive in a time window starting at least 6 clock cycles (or 0.55 µs) after the arrival of the leading edge of the Sync Out signal and ending before the initiation of the read out.

The fine tuning of the sampling time of the HADC is determined via two adjustable delays. The *data valid delay* allows adjusting for different arrival times of the data and the *sync out* signal from the HELIXes. It can be adjusted in multiples of a clock cycle for each detector side via a 4-bit value set in the ADC status register (ADC 0 and 1 are set together, as are ADC 2 and 3; see the description of the HADC for details). This value should be adjusted such that no trailers are visible in the data. A value of 2 is used currently at the experiment. It can be easily checked in a pedestal run without beam: if the data valid delay is set incorrectly, two distinct peaks can be seen at the lowest or the highest strips. These two peaks represent the values 1 and 0 in the trailer data.

Setting the *data valid delay* to a wrong value is used to adjust the sampling point of the HADC and to determine the trailer thresholds, as this is most easily done with the trailers visible in the data. The trailer threshold should be set to a value between the peaks for 0 and 1 visible in the trailer data. This threshold is set for one module side, so if one or two HELIXes in the read out chain have shifted trailers such as no common threshold can be found, the V_{offset} of this chip has to be tuned, although this was shown to have side effects such as the p-side HELIXes stopped working after only small changes in V_{offset}.

To determine the optimum sampling point of the HADC one uses the separation between the 0 and 1 of the trailer data. Starting at a low value for the *clock delay* one does a scan of this value. The separation of the binary 0 and 1 of the trailer should increase up to a certain *clock delay* value and then decrease suddenly. One

[3] This signal notoriously changes names: on the HELIX, it is called *Sync Out*, the corresponding input at the HADC is called Trigger and the delay *Data Valid* Delay.

Clock delay value	delay time	Clock delay value	delay time
0	15.2 ns	8	75.1 ns
1	24.8 ns	9	85.4 ns
2	35 ns	10	95.3 ns
3	45 ns	11	5.5 ns
4	55 ns	12	15.6 ns
5	65.5 ns	13	15.2 ns
6	15.2 ns	14	15.2 ns
7	15.2 ns	15	15.2 ns

Table B.1: HADC Clock delay values and their corresponding delay times as measured by C.Vogel [Vog04].

then chooses a *clock delay* value such that the separation is maximised and a small shift in the *clock delay* does not affect the separation much. The correspondence of the register values with the time delay as measured by C.Vogel [Vog04] is shown in Table B.1.

Bibliography

[A+95] K. Ackerstaff et al., *PinK: A TCL/TK based database interface to ADAMO and DAD*, (1995), Prepared for International Conference on Computing in High-Energy Physics (CHEP 95), Rio de Janeiro, Brazil, 18-22 Sep 1995.

[A+98] K. Ackerstaff et al., *The HERMES spectrometer*, Nucl. Instrum. Meth. **A417**, 230–265 (1998).

[A+02] N. Akopov et al., *The HERMES dual-radiator ring imaging Cerenkov detector*, Nucl. Instrum. Meth. **A479**, 511–530 (2002), physics/0104033.

[AGS83] B. Andersson, G. Gustafson and B. Söderberg, *A general model for jet fragmentation*, Zeitschrift für Physik C Particles and Fields **20**(4), 317–329 (1983).

[And98] B. Andersson, *The Lund Model*, Cambridge University Press, 1998.

[ATLAS] M. S. Alam et al. (ATLAS Collaboration), *ATLAS pixel detector: Technical design report*, CERN-LHCC-98-13.

[B+93] D. P. Barber et al., *The HERA polarimeter and the first observation of electron spin polarization at HERA*, Nucl. Instrum. Meth. **A329**, 79–111 (1993).

[B+02] M. Beckmann et al., *The longitudinal polarimeter at HERA*, Nucl. Instrum. Meth. **A479**, 334–348 (2002), physics/0009047.

[B+03] C. Baumgarten et al., *The storage cell of the polarized H/D internal gas target of the HERMES experiment at HERA*, Nucl. Instrum. Meth. **A496**, 277–285 (2003).

[BBC+87] R. Bock, R. Brun, O. Couet, J. Marin, R. Nierhaus, L. Pape, N. Saumon, C. Vandoni and P. Zanarini, *PAW-Towards a physics analysis workstation*, Computer Physics Communications **45**(1-3), 181–190 (1987).

[BFK+69] M. Breidenbach, J. I. Friedman, H. W. Kendall, E. D. Bloom, D. H. Coward, H. DeStaebler, J. Drees, L. W. Mo and R. E. Taylor, *Observed Behavior of Highly Inelastic Electron-Proton Scattering*, Phys. Rev. Lett. **23**(16), 935–939 (Oct 1969).

[BG] R. Brun and M. Goossens, *HBOOK-Statistical Analysis and Histogramming*, CERN Program Library Long Write-Ups Y **250**.

[Bjo69] J. D. Bjorken, *Asymptotic Sum Rules at Infinite Momentum*, Phys. Rev. **179**(5), 1547–1553 (Mar 1969).

[BKP+05] S. Balashov, B. Krauss, N. Pickert, K. Rith, F. Stinzing and C. Vogel, Energy Calibration of the Silicon Modules for the Recoil Detector with the Tandem Facility, HERMES Internal Note 05-020, May 2005.

[BM98] A. V. Belitsky and D. Mueller, *Predictions from conformal algebra for the deeply virtual Compton scattering*, Phys. Lett. **B417**, 129–140 (1998).

[BMK02] A. V. Belitsky, D. Mueller and A. Kirchner, *Theory of deeply virtual Compton scattering on the nucleon*, Nucl. Phys. **B629**, 323–392 (2002), hep-ph/0112108v1.

[Boto0a] H. Boterenbrood, CANopen, high-level protocol for CANbus, `http://www.nikhef.nl/pub/departments/ct/po/doc/CANopen20.pdf`, 2000.

[Boto0b] H. Boterenbrood, SpiCAN CANopen I/O-sytsem (for analog inputs), `http://www.nikhef.nl/pub/departments/ct/po/doc/SPICAN.pdf`, 2000.

[BR+97] R. Brun, F. Rademakers et al., *ROOT-An Object Oriented Data Analysis Framework*, Proceedings AIHENP **96**, 81–86 (1997).

[BR05] A. V. Belitsky and A. V. Radyushkin, *Unraveling hadron structure with generalized parton distributions*, Phys. Rept. **418**, 1–387 (2005).

[Bur07] M. Burkardt, *Hadron tomography*, AIP Conf. Proc. **915**, 313–318 (2007), hep-ph/0611256.

[CER02] CERN – ECP Division, CERN Software Library Documentation, `https://webafs3.cern.ch/wwwasdoc/`, 2002.

[CF99] J. C. Collins and A. Freund, *Proof of factorization for deeply virtual Compton scattering in QCD*, Phys. Rev. **D59**, 074009 (1999), hep-ph/9801262.

[CMS06] K. Klein (CMS Collaboration), *The CMS Silicon Strip Tracker - Overview and Status*, PoS **HEP2005**, 378 (2006), physics/0610259.

[Com23a] A. H. Compton, *A quantum theory of the scattering of X-rays by light elements*, The Physical Review **21**(5), 483–502 (1923).

[Com23b] A. H. Compton, *The spectrum of scattered X-rays*, The Physical Review **22**(5), 409–413 (1923).

[Ell04] F. Ellinghaus, *Beam-Charge and Beam-Spin Azimuthal Asymmetries in Deeply Virtual Compton Scattering*, PhD thesis, Humboldt-Universität zu Berlin, 2004.

[ENVY06] F. Ellinghaus, W. D. Nowak, A. V. Vinnikov and Z. Ye, *Can the total angular momentum of u-quarks in the nucleon be accessed at HERMES?*, Eur. Phys. J. **C46**, 729–739 (2006), hep-ph/0506264.

[ESS37] I. Estermann, O. C. Simpson and O. Stern, *The Magnetic Moment of the Proton*, Phys. Rev. **52**(6), 535–545 (Sep 1937).

[FB98] W. Fallot-Burghardt, *A CMOS Mixed-Signal Readout Chip for the Microstrip Detectors of HERA-B*, PhD thesis, Ruprecht-Karls-Universität Heidelberg, 1998.

[Fey69] R. P. Feynman, *Very High-Energy Collisions of Hadrons*, Phys. Rev. Lett. **23**(24), 1415–1417 (Dec 1969).

[FR00] M. Feuerstack-Raible, *Overview of microstrip read-out chips*, Nucl. Instrum. Meth. **A447**, 35–43 (2000).

[GEANT403] S. Agostinelli et al. (GEANT4 Collaboration), *GEANT4: A simulation toolkit*, Nucl. Instrum. Meth. **A506**, 250–303 (2003).

[GHK+04a] I. M. Gregor, I. Hristova, M. Kopytin, W. Lange, M. Reinecke, C. Shearer, J. Stewart and A. Vandenbroucke, Study of the First Prototype for the HERMES Silicon Recoil Detector with the ZEUS Beam Telescope, HERMES Internal Note 04-019, June 2004.

[GHK+04b] I. M. Gregor, I. Hristova, M. Kopytin, W. Lange, M. Reinecke, J. Stewart and A. Vandenbroucke, A Laser test-stand for the new Hermes Recoil Silicon Detector, HERMES Internal Note 04-016, July 2004.

[GHR+05] I. M. Gregor, I. Hristova, M. Reinecke, A. Vandenbroucke and S. Balashov, Choice Test of HELIX Parameters for the new HERMES Recoil Silicon Detector, Available on the Recoil Detector Webpage, July 2005.

[GM64] M. Gell-Mann, *A Schematic Model of Baryons and Mesons*, Phys. Letters **8**(3), 214 (1964).

[GPV01] K. Goeke, M. V. Polyakov and M. Vanderhaeghen, *Hard exclusive reactions and the structure of hadrons*, Prog. Part. Nucl. Phys. **47**, 401–515 (2001), hep-ph/0106012.

[Group02] K. Hagiwara et al. (Particle Data Group Collaboration), *Review of particle physics*, Phys. Rev. **D66**, 010001 (2002).

[HB] B. Hallgren and H. J. Burckhart, *Frontend I/O via CANbus of the ATLAS detector control system*, Given at 4th Workshop on Electronics for LHC Experiments (LEB 98), Rome, Italy, 21-25 Sep 1998.

[HC98] Hermes-Collaboration, Technical Design Report of the new Silicon-Detector System, Technical report, 1998, HERMES internal note 98-014.

[HC01] Hermes-Collaboration, The HERMES Recoil Detector, Technical report, 2001, HERMES Internal Note 02-003.

[HERMES01] A. Airapetian et al. (HERMES Collaboration), *Measurement of the beam spin azimuthal asymmetry associated with deeply-virtual Compton scattering*, Phys. Rev. Lett. **87**, 182001 (2001), hep-ex/0106068.

[HERMES05] H. E. Jackson (HERMES Collaboration), *The HERMES dual radiator RICH: Performance and impact*, Nucl. Instrum. Meth. **A553**, 205–209 (2005).

[HERMES07] A. Airapetian et al. (HERMES Collaboration), *The beam-charge azimuthal asymmetry and deeply virtual Compton scattering*, Phys. Rev. **D75**, 011103 (2007), hep-ex/0605108.

[Hil05] A. Hillenbrand, *Measurement and Simulation of the Fragmentation Process at HERMES*, PhD thesis, Universität Erlangen-Nürnberg, 2005.

[HMG+05] I. Hristova, M. Murray, I. M. Gregor, W.-D. Nowak, M. Reinecke, J. Stewart and A. Vandenbroucke, HERMES Recoil Silicon Detector Calibration to MIPs at T22 at DESY, HERMES Internal Note 05-014, April 2005.

[Hoe06] M. Hoek, *Design and Construction of a Scitillating Fibre Tracker for measuring Hard Exclusive Reactions at HERMES*, PhD thesis, Justus-Liebig-Universität Gießen, 2006.

[Ji97a] X.-D. Ji, *Deeply-virtual Compton scattering*, Phys. Rev. **D55**, 7114–7125 (1997).

[Ji97b] X.-D. Ji, *Gauge invariant decomposition of nucleon spin*, Phys. Rev. Lett. **78**, 610–613 (1997).

[JMS97] X.-D. Ji, W. Melnitchouk and X. Song, *A study of off-forward parton distributions*, Phys. Rev. **D56**, 5511–5523 (1997).

[JO98] X.-D. Ji and J. Osborne, *One-loop corrections and all order factorization in deeply virtual Compton scattering*, Phys. Rev. **D58**, 094018 (1998), hep-ph/9801260.

[Joh28] J. Johnson, *Thermal Agitation of Electricity in Conductors*, Physical Review **32**(1), 97–109 (1928).

[KBF+99] A. Kastenmuller, M. Bohmer, J. Friese, R. Gernhauser, J. Homolka, P. Kienle, H. J. Korner, D. Maier, M. Munch, C. Theurer and K. Zeitelhack, *Fast detector readout for the HADES-RICH*, Nucl. Instrum. Meth. A **433**, 438–443 (1999).

[Kem80] J. Kemmer, *Fabrication of Low Noise Silicon Radiation Detectors by the Planar Process*, Nucl. Instrum. Meth. **169**(3), 499–502 (1980).

[KLS+02] M. Kopytin, W. Lange, C. Shearer, J. Stewart and A. Vandenbroucke, Decision on the readout chip for the new Hermes silicon recoil detector, HERMES Internal Note 02-020, June 2002.

[KMP05] T. Keri, A. Mussgiller and N. Pickert, `daq4servicing` Documentation, `http://www-hermes.desy.de/groups/rcoilgrp/recoil/techdoc/software/daq4servicing/html/index.html`, 2005.

[KNo2] V. A. Korotkov and W. D. Nowak, *Future measurements of deeply virtual Compton scattering at HERMES*, Eur. Phys. J. **C23**, 455–461 (2002), hep-ph/0108077.

[Kop06] M. Kopytin, *Longitudinal Target-Spin Azimuthal Asymmetry in Deeply-Virtual Compton Scattering*, PhD thesis, Humboldt-Universität zu Berlin, 2006.

[Kra00] B. Krauss, Ein Silizium-Detektor für das HERMES-Experiment, Master's thesis, Universität Erlangen-Nürnberg, 2000.

[Kra05] B. Krauss, *Deeply Virtual Compton Scattering and the HERMES-Recoil Detector*, PhD thesis, Universität Erlangen-Nürnberg, 2005.

[KS05] S. Köstner and U. Straumann, *Noise considerations of the Beetle amplifier used with long silicon strip detectors*, (2005), CERN-LHCB-2005-029.

[LA88] E. Leader and M. Anselmino, *A crisis in the parton model: Where, oh where is the proton's spin?*, Z. Phys. **C41**, 239 (1988).

[Lut91] G. Lutz, *Correlated Noise in Silicon Strip Detector Readout*, Nucl. Instrum. Meth. **A309**, 545–551 (1991).

[Lut99] G. Lutz, *Semiconductor Radiation Detectors: Device Physics*, Springer, Berlin, Germany, 1999.

[McK51] K. McKay, *Electron-Hole Production in Germanium by Alpha-Particles*, Physical Review **84**(4), 829–832 (1951).

[MH56] R. W. McAllister and R. Hofstadter, *Elastic Scattering of 188-Mev Electrons from the Proton and the Alpha Particle*, Phys. Rev. **102**(3), 851–856 (May 1956).

[O+03] T. O'Neill et al., *Development of the TIGRE Compton Telescope for Intermediate-Energy Gamma-Ray Astronomy*, IEEE Trans. Nucl. Sci. **50,2**, 251 (2003).

[Pei92] A. Peisert, *Silicon microstrip detectors*, Adv. Ser. Direct. High Energy Phys. **9**, 1–79 (1992).

[Pfe04] K.-F. Pfeiffer, *Evaluation of the Medipix Detectors for Medical X-Ray Imaging, with Special Consideration of Mammography*, PhD thesis, Universität Erlangen-Nürnberg, 2004.

[R+04] M. Reinecke et al., *A silicon strip recoil detector for momentum measurement and tracking at HERMES*, IEEE Trans. Nucl. Sci. **51**, 1111–1116 (2004).

[Rad96] A. V. Radyushkin, *Scaling Limit of Deeply Virtual Compton Scattering*, Phys. Lett. **B380**, 417–425 (1996), hep-ph/9604317.

[Rad97] A. V. Radyushkin, *Nonforward parton distributions*, Phys. Rev. **D56**, 5524–5557 (1997).

[Rad98] A. V. Radyushkin, *Compton scattering and nonforward parton distributions*, (1998), hep-ph/9811223.

[Sch18] W. Schottky, *Über spontane Stromschwankungen in verschiedenen Elektrizitätsleitern*, Annalen der Physik **57**(23), 541–567 (1918).

[Sch85] P. Schmueser, *The electron-proton colliding beam facility HERA*, Nucl. Instrum. Meth. **A235**, 201–208 (1985).

[She04] C. Shearer, Integration of the Recoil Detector into the HERMES Monte Carlo Simulation, HERMES Internal Note 04-007, February 2004.

[ST64] A. A. Sokolov and I. M. Ternov, *On Polarization and spin effects in the theory of synchrotron radiation*, Phys. Dokl. **8**, 1203–1205 (1964).

[Sta06] M. Stattera, *Superconducting Magnetic Systems for High Energy Polarized Physics*, PhD thesis, Università degli Studi di Ferrarara, 2006.

[Ste98a] J. J. M. Steiger, Noise behaviour of the APC, Internal silicon detector report, September 1998.

[Ste98b] J. J. M. Steijger, Noise from Erlangen, Internal silicon detector report, Juni 1998.

[Tai06] P. Tait, *Beam-Induced Depolarisation at the HERMES Transversely Polarised Hydrogen Target*, PhD thesis, Universität Erlangen-Nürnberg, 2006.

[The] The HERMES Lambda Wheel-Group, Lambda Wheel Documentation and Manual, `http://www.nikhef.nl/pub/experiments/Hermes/Instrumentation/LambdaWheels/Descriptions_Manuals/begin.html`.

[Tru00] U. Trunk, *Development and Characterisation of the Radiation tolerant HELIX128-2 Readout Chip for the HERA-B Microstrip Detectors*, PhD thesis, Ruprecht-Karls-Universität Heidelberg, 2000.

[V+04] J. Visser et al., *Design and performance of a silicon test counter for HERMES*, Nucl. Instrum. Meth. **A521**, 430–440 (2004).

[VGG99] M. Vanderhaeghen, P. A. M. Guichon and M. Guidal, *Deeply virtual electroproduction of photons and mesons on the nucleon: Leading order amplitudes and power corrections*, Phys. Rev. **D60**, 094017 (1999), hep-ph/9905372.

[vH07] Y. van Haarlem, *The HERMES recoil photon-detector and nuclear p_t broadening at HERMES*, PhD thesis, Universiteit Gent, 2007.

[VL05] I. Vilardi and L. Lagamba, Progress in Cosmics Analysis, Talk given at the Recoil Meeting, July 2005.

[Vog04] C. Vogel, HADC VME map, silicon group internal communication, 2004.

[Vog08] C. Vogel, *Kalibration von Siliziumdetektoren für den HERMES Rückstoßdetektor*, PhD thesis, Universität Erlangen-Nürnberg, to be published in 2008.

[W+95] W. Wander et al., *DAD - Distributed ADAMO Database system at HERMES*, (1995), Prepared for International Conference on Computing in High-Energy Physics (CHEP 95), Rio de Janeiro, Brazil, 18-22 Sep 1995.

[Wan96] W. Wander, *Rekonstruktion hochenergetischer Streuereignisse im HERMES-Experiment*, PhD thesis, Universität Erlangen-Nürnberg, 1996.

[YDG+05] Z. Ye, M. Dohlus, I. M. Gregor, Y. Holler, I. Hristova, J. Lund-Nielsen, V. Prahl, M. Reinecke, J. Stewart, A. Vandenbroucke and M. Wendt, Radio Frequency Test for the HERMES Silicon Recoil Detector, HERMES Internal Note 05-008, March 2005.

[Ye06] Z. Ye, *Transverse Target-Spin Asymmetry Associated with Deeply Virtual Compton Scattering on the Proton and A Resulting Model-Dependent Constraint on the Total Angular Momentum of Quarks in the Nucleon*, PhD thesis, Universität Hamburg, 2006.

[Zwe64] G. Zweig, An SU(3) Model for Strong Interaction Symmetry and its breaking, CERN preprint 8419/TH.412 (unpublished), re-printed in *Lichtenberg, D. B. (Ed.), Rosen, S. P. (Ed.): Developments In The Quark Theory Of Hadrons, Vol. 1*, 22- 101, 1964.

List of Acronyms

ADC Analog Digital Converter

ASIC Application Specific Integrated Circuit

BCA Beam Charge Asymmetry

BH Bethe-Heitler process

BSA Beam Spin Asymmetry

DIS Deep-Inelastic Scattering

DSP Digital Signal Processor

DVC Drift Vertex Chamber

DVCS Deeply Virtual Compton Scattering

FC Front drift Chamber

FIFO First-In First-Out

FF Form Factor

GPD Generalised Parton Distribution

HDC Hermes decoder

HMC Hermes Monte Carlo

HRC Hermes reconstruction program

LW Lambda-Wheel

LTSA Longitudinal Target Spin Asymmetry

MC Magnet Chamber

μDST micro Data Summary Tape

MIP Minimum Ionising Particle

PDF Parton Distribution Function

PID Particle Identification

QED Quantum Electro-Dynamics

QCD Quantum Chromo-Dynamics

RD Recoil Detector

RICH Ring Imaging Čerenkov Counter

TRD Transition Radiation Detector

TTSA Transverse Target Spin Asymmetry

Acknowledgements

The times when a physicist sat alone in his laboratory, working on strange apparati, making interesting discoveries singlehanded are long gone by, if they ever existed. As any other, this work would not have been possible without a great many people, of which I am sure I forgot to mention some. So at first an apology, it did not happen on purpose.

In particular, I would like to thank Prof. Dr. K. Rith for giving me the opportunity to accompany the Silicon Recoil Detector from the first test (during my Diploma thesis) and the commissioning till the dismounting end of June 2007. Seeing the whole lifetime of a detector is a rare thing, as planning and commissioning of recent detectors are usually in the order of tens of years. I am also grateful for the support (both, physics related and morally) and the good working atmosphere I enjoyed in our group in Erlangen and especially the lunch break discussions with Prof. Dr. E. Steffens. I am most obliged to Chris Vogel, who helped my a lot in programming and who more than often wrote helpful and usable software in about five minutes where I would have taken weeks, and to Dietmar Zeiler, who helped me understanding the physics of DVCS and the detector itself.

During my time in Hamburg I also got a lot of help and support from all HERMES colleagues, to many to mention them all. I have learned a lot on detectors and how to operate them from my colleagues in the Recoil group.

I am especially thankful to Andreas Mussgiller and Sergey Yashenko, who helped me a lot in understanding the silicon detector and who also did an amazing work in creating most of the tracking and analysis software used for the Recoil Detector. The time in Hamburg would have been much less enjoyable without Morgan, Henning, Ana and Susanne, who provided me with morale support and a social live.

Also I want to thank Volker Prahl and Matthias Reinecke, whose knowledge on mechanics and electronics more then often helped to make an idea reality, no matter how unrealisable it sounded. Without them, the detector would never have worked. And besides that, both are very fun to work with. The workshops both at DESY and in Erlangen need to be mentioned as well, thanks to their fast and reliable work and their ability to translate from a confuse physicists idea to a real life thing the detector could be constructed as it was planned.

And last but not least I have to thank my family and my friends to support and help me for all that time, besides my family especially Mariana, Nuno and Pedro as well as Micha and Markus.